7-1-2015

# Improvements to Optical Diagnostics of Thermal Barrier Coatings: Contaminant Identification during Laser Cleaning and Time Gated Photoluminescence Piezospectroscopy

Hyung Nun Kim
*Mechanical Engineering*, hyung.kim@uconn.edu

# Improvements to Optical Diagnostics of Thermal Barrier Coatings: Contaminant Identification during Laser Cleaning and Time Gated Photoluminescence Piezospectroscopy

Hyung Nun Kim B.S.

B.S., University of Connecticut 2013

A Thesis

Submitted in Partial Fulfillment of the

Requirements for the Degree of

Master of Science

at the

University of Connecticut

2015

APPROVAL PAGE

Master of Science Thesis

Improvements to Optical Diagnostics of Thermal Barrier Coatings: Contaminant Identification during Laser Cleaning and Time Gated Photoluminescence Piezospectroscopy

Presented by:

Hyung Nun Kim B.S.

Major Advisor:_____

Michael W. Renfro

Associate Advisor:_____

Eric H. Jordan

Associate Advisor:_____

Baki M. Cetegen

University of Connecticut

2015

Acknowledgements

I would like to thank Professor Renfro for taking me in as his student for his exciting research. His guidance throughout the years has truly brought the contents of this Thesis to a realization. I would like to thank Professor Jordan for always providing his expertise on TBCs. I would like to thank Professor Cetegen for being a part of the advisory committee. I would like to thank Martin for his help in understanding LIBS and PLPS as well as LabVIEW programming, and Nirav for his help in using IMS equipment.

I am grateful to University of Connecticut and the Mechanical Engineering department.

I would like to thank my father, mother, and brother for their support.

This work was supported by Rolls-Royce Corporation.

**Table of Contents**

**Table of Figures**

**Abstract**

Laser ablation has previously been demonstrated as a technique for removal of contaminants from engine-run thermal barrier coatings (TBC). A method for monitoring the concentrations of some of the known constituents of the contaminants is developed for paralleled quantification during laser cleaning. The major constituents of these contaminants, CaO, MgO, $Al_2O_3$, and $SiO_2$, also termed CMAS, are prepared in pressed powder samples for which Laser-induced Breakdown Spectroscopy (LIBS) is applied. During LIBS, unique spectra characterizing the contents of the ablated material are obtained. LIBS is applied to the individual CMAS constituent pressed powder samples to obtain reference spectra which are used to construct a set of orthonormal modes via Proper Orthogonal Decomposition (POD). Although these orthogonal modes are mathematically uncorrelated, they may not necessarily be entirely representative of the correspondent constituent references that may cause inaccurate quantifications. Thus, these modes are renormalized by taking advantage of orthogonality between the modes and using that property as a constraint; by doing so, the modes can be reshaped while retaining orthogonality. The resulting orthogonal modes were calibrated using known mixtures, and then applied to engine-run blades for measurements. The missing constituents were quantified by a calculation of residual data.

Photoluminescence Piezospectrocopy (PLPS), a nondestructive evaluation (NDE) technique that has been previously used to assess remaining lifetime of TBCs, can suffer from fluorescence interference due to dopants in the coating composition. Unlike that of CMAS obstruction, which can be cleaned via LIBS, the source of interference within the coating could not be physically removed. A different approach was taken to enable evaluation of TBC health; the collected fluorescence was time gated (or time resolved) prior to being spectrally resolved for meaningful measurements. Results showed that variations in the stress across the blade could be resolved.

## 1. Introduction

Aerial transportation has been globally adopted for long distance travels in both domestic and international flights. For such a ubiquitous application, particular challenges reside in enhancement of the engine performance as well as verification of the healthy status of each and every engine component to assure intended functionality. Operation of modern gas-turbine engines employed in aviation is derived from the Brayton Cycle—a thermodynamic cycle defined by isobaric combustion. During the Brayton Cycle, atmospheric air intake at the compressor is pressurized, mixed with fuel then burned at the elevated pressure. The resulting high-temperature high-pressure gas passes through turbine where the pressure is then decreased, yielding a net work output for aircraft propulsion. The thermal efficiency of the Brayton Cycle model is mathematically governed by the maximum temperature at the turbine inlet, and the maximum permissible temperature is physically constrained by the metallurgic properties of the turbine components exposed to the adverse surroundings (Moran, 2010). The ideal Brayton Cycle model is shown in Fig. 1.

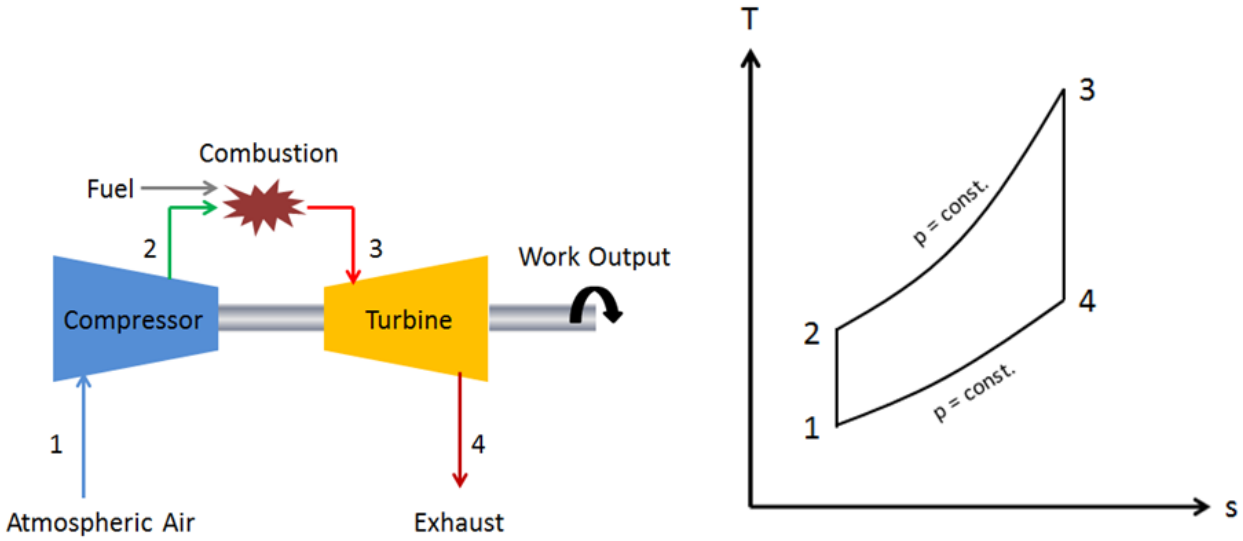


$$\eta = 1 - \frac{T_1}{T_2} = 1 - \frac{T_3}{T_4}$$

Figure 1: Ideal Brayton Cycle model (left), and corresponding T-s diagram and thermal efficiency (right).

To weather the difficult environment present in the hot gas path, contemporary turbine blades are equipped with cooling mechanisms that consist of internal and external heat management, as shown in Fig. 2.

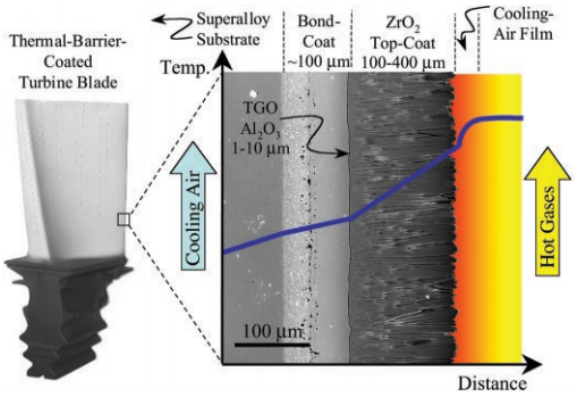


Figure 2: Cross-sectional Scanning Electron Micrograph (SEM) of an Electron-Beam Physical Vapor Deposition (EB-PVD) Thermal Barrier Coating (TBC). The illustrated temperature profile demonstrates the effectiveness of the internal and external cooling mechanisms for a turbine blade, Padture *et al.*

To enhance heat transfer internally, a network of cooling channels are installed within the blade. These channels are often complemented with myriad of heat fins to induce turbulent flow near the passage walls for reinforced convective heat transfer. The effects of internal cooling channels were observed for stationery as well as rotary conditions of the blade in a simulation study (Han, 2004). For external heat regulation, the outer surface of the blade is furnished with an insulative safeguard known as Thermal Barrier Coating (TBC). TBCs are ceramic top-coats with low thermal conductivity that offer considerable reduction in temperature over the span of the coating thickness. The breakthrough in advanced cooling technology has revolutionized the design of turbine blades; the implementation of an internal and external cooling scheme allows operational temperatures of the hot gas path to exceed 100° to 300°C above the melting point of the underlying metal substrate, thereby upgrading engine performance (Padture, 2002).

To realize the structural integration of two fundamentally distinctive materials, a bond coat is applied to secure the TBC onto the metal substrate. The composition of the bond coat is concocted to accommodate various necessities of the blade; the bond coat must ensure firm adhesion of the TBC, and also feature sufficient oxidation resistance. The latter requirement is critical in turbine applications especially during prolonged thermal loading; although TBCs disallow the substrate to liquefy, the

temperatures are high enough at this interface to provoke inevitable oxidation in the bond coat. This sequence of events induces lateral growth of an additional layer commonly termed thermally grown oxide (TGO) (Padture, 2002). Excessive thickening of the TGO leads to unbearable stresses in this interface that eventually causes the TBC to disengage from the blade structure, rendering the substrate vulnerable to intolerable temperatures that were previously enabled by the TBC. For these reasons, the finite serviceable time of turbine blades is equated to the lifespan of TBC (Tolpygo, 2001).

The duration of thermal stress (e.g duration of flight), frequency of thermal loading and unloading (e.g take-off and landing), as well as imperfections in blade manufacture (e.g. rugged interfaces) contribute to some of the variabilities of the coating lifespan. Common industrial practice involves commitment to an allowance of a pre-specified number of thermal cycles before the blades are renewed, thereby discounting the possibilities of premature or overdue disposal. Photoluminescence Piezospectroscopy (PLPS) is a technique that has been under development to assess the remaining coating lifetime in efforts to quantify turbine maintenance schedules—to maximize coating service time without risk. Through PLPS, one is able to examine stress levels in the TGO without incurring damage to the structure, thereby classifying it as a non-destructive evaluation (NDE) technique. The diverse applicability of PLPS (e.g. TGO examination, remaining coating lifetime assessment, coating lifetime prediction) has been demonstrated in a previous study (Gell, 2004).

The use of the described coating technology in engines that ingest atmospheric air under a wide range of conditions causes accumulation of foreign contaminants carried by the air on the top surface of TBCs during operation. Although the composition of atmospheric air intake is not exclusive to these compounds, CaO, MgO, $Al_2O_3$, and $SiO_2$ have been identified to be the major contributors to the contamination, therefore referred to as CMAS. CMAS, with a melting point of approximately 1240 °C as well as exceptional wetting properties, tend to envelop the TBC during operation as shown in Fig. 3 (referred to as a CMAS attack).

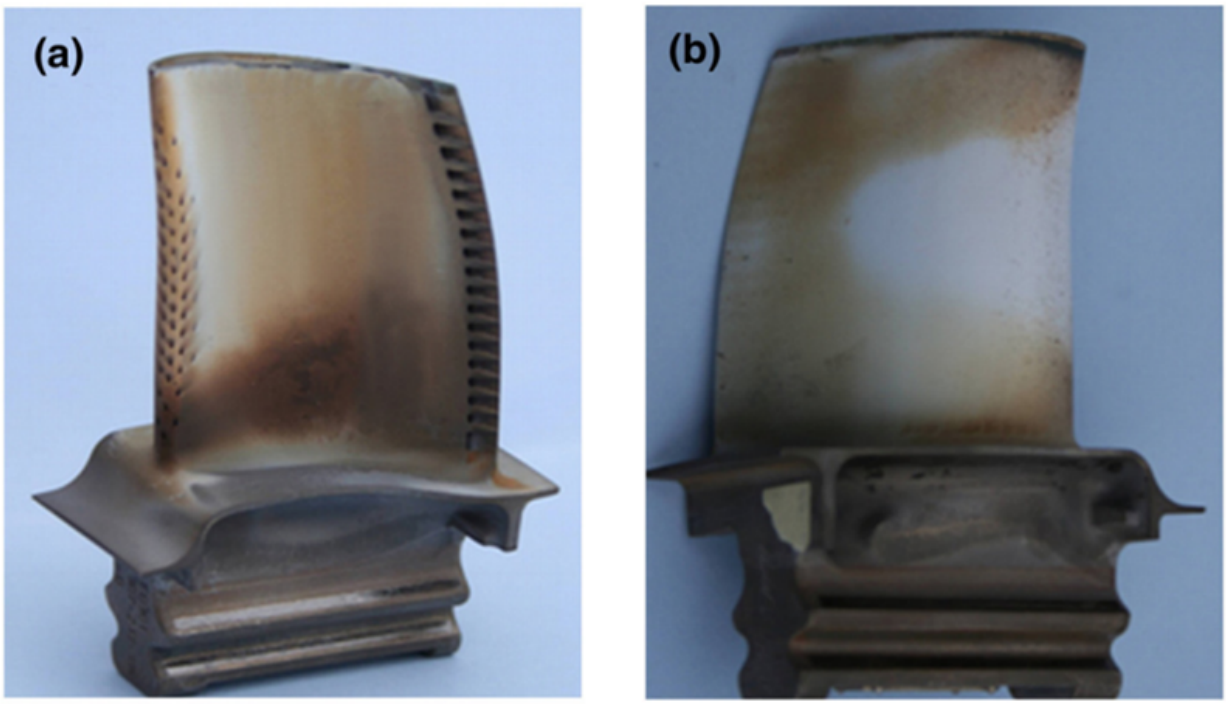

Figure 3: Engine-run blade: Severe case of CMAS contamination seen on a) pressure side and b) suction side, Vidal-Setif *et al.*

Especially in coatings produced by electron beam physical vapor deposition (EB-PVD) defined by its porous structure, the molten CMAS can invade deeper beyond the surface as much as the temperature gradient allows (> 1240 °C); upon cooling, the solidified CMAS may induce degradation of mechanical toughness of TBCs (Wellman, 2007). Although this mode of failure may be secondary to the oxidation-induced failure of TBCs, a major disadvantage of CMAS attack is that it invalidates PLPS analysis on such samples (Hansen, 2007). In consideration to sampling a CMAS contaminated blade for PLPS, which observes the fluorescence peak shifts in chromium ions in the alumina that comprises TGO, the source of photoexcitation is intercepted by the alumina in CMAS that ensues erroneous measurements. To address the presence of CMAS, Laser Induced Breakdown Spectroscopy (LIBS) was applied as a method to effectively remove the contaminants without damaging the TBC; such preparation of samples permitted routine PLPS afterward (Majewski, 2011). However, in this previous work the LIBS signal was only used to determine a criterion for removing the contamination, but it was not used to examine the composition of the contaminants.

In the presented thesis, a scheme for CMAS speciation to exercise composition monitoring during contaminant cleaning is developed. Because of the variability in CMAS constituent deposits that may occur due to differences in weather, climate, and/or unique manifestations (e.g. volcanos) of the globe, reliable inspection of individual composition may enable further investigation and motivation in CMAS-related research. Such applications may include, but are not limited to, correlative study on CMAS compositions to notable changes in its properties (e.g. melting temperature), unanticipated interactions with TBC (e.g. further considerations in coating life prediction), as well as probabilistic analysis regarding the locations of operation solely based on CMAS information. Additionally, an experimental scheme for filtering fluorescence interference inherently caused by certain coating modifications (as opposed to foreign interference such as CMAS that can be removed via LIBS) is developed. With the possibility of incessant alterations to coating compositions for improved performance, adaptations to the conventional PLPS are devised accordingly; in a scenario where the chromium fluorescence is disturbed by a particular composite dosed TBC near the frequency of interest, a time-gate is enforced to extract only the meaningful information. In the subsequent chapters, the formulation of CMAS speciation and time-gated PLPS, as well as results, are illustrated in detail.

## 2. Background

### 2.1 Thermal Barrier Coating System

Thermal Barrier Coating (TBC), Thermally Grown Oxide (TGO), bond coat, and the metal substrate are distinctive layers that comprise the overall blade airfoil structure, also referred to as the Thermal Barrier Coating system. Although it has been established that CaO-MgO-$Al_2O_3$-$SiO_2$ (CMAS) deposition and TGO growth occur post-operation, previous studies have concluded that it was preferable to apply a thin layer of TGO in form of α-alumina by means of surface treatment to enhance TBC durability (Gell, 2004). Therefore, a distinction is made for defining what comprises the TBC system; TBC, TGO, bond coat, and the metal substrate are carefully engineered to optimize each of its own primary functionality, as well as extensions to secondary purposes. CMAS, on the other hand, is strictly a foreign byproduct of engine activity and is rather characterized by uncertainty and randomness in its composition and behavior. Nevertheless, the individual layers of the TBC system, as shown in Fig. 4, are reviewed and discussed in further detail.

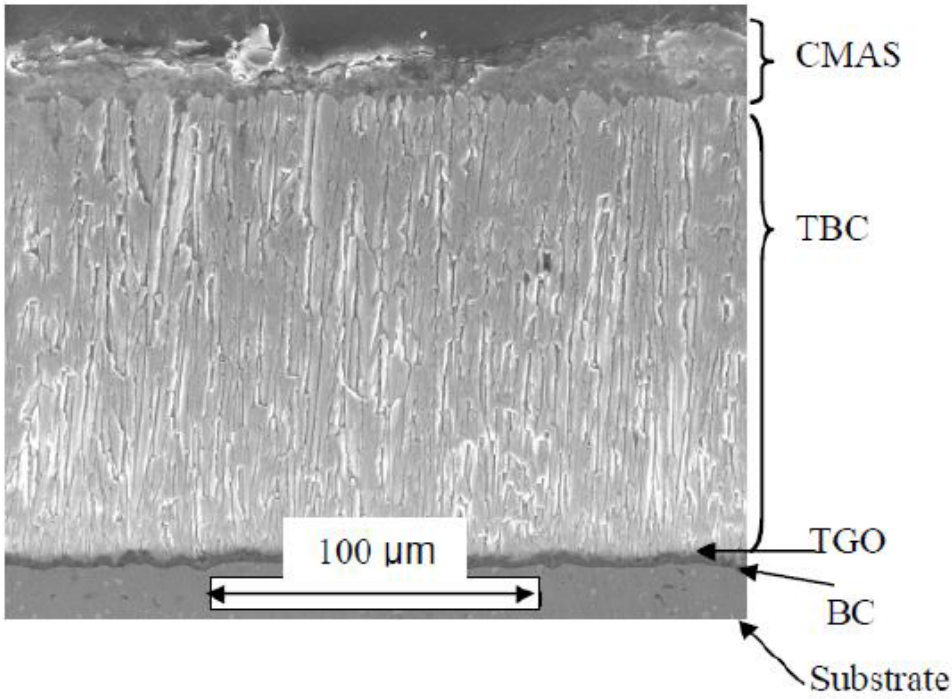


Figure 4: Cross-sectional Scanning Electron Micrograph (SEM) of an engine-run EB-PVD TBC system. CMAS levels are uneven and sporadic, TBC has a fine columnar structure, subtle ridges seen within TGO, and mild cracking in the Bond Coat, Majewski *et al.*

### 2.1.1 Thermal Barrier Coatings (TBC)

TBCs are top-coats engineered primarily towards thermal insulation. A standard TBC composition is comprised of 6-8 wt% $Y_2O_3$–stabilized $ZrO_2$ (YSZ); although alternative ceramic compositions have been investigated to exhibit lower thermal conductivities, other factors of consideration included resistance to erosion as well as delamination (Wellman, 2007). It has also been observed that coatings with inferior durability can be susceptible to sintering effects causing a decline in thermal resistance as a result of thermal aging (Cernuschi, 2004). Therefore, overall coating toughness and stability has become additional criteria for the coating ceramic composition. YSZ has been confirmed to surpass the alternatives in terms of coating durability, thus restricting the probability of failure mechanisms to interface delamination and non-brittle type fracture in extreme cases (Zhu, 2003, Loganathan, 2012). By narrowing the possible types of failure in such manner, damage detection, damage identification, and health monitoring procedures become increasingly reliable.

Modern TBC systems are often classified under two categories based on the method of applying the coating: air plasma spray (APS), and electron beam physical vapor deposition (EB-PVD). APS and EB-PVD refers to the method of the coating installation, and are primarily characterized by its microstructure, as schematically drawn in Fig. 5. APS TBC comprise of random imperfections in forms of horizontal splat boundaries; because of the perpendicular orientation of the splats relative to the direction of the heat flux, APS TBC surpasses EB-PVD TBC in thermal resistance. However, the described imperfections contribute to structural instability (e.g. micro-scale fracture becomes increasingly probable) (Schlichting, 2003); APS TBCs are vulnerable to numerous cracking mechanisms located in both the TGO interface as well as within the TBC, and thus generally have shorter lifespans relative to EB-PVD TBC (Schlichting, 2003). On the other hand, EB-PVD TBCs are characterized by its fine columnar porous structure, and is the preferred choice for advanced gas turbine engines. Because the columnar features are in parallel to the heat flux, EB-PVD TBC has a higher thermal conductivity than APS TBC, but this microstructure is favorable for increased coating durability. As opposed to APS TBCs, EB-PVD TBCs have been observed to exhibit cracking mechanisms predominantly in the TGO interface

only, and this can be attributed to the absence of the horizontal splat boundaries found in APS TBCs (Padture, 2002).

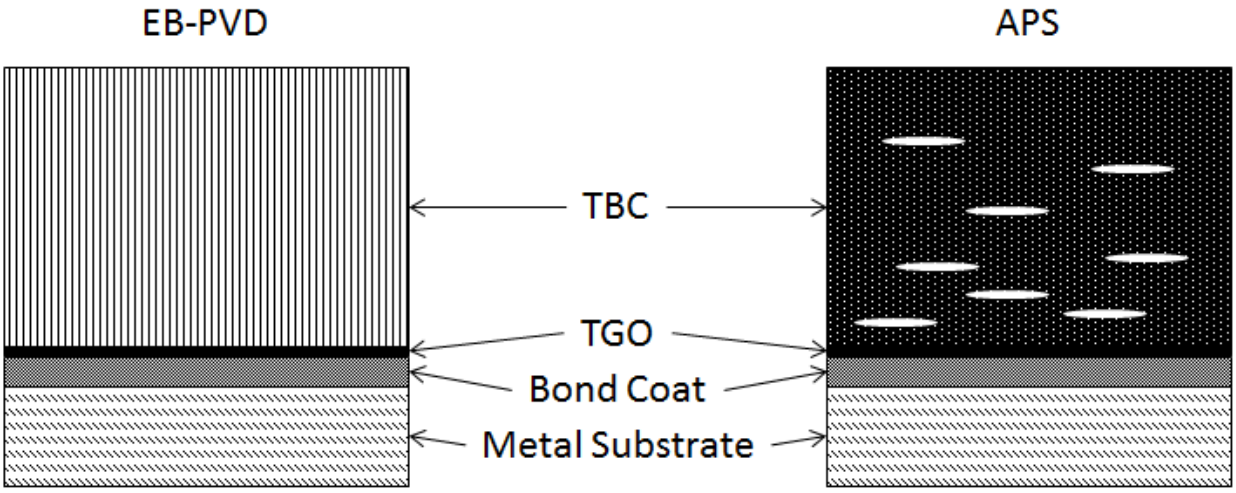


Figure 5: Schematic difference between EB-PVD and APS TBC systems.

EB-PVD TBCs have significantly higher manufacturing costs than APS TBCs, thus, is mainly implemented on the turbine blades, whereas APS TBCs may be found in less intensive applications such as combustor hardware where operating environment is not as extreme (Feuerstein, 2007). In essence, the central trade-offs between APS and EB-PVD are outlined by the specifications in thermal conductivity, durability, and cost.

### 2.1.2 Bond Coat, TGO, and oxidation-induced TBC failure

The bond coat, much like TBC, can be applied via APS or EB-PVD, and also Low-Pressure Plasma Spray (LPPS). Typically comprised of platinum-modified nickel aluminide, or (Ni, Pt)Al, the bond coat composition emphasizes adhesive and oxidation-resistive capabilities. Furthermore, the bond coat is devised to dictate TGO development exclusively in $\alpha$-$Al_2$-$O_3$ for slow and uniform growth (Padture, 2002).

With the temperature of the hot gas path that may exceed 1300 °C, inevitable oxidation occurs with the bond coat resulting in formation of TGO. Typically in EB-PVD TBCs, damage initiation as well as coating failure occurs at this interface. The physics of coating failure can be attributed to thermal

mismatches among TBC, TGO, and bond coat. In a previous study, TGO growth was observed for grit-blasted and as-aluminized (Ni, Pt)Al bond coat with the presence and absence of a TBC overlay; the goal of experiments was to determine if definitive early signs of failure in terms of TGO thickness could be identified prior to actual failure (Tolpygo, 2001). Results showed that TGO consistently reached a certain maximum thickness in which additional growth could not be detected; furthermore, there were minimal indicative evidence regarding TGO thickness immediately prior to TBC failure. By estimating the changes in TGO thickness and mass change over oxidation time, correlative analysis confirmed the strain energies stored within the TGO (Tolpygo, 2001). The development of such strain energy can be attributed to thermal mismatches among TBC, TGO, and bond coat, complemented by continual thermal loading and unloading.

In a more recent study, the morphological changes in the TGO were observed over the lifespan of TBCs (Wen, 2006). Results showed that subtle ridges at the metal/oxide interface (imperfections in the bond coat) became much more pronounced with repetitive thermal cycling. Such roughening of this interface, commonly referred to as rumpling, develops local reversals of compressive and tensile stresses that causes strain at which eventual separation and cracking occurs. Accumulation of the described local damage leads to large-scale separation of TBC, often defined as spallation failure. The development of the rumpling profile (Fig. 6) with respect to number of thermal cycles has been documented to demonstrate this mode of failure (Wen, 2006).

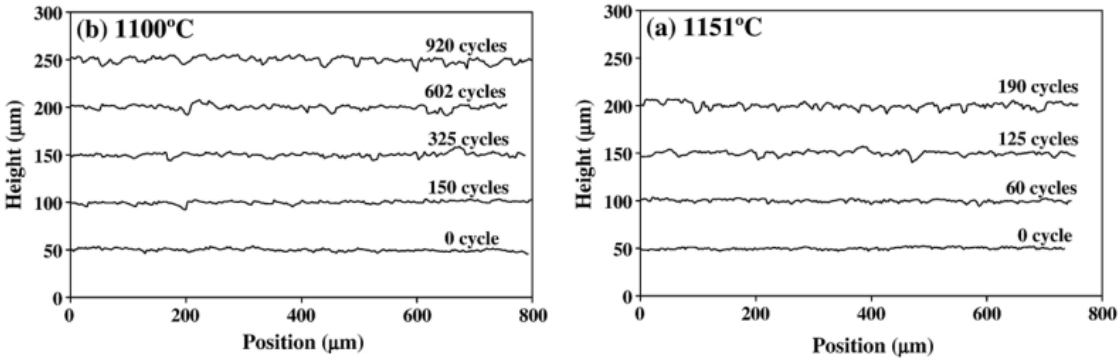


Figure 6: Development of TGO rumpling profiles vs thermal cycles, Wen *et al.*

In regards to damage initiation, mechanisms of micro-crack propagation have also been attributed to phase transformation in the TGO during early stages of thermal cycling. Experiments have shown that tendencies in early TGO growth are in the metastable θ-$Al_2O_3$ and are transformed into the stable α-$Al_2O_3$ with progressive thermal cycling; the changes in TGO volume that accompanies such phase transformations were responsible for incurring local micro-crack initiations (Wen, 2006). For these reasons, the oxidation-resistive capabilities are equally impactful as the primary adhesive properties in engineering the bond coat.

## 2.2 CaO-MgO-$Al_2O_3$-$SiO_2$ (CMAS) attack

CaO-MgO-$Al_2O_3$-$SiO_2$, commonly termed CMAS, refer to the deposition of atmospheric contents onto the surface of TBCs. The ingested sand particles and debris in the hot gas path melt onto the TBC, and its wetting properties facilitate foreign object damage (FOD) due to CMAS. CMAS-related degradation can be categorized into thermomechanical and chemical damage (Vidal-Setif, 2012). Especially in the case of EB-PVD TBCs, the molten CMAS can permeate through the columnar structure as far as the TBC thermal gradient allows (Fig. 7); upon cooling, the solidification of CMAS trapped within the pores can reduce the overall strain tolerance of the TBC. This is primarily due to substantial differences in coefficient of thermal expansion between CMAS and TBC (Chen, 2006).

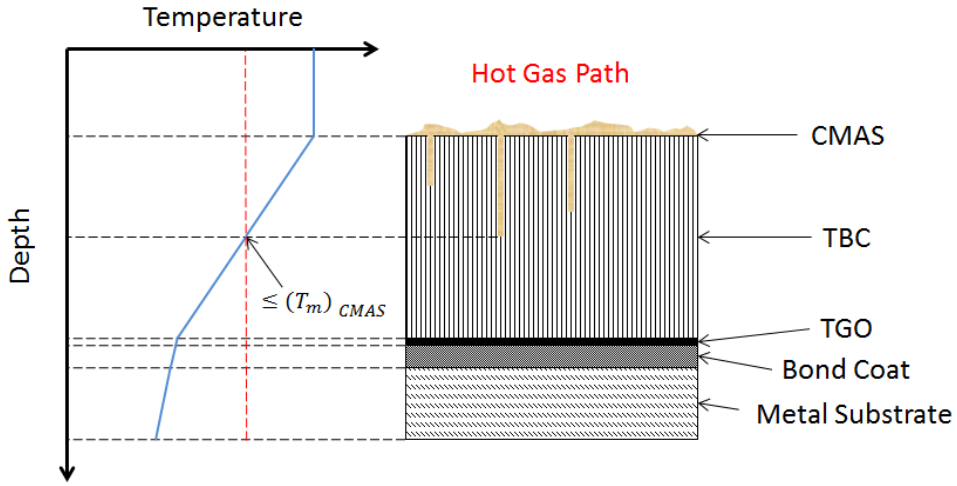


Figure 7: Schematic of CMAS attack on EB-PVD TBC; molten CMAS invades through the porous TBC as far as the temperature gradient allows.

Chemical interaction between CMAS and TBC, although less severe, induce changes in the fine columnar microstructure of EB-PVD TBCs (Vidal-Setif, 2012). Thus, CMAS-resistant coatings have been of interest; recent developments include additional layers equipped with non-wetting characteristics to counteract CMAS deposition, and sacrificial coatings on TBC surface devised to prevent CMAS to liquefy on TBCs. However, particular challenges involve incorporating such developments onto complex topology of EB-PVD TBCs (Rai, 2010).

### 2.3 Laser-induced Breakdown Spectroscopy

LIBS is another optical technique, but unlike PLPS, its objective is ablation by laser. Initiated by a laser pulse energy higher than the breakdown energy of the sample material, the focused laser contact ionizes the surface as well neighboring molecules (Pasquini, 2007). The immediate shockwave of energy is capable of vaporizing small fragments of mass (100 ng to 1 μg, depending on the composition and laser power) at which plasma occurs; such plasma may contain free neutral atoms, ions, molecular fragments, as well as free electrons (Pasquini, 2007). The particle interactions involved in absorption of laser energy by the free electrons, well-described in the realm of quantum physics as the inverse Bremmstrahlung process, effectively accelerates these electrons. Within the duration of the laser pulse, the plasma can be momentarily sustained at which the ionized species can stabilize by seizing the free electrons upon particle collisions (Pasquini, 2007). The described interactions result in species-based deterministic coloration of the plasma plume that can be observed through a high-resolution spectrometer. The received LIBS spectra can be used to identify constituents of interest, and the LIBS schematic is drawn in Fig. 8.

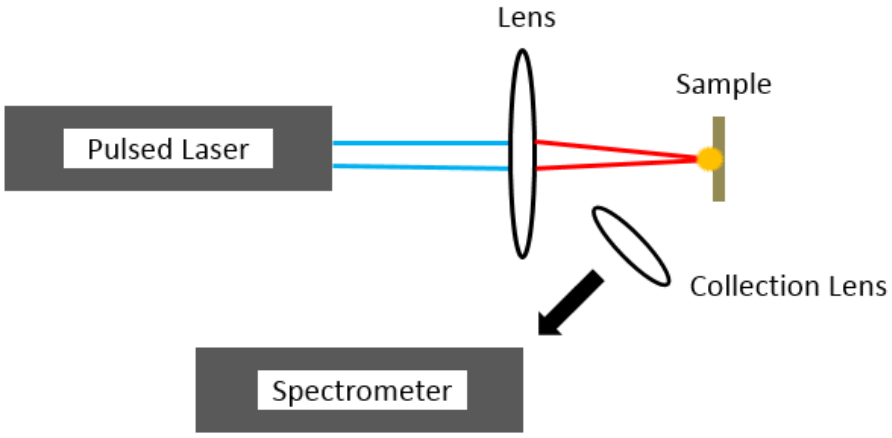


Figure 8: LIBS schematic.

LIBS has been previously used to identify the individual layers of the TBC system (Hawron, 2014).

2.4 Photoluminescence Piezospectroscopy (PLPS)

PLPS is an optical diagnostic technique that allows a variety of TBC system assessments, including APS and EB-PVD TBCs. In PLPS, a visible light source is guided to the TGO, as shown in Fig. 9, where chromium ions undergo photoexcitation that result in a fluorescence at increased wavelengths; this fluorescence is observed through a spectrometer in which data analysis can be performed afterward. The porosity of EB-PVD TBCs facilitate PLPS by functioning as waveguides for the light sourced ($\geq$ 300 μm), whereas PLPS on APS TBCs are limited in that regard ($\leq$ 75 μm) (Gell, 2004).

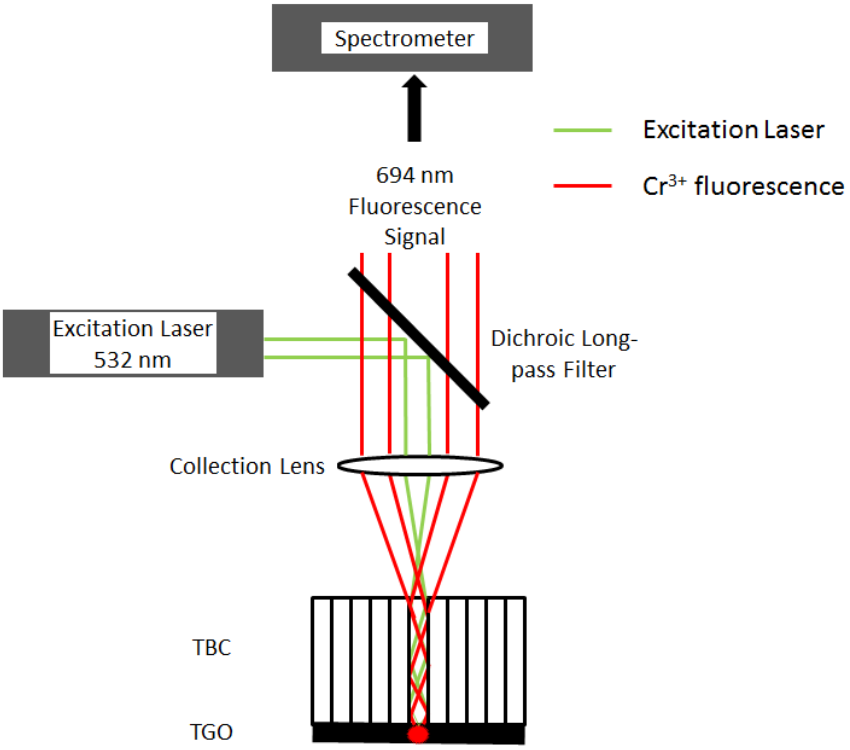


Figure 9: PLPS schematic, Hawron *et al.*

The principal application for PLPS involves TBC lifetime evaluation and failure prediction, and is enabled by paramount findings—stressed alumina within TGO exhibited chromium peak shifts relative to an unstressed alumina reference as shown in Fig. 10 $\left(\text{Note: Wavenumber} = \frac{1}{\text{Wavelength}}\right)$.

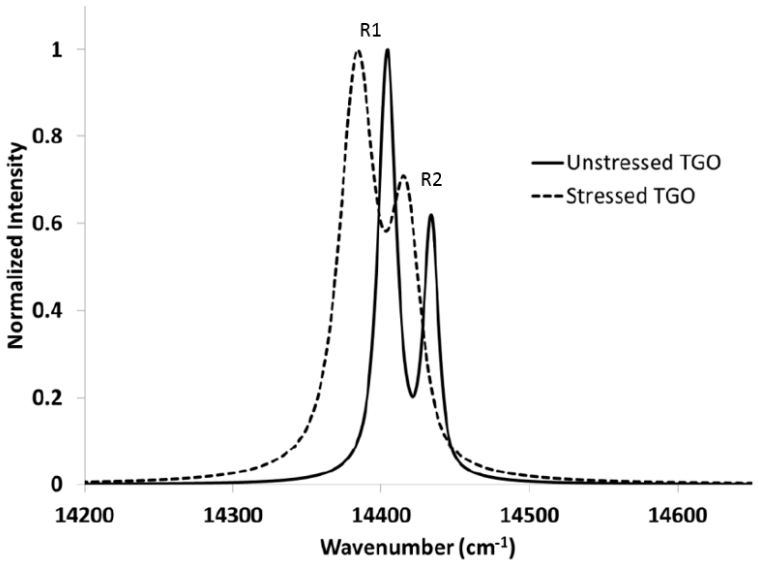


Figure 10: Fluorescence peak shift correspondent to elevated stress levels in TGO, Hawron *et al.*

The chromium fluorescence spectrum consists of R1 and R2 peaks which are typically shifted to higher frequencies during thermal aging indicative of compressive stress. Furthermore, the R2 peak shift has been determined to have a linear relation to the magnitude of the compressive stress (Zhao, 2006). A trend has been identified regarding stress values corresponding to coating life fraction, as shown in Fig. 11. For data presented in Fig. 11, the temperatures and cyclic patterns were a simulation of engine operation, and the life fraction was normalized to unity at incidence of coating spallation. These results allowed remaining life prediction of similar type TBCs in service (Wen, 2006).

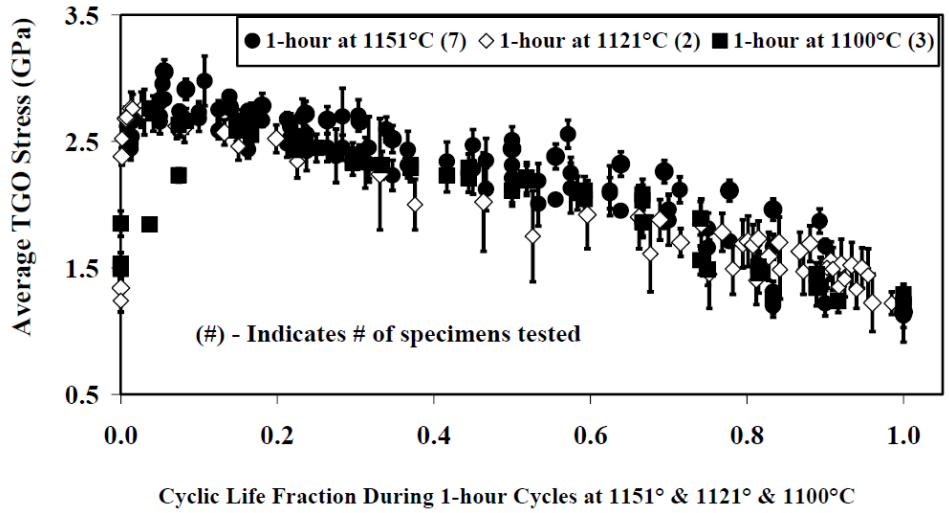


Figure 11: Scatter data of measured TGO stress vs coating life fraction, Wen *et al*.

Because PLPS could be performed on EB-PVD TBCs without damaging the coating, it has been classified as a non-destructive evaluation (NDE).

## 2.5 Fluorescence Interference

During PLPS on engine-run blades, the source of photoexcitation must penetrate through CMAS and TBC and arrive at TGO undisturbed—to necessitate reliable assessments, fluorescence must occur at the stressed TGO only. Otherwise, the collected spectrum may be distorted resulting in false measurements, or, in extreme cases, unreadable measurements. To preserve the benefits of the NDE, several solutions have been developed to permit PLPS on such samples.

2.5.1 Laser-induced Breakdown Spectroscopy (LIBS) for CMAS cleaning

For engine-run blades, CMAS tends to envelop and clog the pores of EB-PVD TBCs, as shown in Fig. 12. CMAS, as the term suggests, partially comprise of alumina; because photoexcitation is intercepted at this outermost layer, the received PLPS spectrum often displays little to no shifts in alumina $Cr^{3+}$ peaks providing deceitful results.

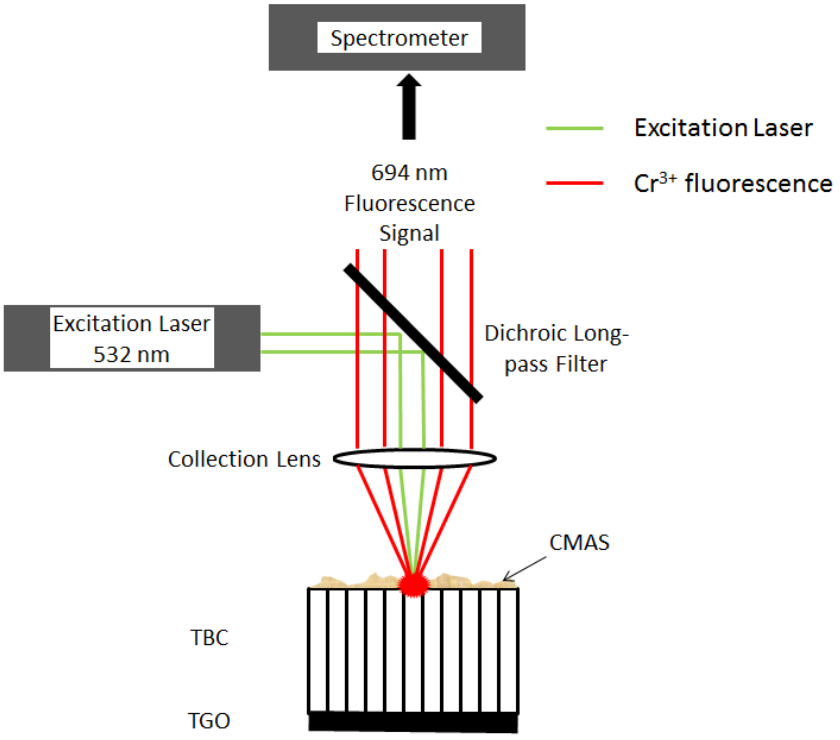


Figure 12: CMAS interference: The excitation laser is intercepted at the outermost CMAS.

In a previous experiment, a solution was developed for CMAS interference; by using a technique known as Laser-induced Breakdown Spectroscopy (LIBS) with cross-correlation monitoring, CMAS could be cleaned off the surface while incurring minimal damage to the underlying TBC (Majewski, 2011). The successful development of reliable CMAS removal via laser cleaning enabled routine PLPS procedures on CMAS contaminated samples (Majewski, 2012).

2.5.2 Time Gated PLPS

In typical EB-PVD blade samples, where the TBC is entirely made of YSZ that does not fluoresce near chromium R1-R2 doublet, the light source can freely travel through the columnar waveguides. However, with continual developments in regards to TBC compositions, as well as unintended impurities that may occur, such modifications may intercept photoexcitation much like in the case of CMAS interference. However, with the source of interference inherent in the coating composition, as shown in Fig. 13, as opposed to at the surface from foreign material, LIBS can no longer be used to physically separate the unwanted fluorescence.

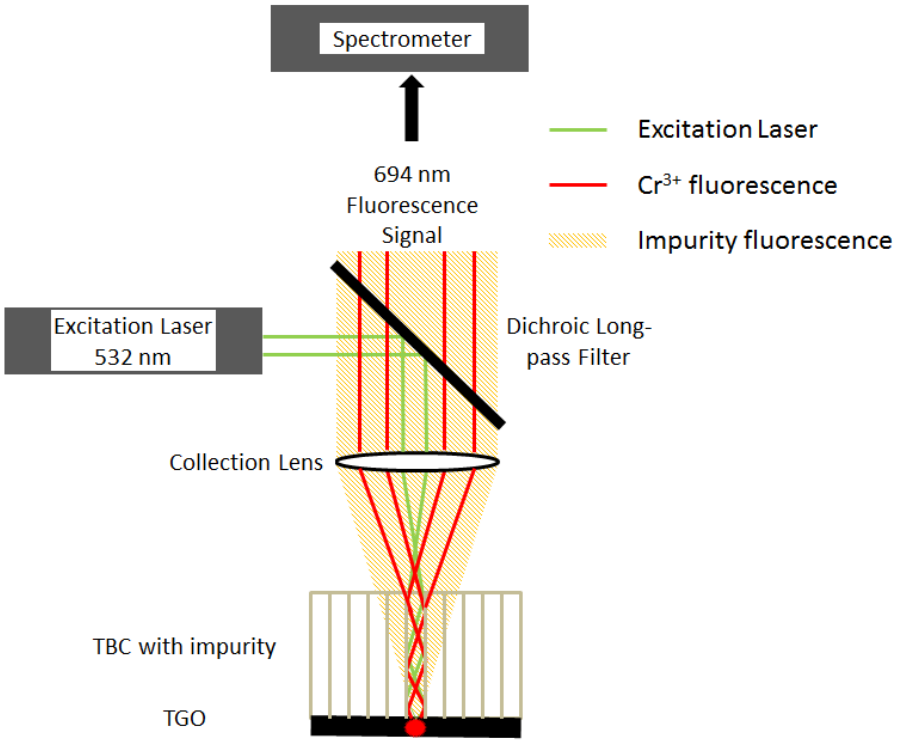


Figure 13: TBC impurity interference: fluorescence occurs along the columnar walls of contact. The collected fluorescence from the interference overwhelms chromium fluorescence that is of interest.

Time gating, or obtaining a time-resolved image, is a technique tailored towards selective image acquisition in the time domain. For mixed signals, assuming each of the signal strengths and time dependence are sufficiently dissimilar (typically in signal decay), time gating exerts data collection where the discrepancy between the mixed signals are at its maximum. Time gating has broad applications in image processing across various disciplines—medical imaging in radiotherapy (Sharp, 2004), flame

kernels involved in ignition (Spiglanin, 1995), as well as fluorescence lifetime imaging (De Grauw, 2001). In regards to PLPS, time gating was also qualified; by exploiting the time dependencies of multiple fluorescence signals, the desired TGO spectrum could be extracted while discarding interference in coating impurities. This work is discussed in detail in Chapter 5.

## 2.6 Proper Orthogonal Decomposition (POD)

The unique compositions of CMAS, TBC, TGO, bond coat, and the metal substrate are reflected in their spectral features. For data analysis that is heavily concentrated around spectra, which are essentially vectors in a simplistic sense, powerful statistic tools become a necessity. Proper Orthogonal Decomposition (POD), also known as Principal Component Analysis (PCA), is a linear decomposition technique similar to Fourier decomposition. However, unlike Fourier decomposition that utilizes predefined sinusoidal functions, POD extracts its own functions (also known as proper orthogonal modes, or POMs) from the presented data set (Rathinam, 2003). POMs are computed via singular value decomposition (SVD), such that the least number of modes are required to best represent the original data set, thereby considerably reducing the number of dimensions of the solution set (Chatterjee, 2000).

POD has been used to create modes (or functions) for CMAS and TBC from their reference spectra, and these modes were exercised in CMAS monitoring during laser ablation; results showed that the POMs, due to their orthogonality, were a substantial improvement to the raw reference cross-correlation (Hawron, 2014). POD has also been used for bond coat detection and TBC removal as an extension to CMAS cleaning; due to excessive spectral similarities between the (Pt, Ni)Al bond coat and the underlying Nickel Superalloy substrate, a simple cross-correlation could not reliably detect bond coat during LIBS and a robust drilling stop criterion could not be established for TBC removal without bond coat damage. The spectral similarities accounted for over 90% of the cross-talk between the LIBS references, and thus POD was applied to differentiate this data set by establishing orthogonality (Hawron, 2014).

Through similar implementation, POD can also be used to decompose CMAS into its major constituents. In a previous study, CMAS speciation was attempted using a Least Squares Fit (LSF) algorithm with the reference spectra obtained through LIBS on constituent samples (Lake, 2012). Much like in the results demonstrated by Hawron *et al.* regarding CMAS cleaning, POD has shown improvements in CMAS speciation by achieving mode orthogonality. This work is discussed in detail in Chapter 5.

## 3. Experimental Setup

Photoluminescence Piezospectroscopy (PLPS) and Laser-induced Breakdown Spectroscopy (LIBS) are the primary optical diagnostic techniques employed in this thesis for turbine blade evaluation. Each spectroscopic method uses different sets of laser equipment that are oriented in the workspace for interchangeability of experimentation as shown in Fig. 14.

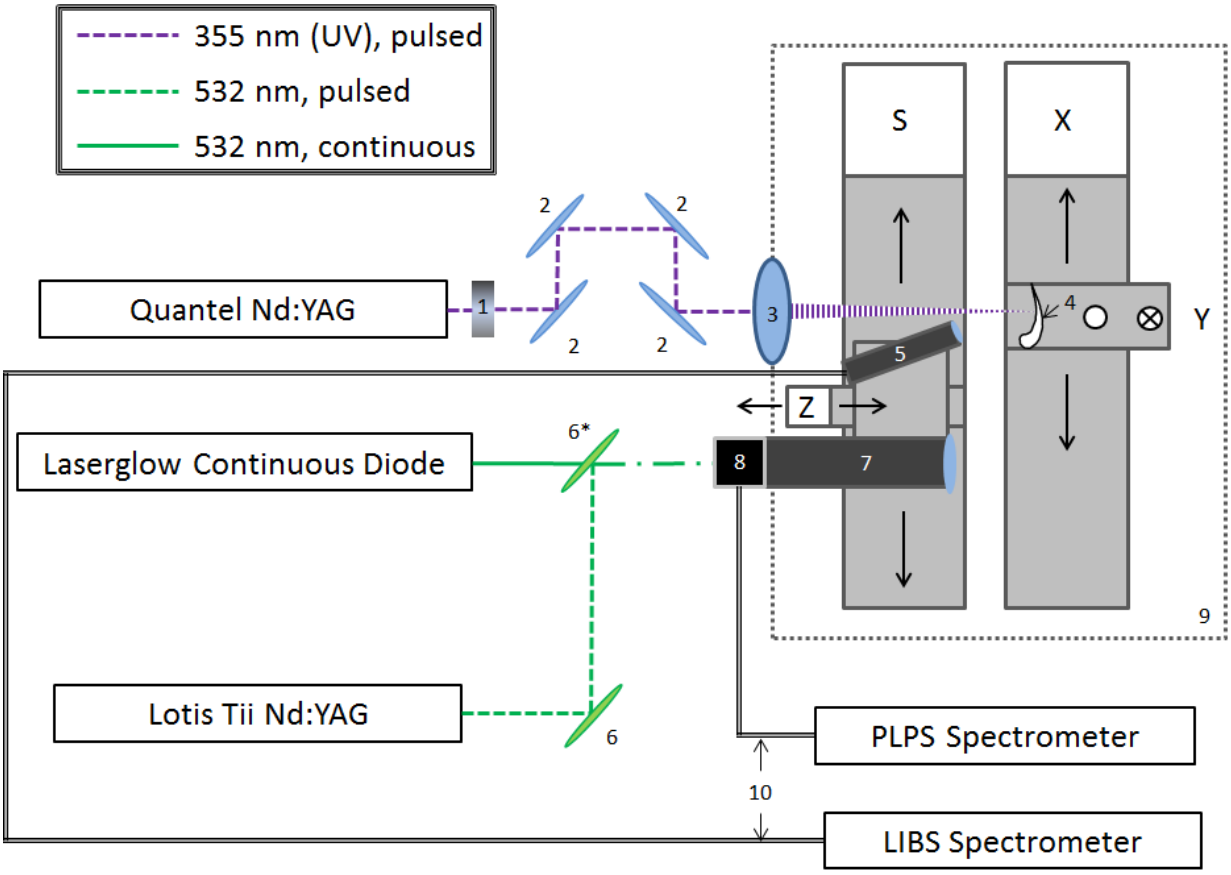


Figure 14: Experimental apparatus. Labeled are 1) shutter, 2) dielectric mirrors to remove residual 532 nm light, 3) lens, 4) target blade, 5) LIBS collection objective, 6) 2nd harmonic mirrors (6* can be removed for the continuous diode laser), 7) PLPS collection objective, 8) wavelength division multiplexer (WDM), 9) translational stage (X, Y, S, Z), and 10) multimode optical fiber cables.

### 3.1 Laser-induced Breakdown Spectroscopy (LIBS)

During Laser-induced Breakdown Spectroscopy (LIBS), the frequency-tripled (3rd harmonic) 355 nm output from the Quantel Nd:YAG laser is guided through dielectric mirrors to remove residual 532 nm laser light. The resulting laser is focused through a lens and directed at the target for ablation. The

Nd:YAG laser is pulsed with a repetition rate of 20 Hz, a pulse width of 5.22 ns, and energy of 17 mJ/pulse. The achieved focused spot size is approximately 400 μm in diameter achieving a peak power density of approximately 26 MW/mm$^2$. This pulse energy was selected based on a series of previous experiments regarding CMAS cleaning (Majewski, 2011); low pulse energies yielded ineffective CMAS removal whereas high pulse energies, due to the overwhelming laser-induced shockwave on the target surface, caused severe coating damage during the cleaning process. In order to achieve the appropriate power density with respect to the ablation spot size, the placement of the preceding lens was considered (Hawron, 2014).

For each laser pulse, the light emitted by the ejected plasma plume is collected within a fiber-optic coupled LIBS objective and directed to an Ocean Optics 2000+ spectrometer (calibrated to 400 – 600 nm). The duration of spectral collection, defined as the integration time, is set to 50 ms correspondent to the Nd:YAG pulse repetition rate, and the spectrometer collection is initiated through a trigger-based Q-switch transistor-transistor logic (TTL) digital output per laser pulse. A delay between the Q-switch trigger and the spectrometer trigger is implemented to account for inherent offsets in digital communication among instruments.

The Quantel Nd:YAG laser is equipped with a low energy configuration for alignment purposes. Although, the alignment of the laser path may be a straightforward process, the alignment of the LIBS collection objective can be elusive. It has been determined that directing the LIBS objective towards the center of the laser-induced plasma plume is preferable over the ablation crater (Hawron, 2014).

The translational stage is driven by individual motors that can be controlled (to the order of $10^{-3}$ mm) during LIBS. The motors are programmed for steady motion during raster scans, supplemented with shutter control to avoid uneven ablation along the edges of the cleaning area. Promising results for effective CMAS removal have been demonstrated, as shown in Fig. 15 (Hawron, 2014).

Figure 15: Demonstration of CMAS cleaned area using LIBS paired with motor and shutter control. The ablated area is ready for stress measurements via PLPS, Hawron *et al.*

The described scan procedure is replicated for CMAS speciation on engine-run blades during LIBS in Chapter 5.

## 3.2 Photoluminescence Piezospectroscopy (PLPS)

During Photoluminescence Piezospectroscopy (PLPS), the Laserglow continuous diode laser provides the necessary frequency-doubled ($2^{nd}$ harmonic) 532 nm for $Cr^{3+}$ fluorescence. The continuous diode is capable of a 500 mW maximum power that is guided to the wavelength division multiplexer (WDM). The WDM is privileged by its ability to carry different wavelengths of laser light bi-directionally, as shown in Fig. 16.

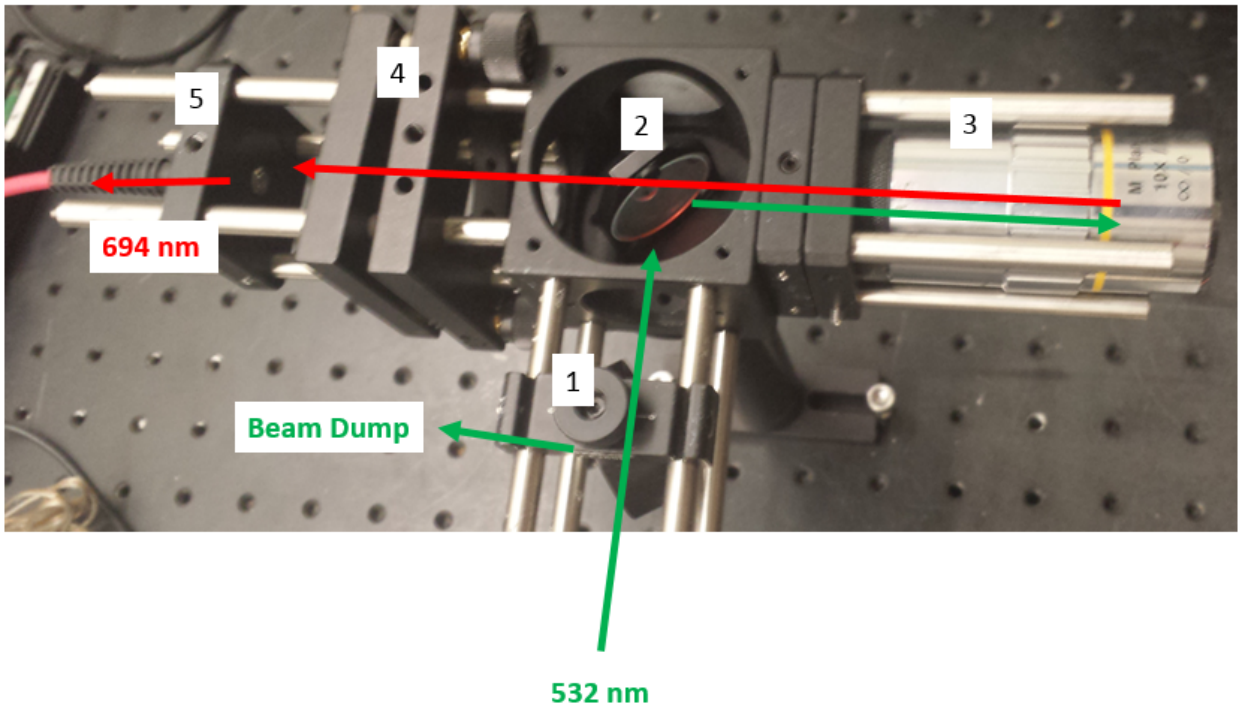


Figure 16: Wavelength Division Multiplexor (WDM). Labeled are 1) beam-splitter, 2) dichroic mirror (long-pass, 638 nm cutoff), 3) PLPS objective, 4) lens placed in an adjustable mount, and 5) fiber coupling.

The beam-splitter allows tolerable reduction in laser power to avoid damage to optical equipment, the long-pass dichroic mirror allows reflectivity at 532 nm and transmissibility at 694 nm for bidirectional light passage, and the PLPS objective focuses the excitation laser onto the target. The target surface is placed normal to the incoming focused laser within a working distance of 35 mm achieving a spot size of approximately 180 μm. The resulting fluorescence is accepted through the same PLPS objective, transmitted through the dichroic mirror, and guided to the outlet fiber cable. The fiber cable directs the collected fluorescence to the Ocean Optics USB4000 spectrometer (calibrated to 665 – 720 nm) used for measurement of the chromium fluorescence spectra. The following PLPS setup has been validated through paralleled measurements via Raman Microscopy at the near excitation frequency of 514 nm (Hawron, 2014).

3.3 Time Gated PLPS

In time-gated PLPS, the received fluorescence is time-resolved prior to being spectrally resolved. The Lotis Tii Nd:YAG pulsed laser at a frequency-doubled ($2^{nd}$ harmonic) wavelength of 532 nm is used to excite the $Cr^{3+}$ ions in place of the continuous diode; the pulsed configuration allows distinguishability between multiple fluorescence sources in the time domain. Equipped with a 14 ns pulse width and repetition rate of 10 Hz, the Lotis Tii Nd:YAG is capable of delivering a maximum energy of 230 mJ/pulse at the $2^{nd}$ harmonic. To avoid possible ablation during PLPS interrogation yet preserve enough laser power for sufficient measurements, the applied pulse energy is reduced to approximately 70 mJ/pulse achieving an approximate average power of 70 mW and peak power of 3.6 MW. The peak power determines the occurrence of ablation, and the average power constitutes the fluorescence signal strength; laser pulse energy could not be further increased without coating damage, and could not be further decreased without severely taxing signal intensity. The limitations due to the pulsed energies for Lotis Tii Nd:YAG allowed a minimum spot size of 2 mm in diameter for measurability; the lower average power relative to the Laserglow continuous diode (by a factor of 10) required compensation in increased area of interrogation for reliable measurement of the chromium spectra. Although it is preferable to tighten the focused spot size to account for TGO stress variability, previous experiments have shown that this variability was generally not significant during PLPS over an area of 2 $mm^2$ (Hawron, 2014).

Prior to applying time-gated PLPS to actual hardware, a pre-experimental confirmation was conducted to ensure its viability by verifying a sufficient difference between fluorescence decay behaviors of chromium and TBC interference. In this confirmation test (Fig. 17), the actual fluorescence spectrum is not collected; rather, the fluorescence decays are observed through an oscilloscope. In this experiment, a set of new target items are required including individual unmixed samples comprised of the respective fluorescence sources. A photomultiplier tube (PMT) is also required for faster resolution of the fluorescence signal.

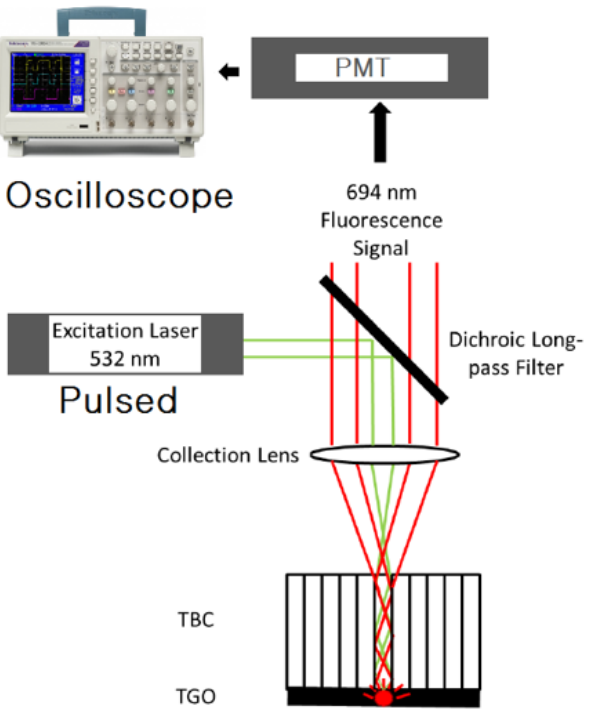


Figure 17: Schematic of modifications to PLPS for observation of fluorescence decay.

PMTs are vacuum phototubes capable of converting any detected light into current through the inlet photocathode (Fig. 18). As a result of incoming photons received at the photocathode window, electrons are ejected at the opposite end via photoelectric effect. The number of electrons multiply (secondary cascade emission) and accelerate within the tube pathway through consecutive electron multiplier dynodes, with each subsequent dynode possessing greater voltage potential. The voluminous electron flow is received at the anode coupled through a resistor to connector pins that allow fluorescence decay observations in terms of voltage through an oscilloscope.

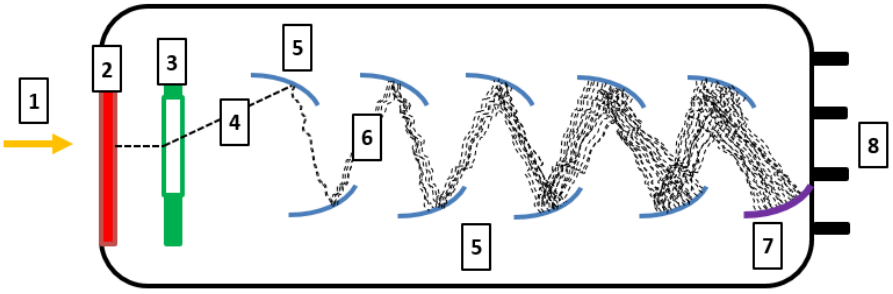


Figure 18: Schematic of a photomultiplier tube (PMT). Labeled are 1) detected light, 2) photocathode, 3) focusing electrode, 4) primary electron, 5) dynodes, 6) secondary cascade emission, 7) anode, and 8) connector pins.

During time-gated PLPS (after satisfactory confirmation), an image intensifier was installed between the spectrometer and the observing camera. The image intensifier is similar to PMTs in terms of functionality; contained within the vacuum space of an intensifier is a photocathode, but unlike that of PMTs, the ejected electrons are not accelerated via dynodes, but rather towards a microchannel plate (MCP) via high-voltage potential (Fig. 19). Per every electron received at the MCP, thousands of electrons are released on the opposing side via secondary cascade emission where continual voltage-induced acceleration occurs. Through the use of parallel plates as opposed to dynodes, the electron flow preserves collimation (thereby preserving the received image) until it arrives at the phosphor screen that reverts received electrons into photons. The emerging image at the phosphor screen can be captured through a camera, and the corresponding spectrum can be recorded. The image intensifier is equipped with a tunable voltage knob that allows adjustments in the acceleration of electrons, thereby offering amplification control of the image intensity received at the phosphor end.

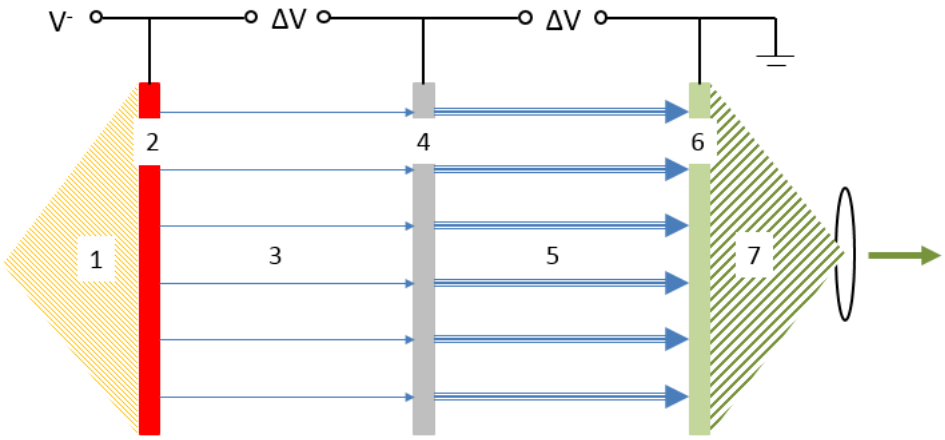


Figure 19: Schematic of an image intensifier. Labeled are 1) incoming image, 2) photocathode, 3) primary electrons, 4) microchannel plate (MCP), 5) secondary cascade emission, 6) phosphor screen, and 7) received image focused and received on camera.

The high-voltage potential that drives electron motion is enabled through a trigger; therefore, the intensifier functions as a 'gate' to either enable or disable fluorescence reception within a pre-specified duration of time. Similar to LIBS where the spectrometer is triggered through a Q-switch output of the laser, a delay generator is employed between the Lotis Tii Q-switch and the image intensifier through TTL communication. The delay generator parameterizes two instances of time relative to its own

incoming trigger (in this case, the Q-switch from the pulsed laser), A and B, at which the intensifier is actuated. The delay generator partakes in two critical tasks: 1) it accounts for inevitable communication delay among instruments thereby facilitating synchronization, and 2) it mediates the intensifier trigger to exert the time-gate. The described time-gated PLPS is illustrated in Fig. 20.

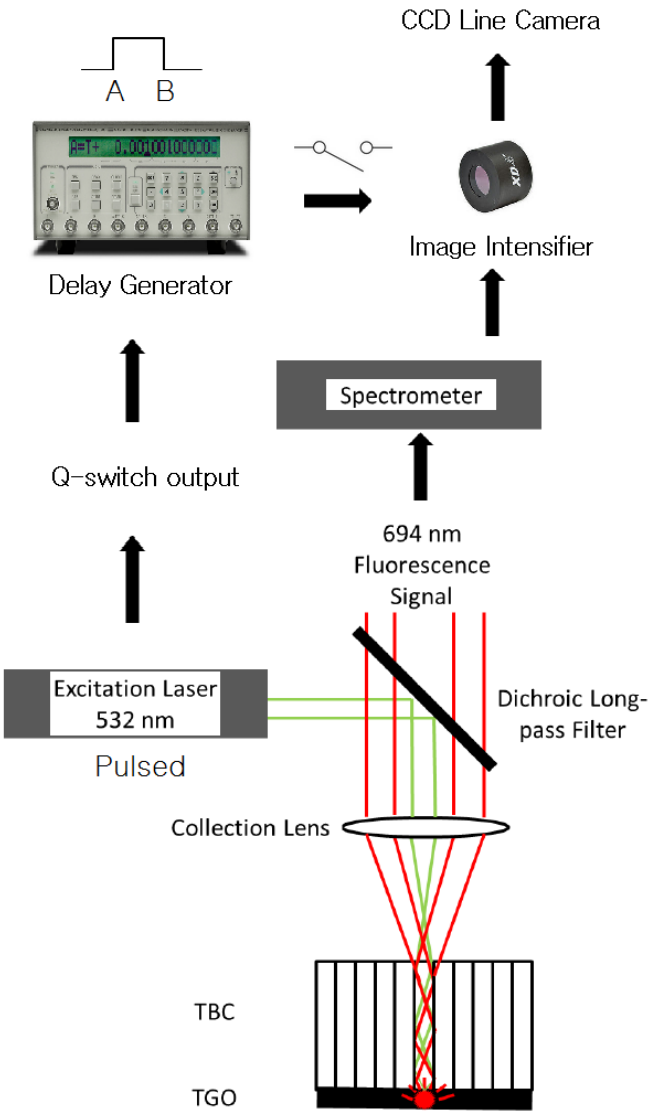


Figure 20. Time-gated PLPS schematic.

The previously employed Ocean Optics 4000 spectrometer is manufactured with a built-in camera, and thus could not be disassembled to install the image intensifier. A Spectra-Physics spectrometer with an appropriate diffraction grating was instead used to observe fluorescence near 694 nm for time-gated PLPS.

**4. CaO-MgO-$Al_2O_3$-$SiO_2$ (CMAS) speciation**

Thermal barrier coatings (TBC) are widely used on turbine blades, vanes and other surfaces in the hot gas path of gas-turbine engines to reduce heat transfer to the underlying metal. During operation, the ingested air will contain a wide variety of atmospheric contaminants that can coat the top surface of the TBC. Typical surface contamination is composed of calcium, magnesium, alumina and silicates (CMAS) (Chen, 2006; Mercer, 2005; Kramer, 2006; Wellman, 2008) as well as lower levels of iron and sulfates (Braue, 2009). The particular composition of the contamination is expected to vary with the operating and atmospheric conditions. In practical usage, CMAS accumulation is abundant such that engine-run TBC coatings are normally fully covered with CMAS. Failure due to CMAS exposure of TBC is a well-recognized problem (Hitchman, 2010).

In addition to potential structural damage, CMAS accumulation can prevent certain non-destructive evaluation of coatings. For example, Photoluminescence Piezospectroscopy (PLPS) utilizes fluorescence from chromium ions present in the thermally grown oxide (TGO) layer in order to measure stresses that correlate to remaining lifespan of a coating (Grabner, 1978; Christensen, 1996; Wen, 2005; Sridharan, 2004; Vaidyanathan, 2001; Wang, 2007). However, because CMAS contaminants also include alumina, the accumulation of CMAS on the outer layer of TBC causes invalid diagnosis (Majewski, 2012; Hansen, 2007).

For these reasons, removal and characterization of CMAS from coated components without damaging the underlying coating is of interest. Laser ablation has been demonstrated as a viable technique for removing the CMAS (Majewski, 2011, 2012). During ablation, laser induced breakdown spectroscopy (LIBS) can be used to monitor the material removal. During the laser excitation, the material subjected to ablation is ionized and dissociated. After the laser excitation is stopped, excess energy is emitted as the atoms returns to their neutral states (Kim, 2012). This emitted light is spectrally resolved and can be used to differentiate atomic composition from unique spectral peaks. LIBS has been used in a wide variety of applications for speciation of the ablated material (Kim, 2012; Multari, 2010; Michel, 2010).

A LIBS approach for removing CMAS from engine-run TBCs has been developed in a previous study (Majewski, 2011). In this approach, the LIBS spectrum collected during material ablation was

compared to reference spectra from both a new TBC with no CMAS and a spectrum representing average LIBS signals from many CMAS samples. Typical measured spectra for CMAS and TBC are shown in Fig. 21.

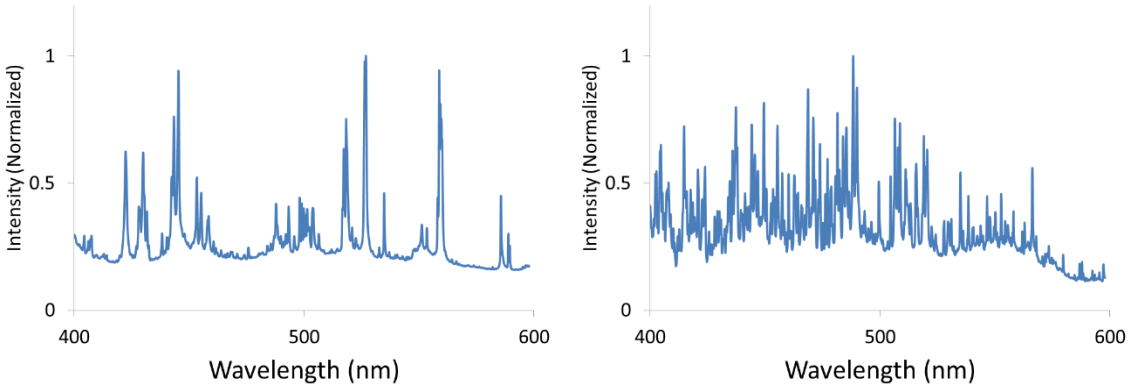


Figure 21: Reference LIBS spectrum for CMAS (left), and TBC (right), Kim *et al.*

As can be seen, there are substantial differences in the spectra. During removal of CMAS, the LIBS spectra are monitored with each laser shot. Examples of spectra as a function of removal depth are discussed in Majewski's (2011) work. When the signal was sufficiently representative of TBC, ablation was stopped. Scanning electron microscopy (SEM) was used on samples before and after CMAS removal to show that local cleaning did not alter the coating (Majewski, 2011). However, no attempt was made to isolate the components of the CMAS signal. In this chapter, additional analysis of the LIBS signal during laser ablation is used to quantify the composition of the contamination. Since the composition can vary with engine and atmospheric conditions, quantifying the deposited material on the TBC can help understanding of deposition processes and the impact of specific contaminants on the TBC durability.

To separate the measured LIBS spectra into their contribution from different atomic species, several approaches can be taken. If all contributing species to the signal are known and have well-characterized LIBS spectra, then a least-squares regression of a measured sample onto the reference spectrum can be used as has been applied to other applications for LIBS spectral analysis (Multari, 2010; Clegg, 2009). However, CMAS consists of several major species as well as an unknown number and distribution of minor contributors. A linear regression has been previously attempted to decompose the CMAS signals onto reference spectra for calcium oxide, magnesium oxide, alumina, and silica. However,

the presence of other components and significant overlapping spectral features led to significant errors in the decomposition (Lake, 2012). In this chapter, proper orthogonal decomposition was used instead to more directly account for unknown contributors to the spectrum permitting quantification of constituents with strong LIBS signals. Proper orthogonal decomposition (POD), also known as principle component analysis (PCA), is a linear decomposition technique that uses the data itself to determine orthogonal modes (OMs). These modes are determined from a singular value decomposition (SVD) of the data and provide the most compact representation of the data set (Liang, 2002). During measurements to characterize a surface, the measured spectrum is decomposed onto the OMs. However, since the OMs are defined mathematically they do not necessarily represent unique species. A process to separate, or renormalize, the OMs so that each mode represents a single contributing CMAS species is described in this chapter. These separated OMs are then used to characterize the CMAS composition across the surface of several engine run TBCs.

## 4.1 CMAS and Constituent Spectra

Figure 22 shows raw spectra from CMAS on an engine-run TBC-coated turbine blade, as well as pure powder samples of CMAS constituents at purity levels of 99.99% obtained from Sigma-Aldrich. Note that:

1) CaO has the largest number of unique peaks in its LIBS spectrum which are clearly represented also in the CMAS spectrum. CaO is readily detectable in any given CMAS sample visually.
2) MgO only has two major peaks in its LIBS spectrum, but the intensities of these peaks are relatively high, which facilitates detection of MgO in the CMAS spectrum as well.
3) $Al_2O_3$ has several unique peaks in its LIBS spectrum, but these are not easily observed in the composite CMAS spectrum relative to the baseline due to inherently weak alumina LIBS signals.
4) $SiO_2$ signals are much lower than the other three CMAS constituents, which is apparent from the large background relative to the weak peaks observed in this wavelength range. This low signal makes $SiO_2$ very difficult to detect in CMAS where there are strong contributions from calcium

or magnesium. In all combined CMAS samples studied in this work, the silica signals are too weak for detailed analysis so only decomposition of the magnesium, calcium and alumina spectra is considered.

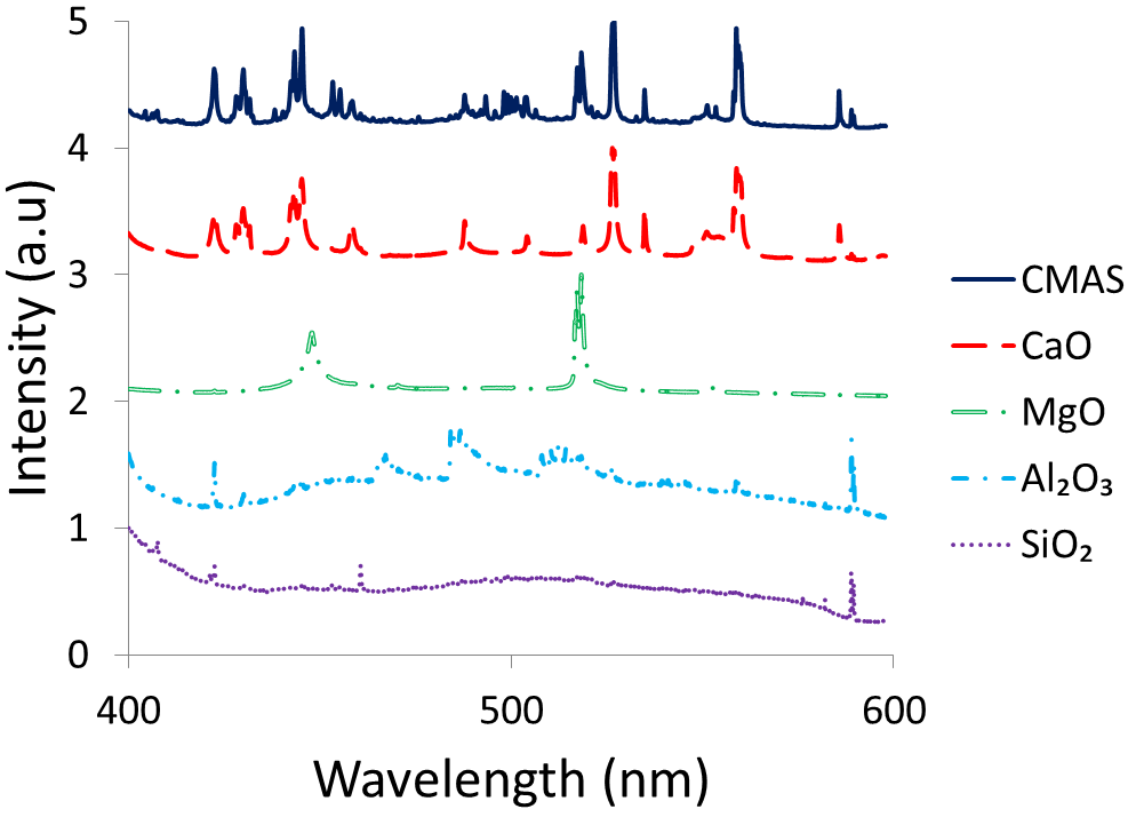


Figure 22: Raw LIBS spectra for CMAS and single compounds of interest. Individual spectra are shifted vertically for clarity, Kim *et al.*

One method of using LIBS for quantitative determination of atomic constituents is to find isolated peaks in the spectra of the constituents and use the magnitude of these peaks (following calibration) to separate the composite measured spectrum. This requires good separation of peaks, which may not always be the case, and takes advantage of only a limited amount of the collected signal. Alternatively, the entire spectrum can be used. In previous work, Majewski *et al.* (2011) used a simple cross-correlation between collected composite CMAS spectra like that shown in Fig. 22 and a reference spectrum to identify the boundary between the CMAS and TBC during CMAS removal. However, this simple cross-correlation can be difficult to interpret quantitatively since the constituent spectra are not

necessarily orthogonal. For example, note in Fig. 22 that both of the major peaks in the MgO spectrum overlap peaks in CaO; thus, the cross-correlation between MgO and CaO is non-zero. Therefore, even for a pure measurement of CaO, a comparison to the MgO spectrum will find non-zero contribution. Table 1 shows the normalized cross-correlation (coefficient of determination) between each of the reference spectra, except silica.

Table 1: Reference to reference cross-correlation, Kim *et al.*

| | Coefficient of Determination ($R^2$) | | | | |
|---|---|---|---|---|---|
| Reference Spectra | | Reference Spectra | | | |
| | | CaO | MgO | $Al_2O_3$ | Sum |
| | CaO | 1 | 0.026 | 0.015 | 1.041 |
| | MgO | 0.026 | 1 | 0.120 | 1.146 |
| | $Al_2O_3$ | 0.015 | 0.120 | 1 | 1.135 |

Note that the sum of these coefficients is not unity, which indicates a non-orthogonal set of data. As an example, the cross-correlation of the CaO reference spectrum and the full CMAS measurement from Fig. 22 was used to estimate the contribution of CaO. This contribution was then subtracted from the CMAS measurement to yield a residual, shown in Fig. 23. This residual of the CaO cross-correlation represents the other known species (MgO and $Al_2O_3$) as well as any contributions from unknown species. This residual has significant non-physical negative values at wavelengths where CaO contributions were overestimated due to the CaO reference spectrum being correlated to other species. Some negative values in the residual are expected due to noise, but the magnitude of these peaks relative to the baseline is as large as the other contributing species. Because the $R^2$ values do not sum to unity, the set of reference spectra cannot be simply used by cross-correlation to decompose spectral data for mixture samples and obtain concentrations of known constituents.

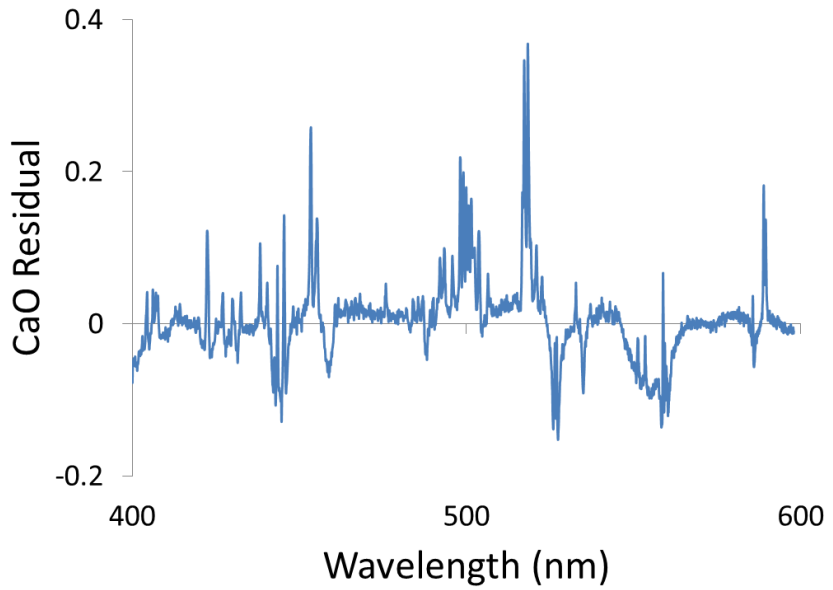


Figure 23: Residual computed from subtracting CaO contributions to CMAS signal using simple cross-correlation to the CaO reference spectrum, Kim *et al.*

As discussed previously, the reference spectra can also be used for a least-squares decomposition of the measured signal. However, in the case of CMAS, additional spectral features not represented by the major species can cause significant errors in the analysis (Lake, 2012). Figure 24 shows a least-squares fit of the reference spectra from Fig. 22 to a representative CMAS measurement.

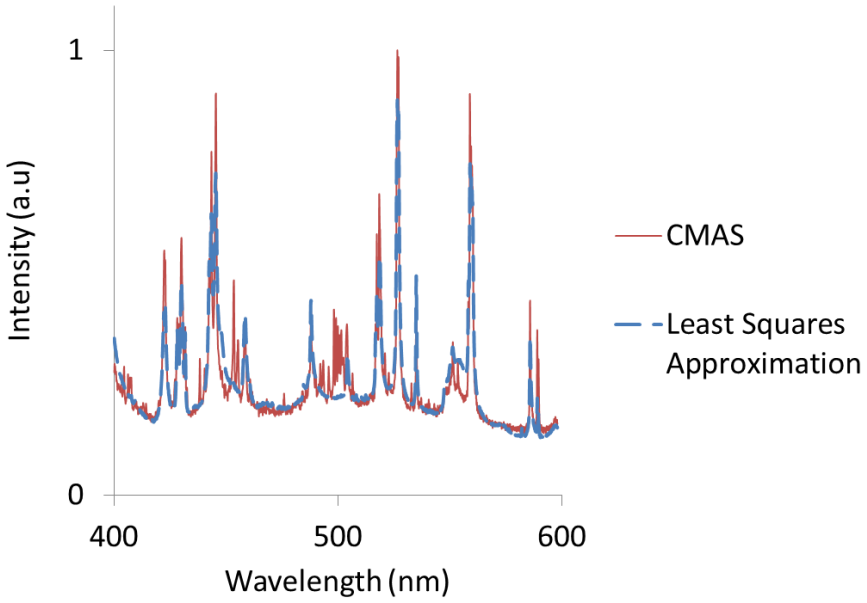


Figure 24: Best fit of reference spectra to CMAS measurement using least squares fit, Kim *et al.*

The resulting fit appears to adequately represent the measured spectrum; however, the CaO contribution, which is the dominant signal in the CMAS measurement, is again found to be overestimated. Figure 25 shows the residual from subtracting the best fit contribution of CaO from the full CMAS spectrum.

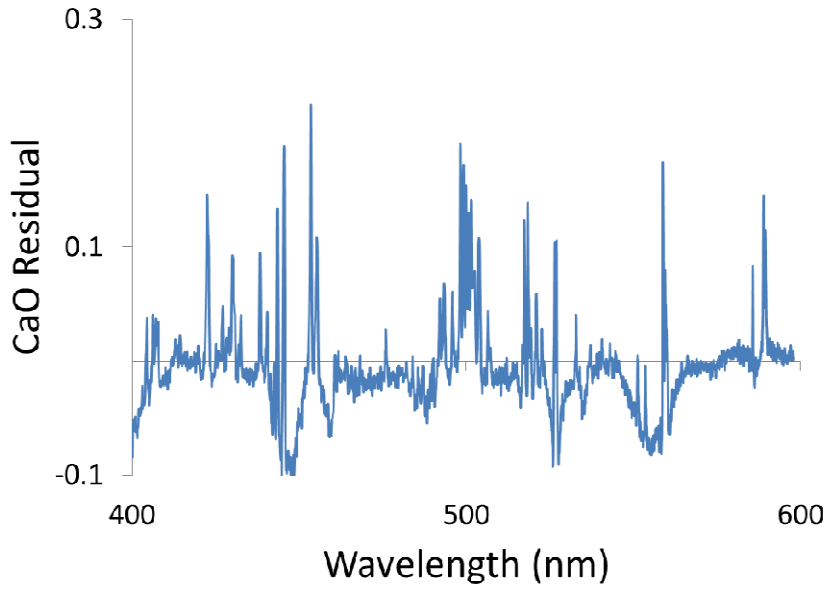


Figure 25: Residual computed from subtracting CaO contribution to CMAS signal using a least squares fit to the CaO reference spectrum, Kim *et al.*

As with the CaO cross-correlation results, the least squares fit residual has negative values from the overestimation of CaO that are too large to enable accurate determination of subsequent species. Proper orthogonal decomposition can instead be used to improve upon this analysis by orthogonalizing the reference spectra, thereby addressing the issue of overlap among CMAS constituent spectra, and separating unknown contributors from the major species.

## 4.2 POD of Constituent Spectra

In this study, POD (also known as principal component analysis, PCA) was used as the primary mathematical tool to extract information from spectral measurements during LIBS. POD was chosen over a least squares fit technique to account for contributions from unknown constituents of CMAS as well as avoid overestimation of constituents. POD can be used to separate unidentified spectral information into

the decomposition's residual (as will be demonstrated in the results section) without affecting the orthonormal modes of spectrally identified species. Because not all of the species contributing to CMAS can be known, the least squares method yielded nonphysical results (Lake, 2012). Furthermore, using POD to extract physically meaningful modes permits data decomposition by cross-correlation which only requires array multiplication to obtain a scalar value as opposed to an iterative fitting. Therefore, POD is computationally efficient and can be utilized in parallel with LIBS experimentation in real-time. We have previously shown that cross-correlation decomposition for CMAS versus TBC can be applied in real time for shot-to-shot assessment of the LIBS signal; however in that work no attempt was made to determine the composition of the CMAS (Majewski, 2011).

POD is a linear decomposition, like Fourier decomposition, where the modes are determined directly from the data to be decomposed (Rathinam, 2003). In this case, the spectra from each constituent element of CMAS are combined into a single matrix, S, of size *m* by *n*, where *n* is the number of unique wavelength values (determined by the spectrometer), and *m* is the number of single spectra included. The data can be decomposed into *m* modes, *M*, each of length *n* and an *m* by *m* matrix of constants, *C*, as

$$S = \sum_{i=1}^{m} C_i M_i \tag{1}$$

Using POD, the mode shapes are computed from singular value decomposition (SVD) such that the least number of modes are required to represent the data set (Berkooz, 1993). Orthogonal modes were computed using SVD from the individual reference spectra for CaO, MgO and $Al_2O_3$, shown in Fig. 26.

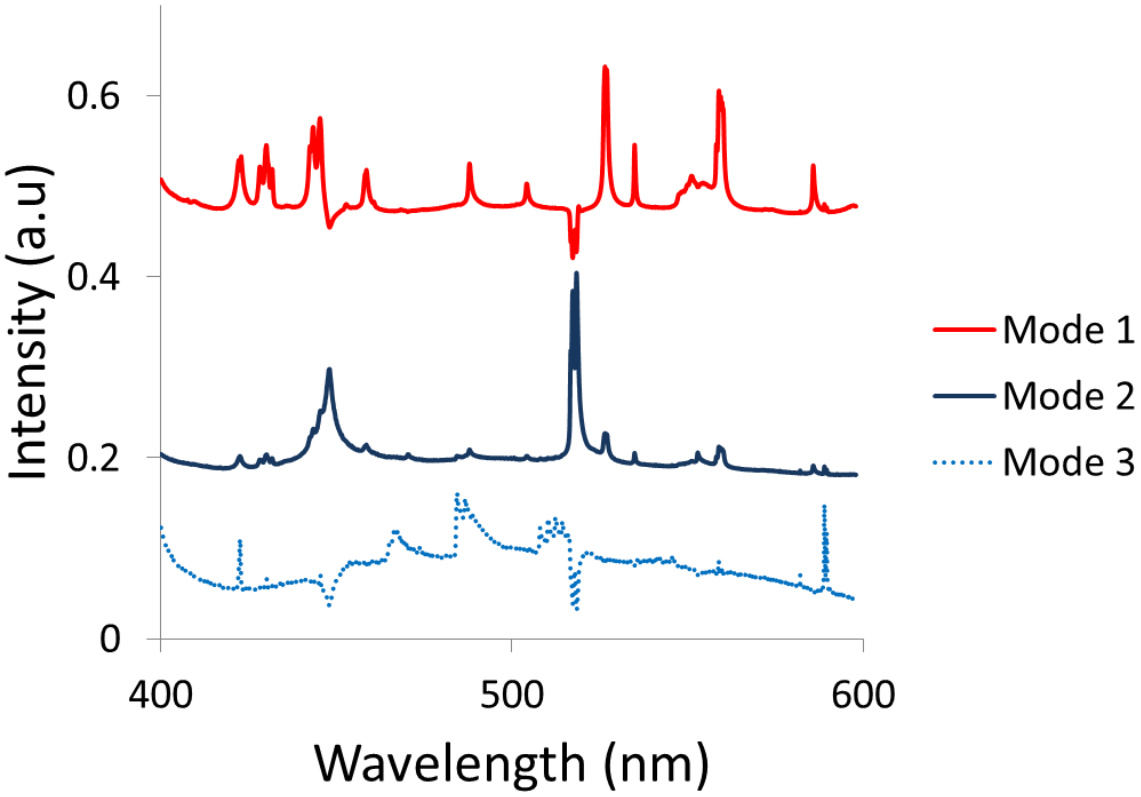


Figure 26: Orthonormal modes for CaO, MgO, and $Al_2O_3$ computed directly from POD, Kim *et al.*

Although the major features of the modes from this POD analysis (Fig. 26) are similar to the directly measured spectra (Fig. 22), the modes are orthogonal such that cross-correlations between any two spectra are identically zero, yet do not uniquely represent each of the single constituents, as shown in Table 2.

Table 2: Cross-correlation of POD modes (Fig. 26) to reference spectra, Kim *et al.*

| | | Coefficient of Determination ($R^2$) | | | |
|---|---|---|---|---|---|
| Orthonormal Modes | | Reference Spectra | | | |
| | | CaO | MgO | $Al_2O_3$ | Sum |
| | Mode 1 | 0.893 | 0.107 | 0.000 | 1.000 |
| | Mode 2 | 0.030 | 0.968 | 0.003 | 1.001 |
| | Mode 3 | 0.007 | 0.154 | 0.839 | 1.000 |

The level of intermixing is also shown graphically in Fig. 26; mode 1 which mostly represents CaO has negative peaks in the locations of the dominant MgO spectral features. If these POD modes are used directly to decompose a measured LIBS spectrum, this spectral cross-talk of over 10% will result in incorrect identification of the underlying components. A secondary procedure was developed in the present case to separate these intermixed features of the modes, while still retaining the orthogonal property of the POD modes.

4.3 Renormalization of Modes

A procedure, referred to herein as "renormalization," was developed to reduce crosstalk in the decomposed spectra. The derivation utilizes a forced linear combination of the initial modes to construct new modes that minimize cross-talk between constituents while maintaining the orthonormal properties with respect to all of the other modes. The renormalization process involves altering some of the mode shapes without violating its orthogonal properties, and it is a straightforward algebraic procedure. For cases such as the present work involving three modes, this process is done iteratively by renormalizing two modes at a time. For the case of renormalizing two mode shapes, the new modes, $M_a$ and $M_b$ can be computed from the original POD modes, $M_1$ and $M_2$ by

$$M_a = A_1 M_1 + A_2 M_2 \tag{2a}$$

$$M_b = B_1 M_1 + B_2 M_2 \tag{2b}$$

where $A_1$, $A_2$, $B_1$, and $B_2$ are constants. The POD modes are orthonormal; that is, $M_1 \cdot M_1 = 1$, $M_2 \cdot M_2 = 1$ and $M_1 \cdot M_2 = 0$. Thus by substitution, the constants must satisfy

$$A_1^2 + A_2^2 = 1 \tag{3a}$$

$$B_1^2 + B_2^2 = 1 \tag{3b}$$

so that the new modes are normal. Likewise, the original POD modes are orthogonal so the constants must also satisfy

$$A_1 B_1 + A_2 B_2 = 0 \tag{4}$$

Thus, the new modes have four parameters, three of which are constrained by orthonormal requirements. The remaining parameter can be freely chosen to minimize cross-talk in the renormalized modes.

The equations above only allow renormalization of two modes. In order to renormalize a set of three or more modes, it is necessary to renormalize multiple times. This process can be analogous to rotational transformations applied to orthonormal directional vectors in 3-dimensional space as shown in Fig. 27. Let the ideal reference spectra for CaO, MgO, and $Al_2O_3$ which have no cross-talk be representative of principal axis in 3-dimensional space. Then, let the resulting mixed modes obtained through POD be a set of orthonormal vectors in this 3-dimensional space. The arbitrary directions of these mode vectors signify mixed contributions from more than one principal constituent. Because renormalization using Eq. (2) operates on two modes at a time, this technique can be analogous to a rotational transformation of two of the mode vectors with respect to the remaining third mode vector. This rotational transformation was applied onto the first two mode vectors holding the third mode vector unchanged, thus all three of the mode vectors retain their orthonormal properties as shown in Fig. 27(b). The parameters $A_1$, $A_2$, $B_1$, and $B_2$ in Eqs. (2)-(4) are analogous to the angle of rotation for a set of vectors; therefore, through careful parameterization, it is possible to align one of the first two modes with the ideal reference spectrum, in this case aligning mode 2 with the ideal MgO spectrum as shown in Fig. 27(b). From there, renormalizing the other two modes (1 and 3) while holding mode 2 fixed yields a set of three orthonormal modes that optimally represent each constituent spectrum as shown in Fig. 27(c).

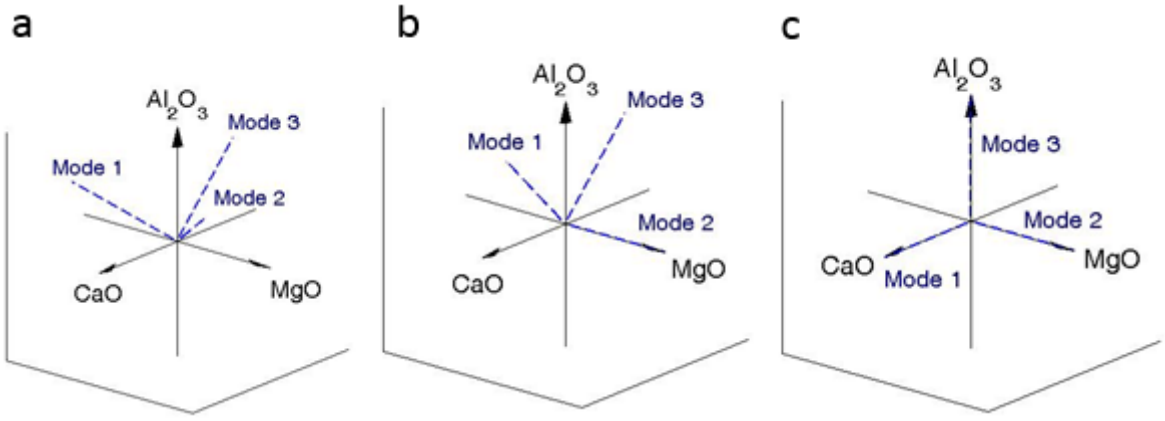


Figure 27: (a) Mixed orthonormal modes directly from POD, (b) modes after 1st renormalization, and (c) modes after 2nd renormalization with minimum cross-talk, Kim *et al.*

This concept was followed in the actual renormalization process; modes 1 and 2 were renormalized first, and then modes 2 and 3. It is also viable to renormalize modes 2 and 3 before modes 1 and 2 to obtain similar results. The order of renormalization yields quantitatively different parameter values but similar separation of modes. In each case, the cross-correlation of the renormalized modes to the pure reference spectra was used to measure the cross-talk between modes.

For this application, was initially parameterized, and the corresponding constants were calculated to satisfy Eqs. (2)-(4). From Eq. (2a), it can be seen that the value of signifies the fragment of mode 1 that is reallocated into a new mode, . Therefore, it is possible to choose values for $A_1$ by identifying peaks that result from cross-talk between original modes of interest as shown in Fig. 28.

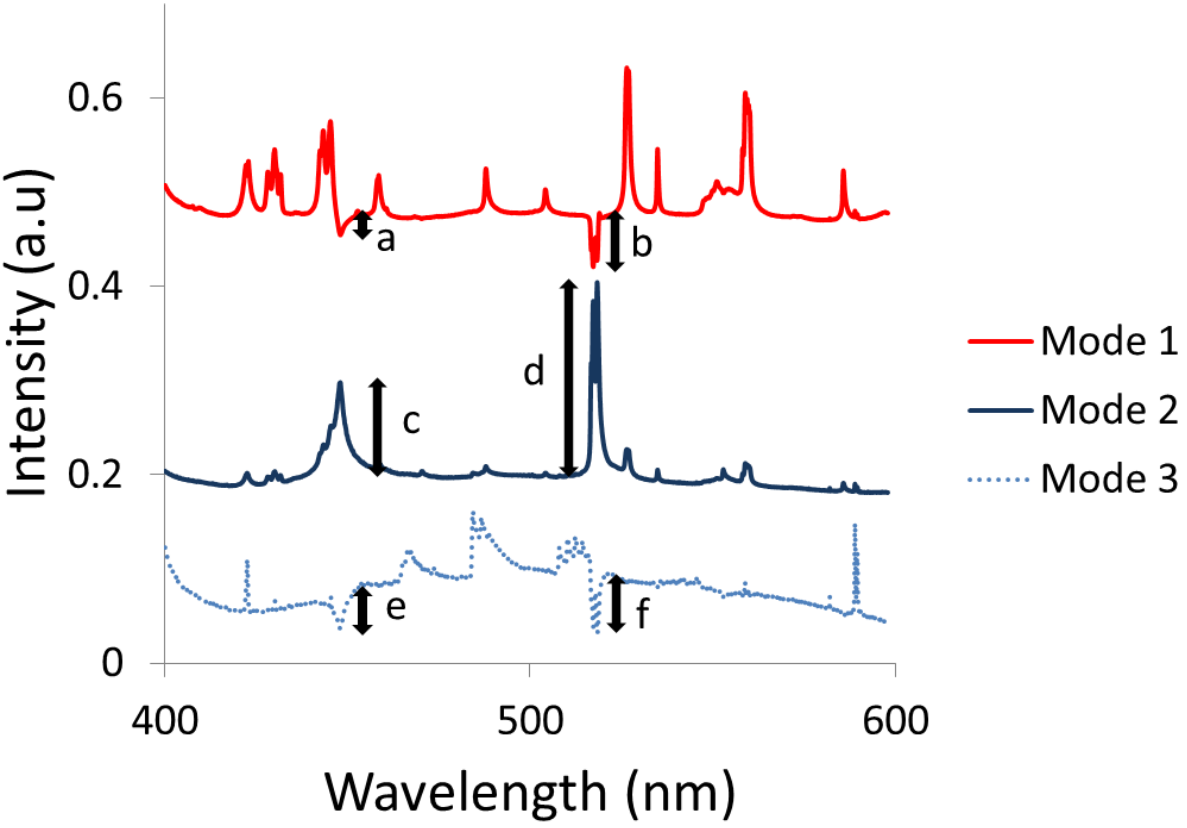


Figure 28: Approximate method for quantifying magnitudes of MgO peaks found in modes 1-3 (Fig. 26), Kim *et al.*

For example, mode 1, primarily resulting from CaO, has two unique peaks at approximately 450 nm and 515 nm that result from MgO. Similarly, mode 2, primarily resulting from MgO, has numerous subtle peaks from CaO. Therefore, these two modes are clearly mixed. In order to choose a reasonable value for , the relative intensities of MgO peaks were taken into consideration, labeled *b* and *d* in Fig. 28. Peaks *b* and *d* have peak intensities of approximately -0.05 and 0.2, respectively. Taking the absolute value of the ratio of these peak intensities, calculated to be 0.25, provided a general approximation of a reasonable value. values from 0.1 to 0.3 were used to compute renormalized modes. As is gradually increased, the MgO peaks from mode 1 begin to subside and there is less cross-talk between the modes. However, if $A_1$ is increased too much, the CaO peaks begin to resurface in mode 2. By computing the cross-correlation between the renormalized modes and the reference spectra for each value of $A_1$, a minimum cross-talk was identified when $A_1$=0.179. The resulting modes after renormalization are shown in Fig. 29.

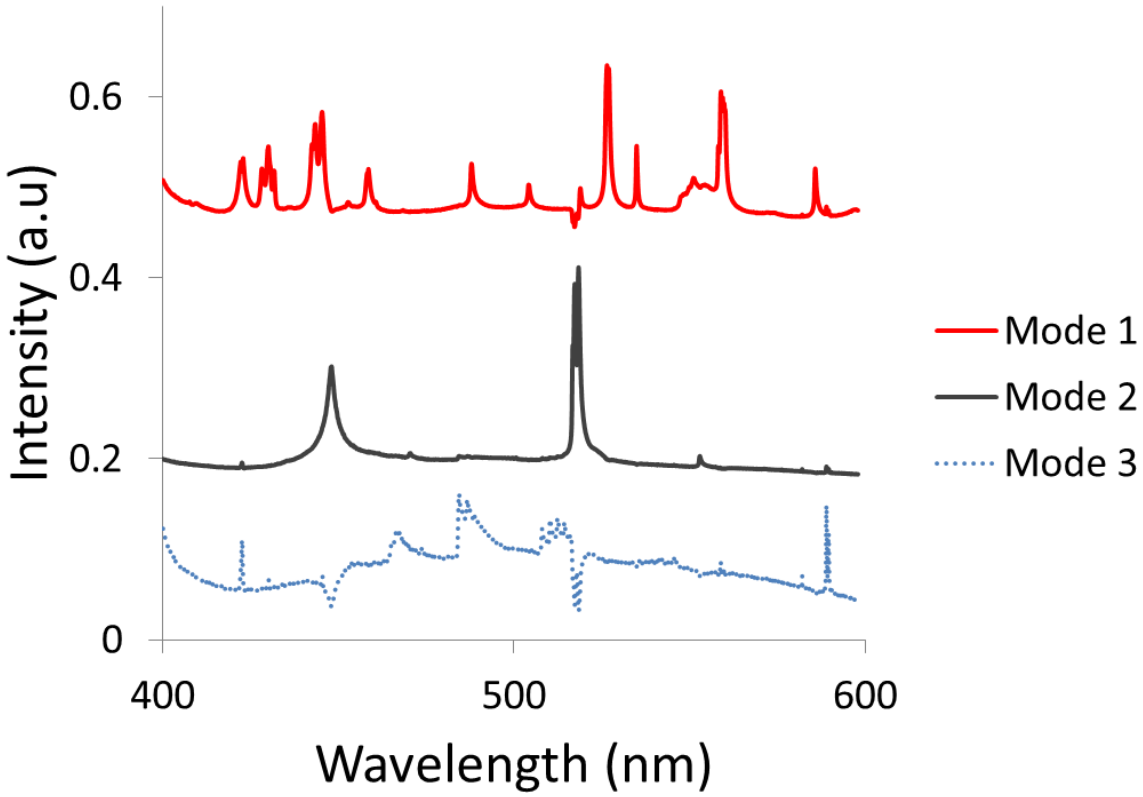


Figure 29: Renormalized modes 1 and 2, at , Kim *et al.*

Table 3 shows the repeated calculation of the $R^2$ values for the modes from Fig. 29, and demonstrates that reduced cross-talk between mode 1 and mode 2 was achieved as a result of renormalization.

Table 3: Cross-correlation of modes (Fig. 29) to reference spectra after first renormalization, Kim *et al.*

| | | Coefficient of Determination ($R^2$) | | | |
|---|---|---|---|---|---|
| Orthonormal Modes | | Reference Spectra | | | |
| | | CaO | MgO | $Al_2O_3$ | Sum |
| | Mode 1 | 0.979 | 0.021 | 0.001 | 1.001 |
| | Mode 2 | 0.000 | 0.997 | 0.003 | 1.000 |
| | Mode 3 | 0.007 | 0.154 | 0.839 | 1.000 |

Note that throughout this process, mode 3 remains unchanged (as well as its $R^2$ values) because Eqs. (2)-(4) only consider two modes at a time and orthogonality with mode 3 is unaffected.

Next, modes 2 and 3 were renormalized. Figure 28 shows that there are also MgO peaks in mode 3. The ratios between *d* and *f* peaks are taken into consideration when parameterizing $A_1$ for the second renormalization. However, the difference in the second renormalization is that mode 2 is already representative of the MgO spectrum; therefore, it is reasonable to expect a value for $A_1$ that is close to 1, such that most of the spectral features in mode 2 are conserved. As before, a range of $A_1$ values were considered and the renormalized modes were compared to the reference spectra for each pure species to find an optimum value. For a case of $A_1$=0.906, the resulting renormalized modes are shown in Fig. 30, and the corresponding $R^2$ values are shown in Table 4.

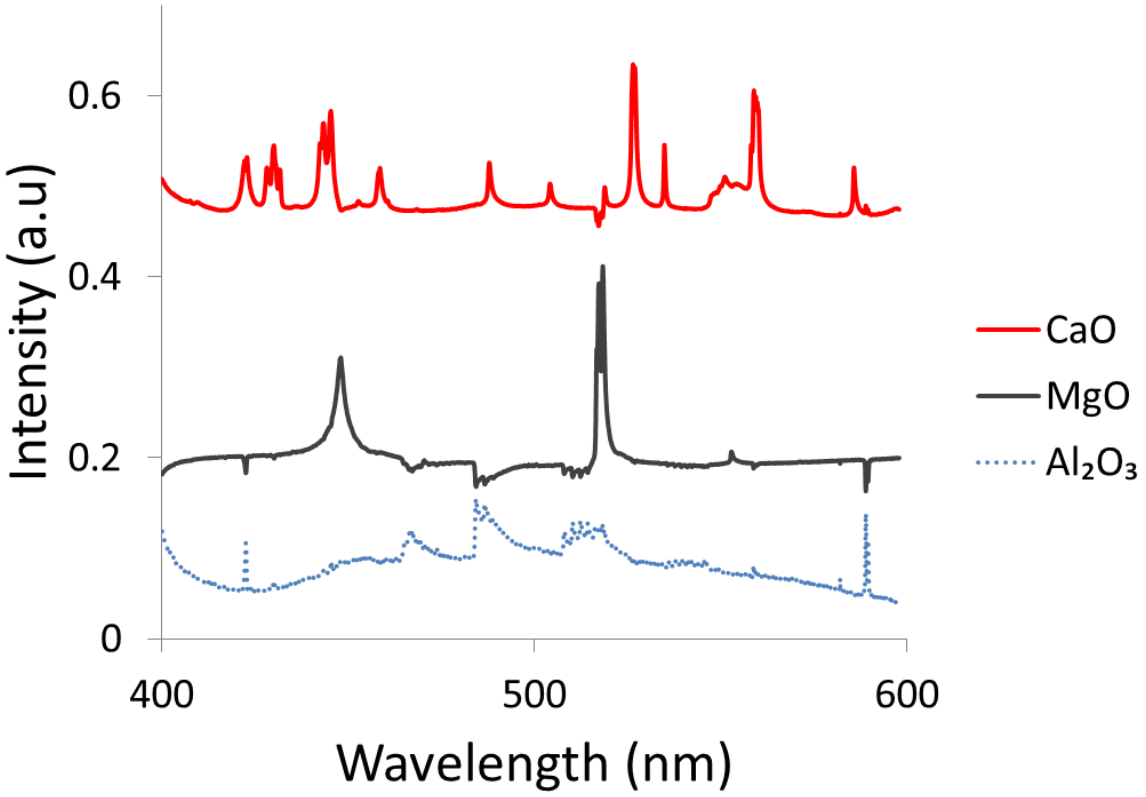


Figure 30: Renormalized modes for CaO, MgO, and $Al_2O_3$. Modes 2 and 3 renormalized at , Kim *et al.*

Table 4: Cross-correlation of final set of renormalized modes (Fig. 30) to reference spectra, Kim *et al.*

| | | Coefficient of Determination ($R^2$) | | | |
|---|---|---|---|---|---|
| Orthonormal Modes | | Reference Spectra | | | |
| | | CaO | MgO | $Al_2O_3$ | Sum |
| | Mode 1 | 0.979 | 0.021 | 0.001 | 1.001 |
| | Mode 2 | 0.000 | 0.944 | 0.056 | 1.000 |
| | Mode 3 | 0.007 | 0.012 | 0.980 | 0.999 |

Most of the intermixing between constituents is removed, thereby producing new modes that are better representative of the reference spectra individually. Furthermore, these modes retain orthonormal properties, which mean that they can be used directly to decompose a measured spectrum by cross-correlation.

4.4 Calibration

The applicability of the renormalized modes was tested using samples with known mixtures of CMAS constituents. Five different mole compositions of pure calcium oxide and magnesium oxide were thoroughly mixed and pressed into a disk using a kiloton press. Mole compositions included 0%, 25%, 50%, 75%, and 100% CaO by volume, with the remainder comprised of MgO. LIBS measurements were then taken on the disk samples. A total of 25 shots were taken for each sample, and its spectra were obtained. Before applying the POD modes to decompose the spectra, the reference spectra from Fig. 22 were first used directly to decompose the spectra using either a least-squares approximation or a sequential cross-correlation as discussed previously. These results are shown in Fig. 31(a) and (b), respectively.

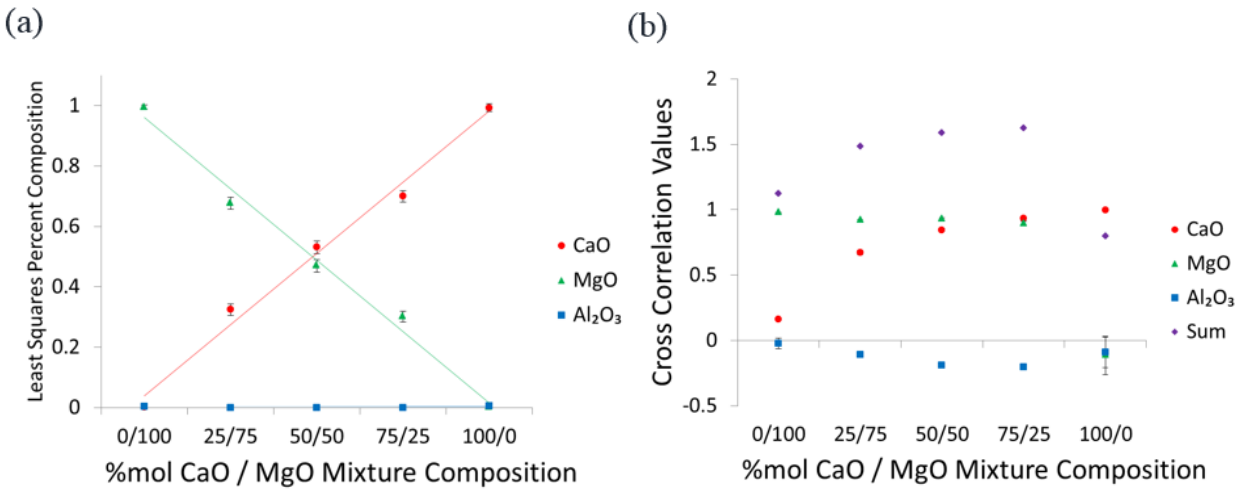


Figure 31: Calibrated measurements on CaO / MgO pressed disk samples using (a) least squares fitting and (b) sequential cross-correlation. The sum of the contributions does not equal unity, which indicates overestimation or underestimation, Kim *et al.*

For these calibration measurements, where only CaO and MgO are present and reference spectra for those constituent species are available, the least-squares approximation captures a linear relation, as shown in Fig. 31(a) and is a viable approach for quantifying the composition. A major drawback in the least-squares method even for this simple case is the heavier computational cost in comparison to POD. This iterative fitting impedes monitoring of CMAS speciation during LIBS in real time. Moreover, the least-squares approach does not work as well when additional species are present as shown subsequently. The

sequential cross-correlation method of decomposition, Fig. 31(b), suffers from overestimation of species and does not match the expected calibration values.

For POD, each spectrum was decomposed using the renormalized modes from Fig. 30. The constants from this decomposition (C in Eq. 1) represent the amplitude of that mode in the measured spectra and can be positive or negative. The square of the decomposition constants, $C^2$, represents the contribution of the mode to the signal variance and is taken as the relative contribution of that mode to the sample. Finally, it is necessary to calibrate the $C^2$ values against the pure samples to account for inherent differences in the LIBS signal strength between CaO and MgO. The average values for $C^2$ for each pure sample was used to scale the $C^2$ values for test samples. These normalized constants can then be taken as representative of the quantitative composition of the individual constituents.

The resulting calibrated measurements for the mixed samples are shown in Fig. 32. The data points indicate averages, and the standard deviation illustrates the range of values measured among 25 single shot LIBS measurements from a given mixture.

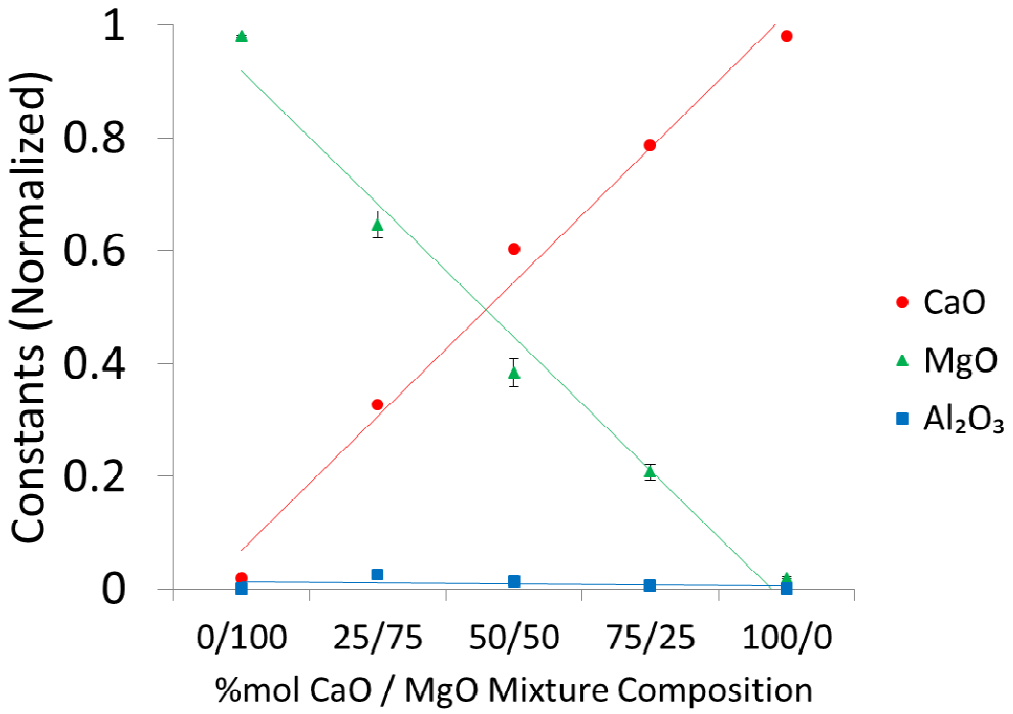


Figure 32: Calibrated measurements on CaO / MgO pressed disk samples using POD, Kim *et al.*

The standard deviation is largest in the mixed samples, which can be due to some non-uniformity of the relative mole compositions on the pressed disk surface during ablation. The uncertainty can also result from residual cross-talk indicated in Table 4.

An error analysis was done on the calibrated measurements. For each of the 25 single shot spectra, the absolute value of the difference between the experimentally measured composition and the known mole composition was computed. For the total sample size of 25 spectra per mixture, the maximum, minimum, and the average error were recorded for CaO, and MgO individually and are given in Table 5.

Table 5: Calibration error, Kim *et al.*

| | | CaO % Error | | | MgO % Error | | |
|---|---|---|---|---|---|---|---|
| | | Max | Min | Average | Max | Min | Average |
| %mol CaO/MgO | 0/100 | 5.18 | 5.15 | 5.17 | 5.16 | 3.45 | 4.26 |
| | 25/75 | 8.83 | 0.13 | 3.43 | 7.82 | 0.02 | 2.79 |
| | 50/50 | 11.6 | 1.70 | 6.37 | 10.6 | 0.79 | 5.49 |
| | 75/25 | 2.91 | 0.05 | 1.28 | 3.75 | 0.00 | 1.32 |
| | 100/0 | 5.56 | 4.79 | 5.19 | 6.09 | 5.32 | 5.71 |

The same procedure was used to calibrate alumina signals; however, for mixtures containing $Al_2O_3$, the relative signal and peak intensities were weak compared to the CaO and MgO signals, such that mole concentrations for alumina had a large error if the composition of CaO or MgO exceeded 25% (Fig. 33).

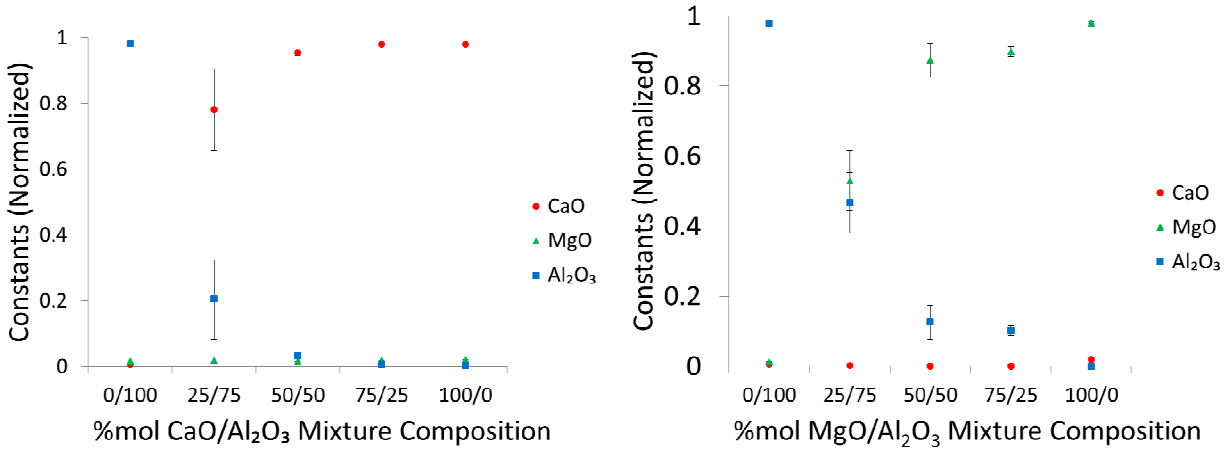


Figure 33: Calibration attempt on mixtures containing $Al_2O_3$.

As shown in the next section, the MgO and CaO LIBS signals are always dominant for the examined turbine blades even though measurable amounts of alumina are present.

4.5 Application on CMAS contaminated TBC

LIBS was finally performed on CMAS contaminated TBC coatings from engine-run turbine blades. The ablation target was traversed throughout the LIBS process to sample multiple locations across the blade. Decomposition using the renormalized modes from Fig. 30 was performed on the collected data. The calibrated composition for each spot on the blade is shown in Fig. 34 for measurements across two representative blades.

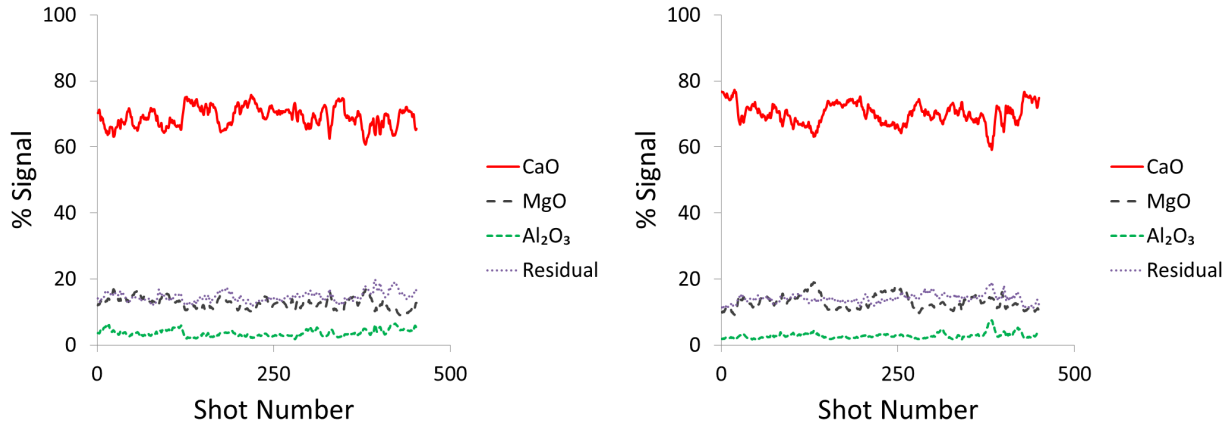


Figure 34: LIBS speciation on CMAS contaminated blades. Renormalized modes were used to extract the decomposition constants, which were normalized using calibrations for quantitative speciation (CaO and MgO only). Each shot represents a different location on the blade and the two plots are for separate turbine blades, Kim *et al.*

Note that since only three modes are used for this decomposition, a portion of the spectrum comprised of other species is unresolved. A method to quantify the unresolved species is discussed subsequently. In general, the composition of the CMAS shows only small variations across a single blade and is dominated by calcium which contributes approximately 80% to the total resolved CMAS LIBS signal. Magnesium is the second largest contributor at nearly 20% of the resolved signal. Some alumina signal is present but is at too small of a concentration to be accurately quantified given the dominant signals present from the other constituents.

In this analysis, only three of the constituents are considered: CaO, MgO, and $Al_2O_3$. Other missing constituents, such as $SiO_2$, and small contributions from other metallic oxides such as Ti, Fe, Ni, S are not taken into account. Moreover, noise in the LIBS measurement accounts for additional variance in the spectrum that is not captured by the renormalized modes. To quantify the contribution from missing constituents and spectral noise, a residual error analysis was performed on the results from Fig. 34.

Suppose that there are a total of *m* constituents present in a CMAS contamination. Then, expanding Eq. (1) yields:

$$S = C_1M_1 + C_2M_2 + C_3M_3 + C_4M_4 + C_5M_5 + \cdots + C_mM_m \tag{5a}$$

where each term corresponds to a constituent. The first three terms are CaO, MgO, and $Al_2O_3$, respectively, where the renormalized modes are provided. Then, by isolating the modes for the missing constituents:

$$S = C_1M_1 + C_2M_2 + C_3M_3 + (C_4M_4 + C_5M_5 + \cdots + C_mM_m) \tag{5b}$$

$$C_4M_4 + C_5M_5 + \cdots + C_mM_m = R \tag{5c}$$

where the isolated terms are defined as the residual, which is the spectrally unresolved information as a byproduct of a linearized approximation. An example of a single shot measurement, S, the representation of this measurement with the three renormalized modes, and the residual is shown in Fig. 35.

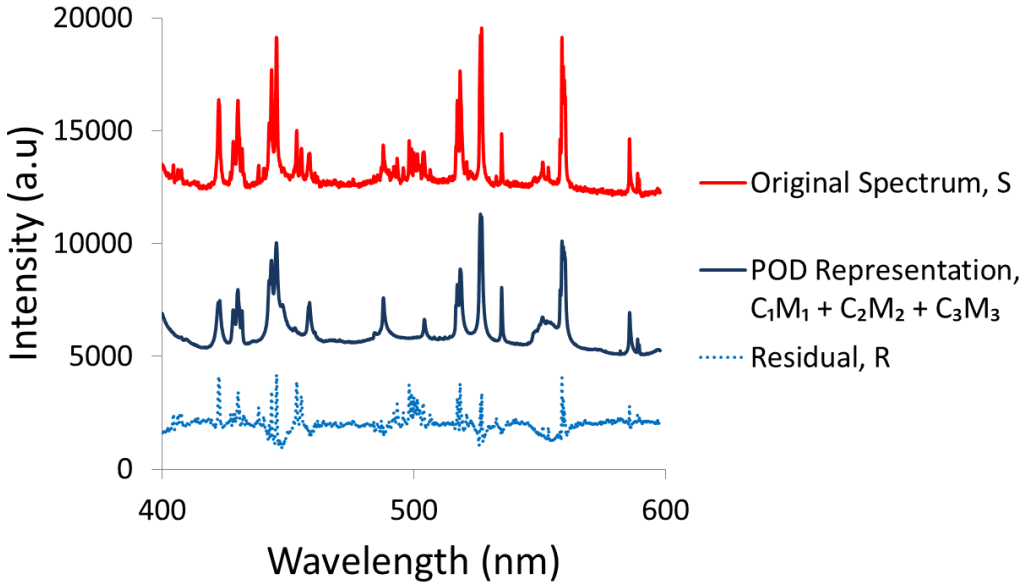


Figure 35: Separation of residuals from decomposed spectrum (POD), Kim *et al.*

Note that while this residual does have negative values as well due to noise, they are significantly smaller as compared to the contributions from the resolved species.

Taking the dot product of *S* from Eq. (5b) yields:

$$S \cdot S = C_1^2 + C_2^2 + C_3^2 + R^2 \tag{6}$$

since all of the modes are orthogonal. The collection of all of the POD constants for the missing constituents, as well as the noise, is the variance of the residual, where it defines the concentration of missing data. Then, to find signal percentages of each constituent, as well as the missing constituents:

$$\frac{C_1^2}{S \cdot S} + \frac{C_2^2}{S \cdot S} + \frac{C_3^2}{S \cdot S} + \frac{R^2}{S \cdot S} = 1 \tag{7}$$

where the first three terms are signal percentages of CaO, MgO, and $Al_2O_3$ modes respectively. The last term is the signal percentage of the residual, which represent the unaccounted constituents and signal noise. Eq. (5-7) demonstrate the importance of orthogonality for CMAS decomposition. If the constituent modes are not orthogonal, the residual in Eq. (7) can contain contributions from error in the fit to the resolved species. However with orthogonal modes the cross-correlation of the residual to the major

species spectra is identically zero. For the results in Fig. 34, approximately 14% of the total signal is in the residual representing omitted constituents, as well as unavoidable noise in the measurement. The other 86% of the signal is distributed among CaO, MgO and $Al_2O_3$ as quantified in Fig. 29; thus CaO contributes to approximately 70% of the signal, MgO to 13%, and $Al_2O_3$ to 3%.

To examine the contribution in the residual to $SiO_2$ or to the underlying TBC which may be partially ablated during LIBS, a cross-correlation between the residual and references for TBC and $SiO_2$ spectrum were computed. This is a valid approach because all of the spectral information regarding CaO, MgO, and $Al_2O_3$ was decomposed and separated from the residual. Thus, although the spectral references for TBC may not be orthogonal to the first three modes, the contributions from CaO, MgO, and $Al_2O_3$ references to the residual are approximately zero (which is not the case for least-squares and sequential cross-correlation method where non-orthogonal references were used for speciation). The cross-correlation values for TBC and $SiO_2$ references against the residual are shown in Table 6.

Table 6: Average cross-correlation values between the residuals and known reference spectra, Kim *et al.*

| Average cross-correlation values ($\bar{R}$) | | | | | |
|---|---|---|---|---|---|
| | Reference Spectrum | | | | |
| | CaO | MgO | $Al_2O_3$ | $SiO_2$ | TBC |
| Residuals | 0.000 | 0.000 | 0.000 | 0.018 | 0.046 |

Results show that TBC contributes approximately 4.6% of the total residual and $SiO_2$ contributes 1.8% of the residual signal. The remaining unidentified residual error indicates presence of other constituents that comprise CMAS, in addition to noise in the spectral measurements. Further investigation is necessary to verify the accuracy of the CMAS speciation when using pressed powdered samples as reference to calibrate measurements on CMAS contaminated coatings.

A similar procedure for error analysis was investigated for a least squares decomposition. In this case, the spectrum, S, is represented by a linear sum of the reference spectra for CaO,MgO and $Al_2O_3$ as,

$$S - error = a \cdot CaO + b \cdot MgO + c \cdot Al_2O_3 \quad (8)$$

where the coefficients a, b, and c signifying contribution of corresponding constituents are determined by a least-squares minimization of the residual. When applying this to the CMAS spectrum from Fig. 35, the least squares error is 22% of the total spectrum, compared to 14% from POD. This larger error leads to much larger variation in the CaO and MgO compositions across the blade as compared to the POD results shown in Fig. 34.

## 4.6 Summary

LIBS was performed on CaO, MgO, $Al_2O_3$, and $SiO_2$ samples to obtain spectra for each of the CMAS constituents. Disregarding the $SiO_2$ spectrum due to its weak signal, POD was completed on the other three references to construct a set of orthonormal modes. All three of the resulting modes were renormalized, two modes at a time, minimizing cross-talk. The set of new modes were used to decompose LIBS spectra for various known mixtures. Through calibration of data, CaO and MgO measurements were extracted. The relative weak intensities of $Al_2O_3$ mode were overwhelmed by the signal contributions from CaO and MgO, and could not be calibrated within reasonable accuracy despite significant presence in the CMAS samples. The renormalized modes were used to analyze CMAS contaminated TBC coatings from engine-run turbine blades. Results showed that the spectra obtained from the ablated region primarily consisted of CaO, contributing to more than 70% of the signal, MgO at approximately 13%, and $Al_2O_3$ at 3%. The residuals which included slight amounts of TBC and $SiO_2$, other missing constituents, as well as noise in the collected spectrum accounted for approximately 14% of the total signal. Calibration experiments show that the MgO and CaO content can be determined typically with an accuracy of 6%. Least squares approximation and sequential cross-correlation was also investigated on the set of data. Results showed that although least squares captured a linear relation for calibration experiments where all present species were included in the reference data set, POD surpassed least squares in computational efficiency as well as for decomposition of the CMAS measurements on a contaminated blade with additional unknown species. Sequential cross-correlation suffered from severe overestimations and underestimations of contributions from each constituent, and did not yield reasonable

calibration. The accuracy of calibration using spectra collected through pressed powder samples to CMAS deposits on the coatings will be examined in future work. Finally, it is worth noting that previous results (Majewski, 2011) showed that with the chosen laser intensity, CMAS was removed at a relatively constant rate of 1 μm/shot. By combining the analysis in this chapter with the ability to discern the CMAS/TBC boundary (Majewski, 2011) this technique can give CMAS composition and a good estimate of CMAS thickness.

**5. Time Gated Photoluminescence Piezospectroscopy (PLPS)**

As discussed in Chapter 4, a reliable method for CMAS removal on engine-run blades without coating damage has been demonstrated using LIBS spectrum cross-correlation (Majewski, 2011) and further improved by using POD modes instead of reference spectra (Hawron, 2014). CMAS cleaning of the coating surface has been proven to be effective as it allows routine PLPS measurements on engine-run blades to evaluate remaining coating lifetime (Majewski, 2012). However, a new possible source of PLPS obstruction has been discovered recently when applying PLPS to new coatings. This obstruction is not due to an outer film of CMAS but occurs within the coating composition itself. In the case of performing PLPS on CMAS contaminated blades, the source of photoexcitation is intercepted by the alumina in CMAS that causes non-TGO chromium fluorescence to be collected. On the other hand, coating-based interference need not necessarily involve alumina; any type of irregular dopants that fluoresce near chromium wavelengths may interrupt PLPS measurements. Such was the case for a particular vane sample as shown in Fig. 36.

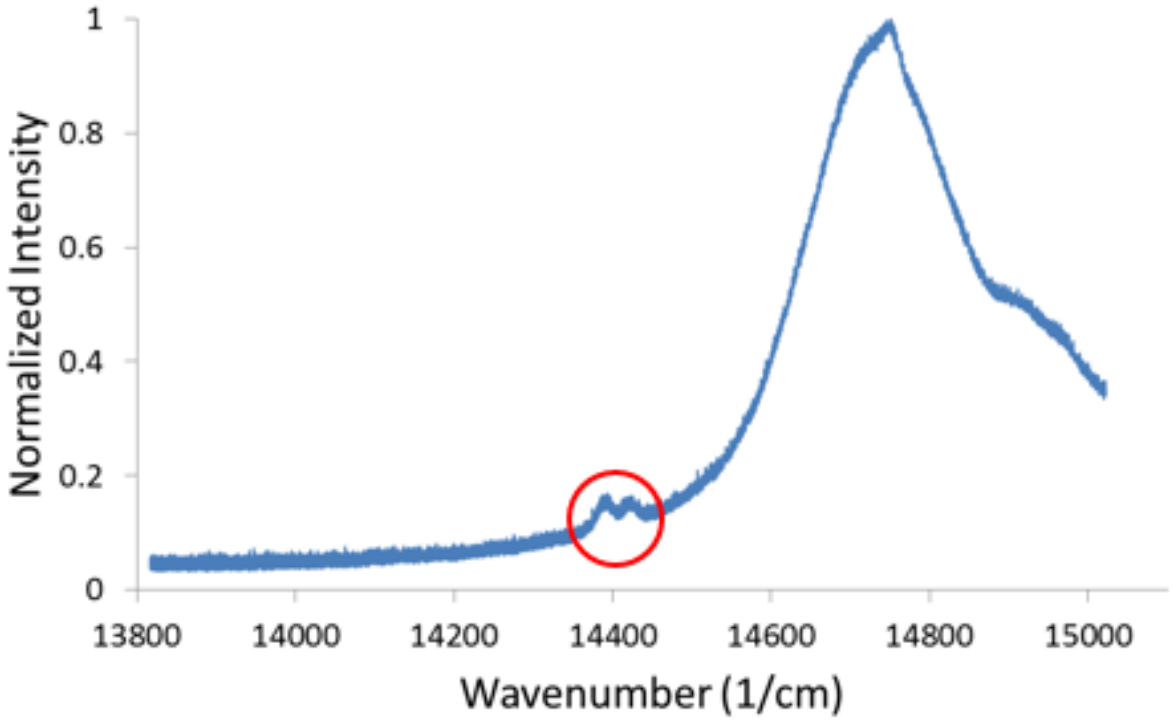


Figure 36: Fluorescence interference. Desired chromium fluorescence circled in red. Integration time = 3 seconds.

The excessive fluorescence interference centered at 678 nm originated from a non-standard impurity within the YSZ topcoat. The tail end of this expansive fluorescence peak at 694 nm overshadowed the chromium fluorescence which invalidated deconvolution of the R1-R2 doublet necessary to obtain stress measurements. The overwhelming intensity of the interference disallowed reasonable curve fitting as this trailing signal distorted the baseline of the chromium fluorescence.

Unlike CMAS interference which can be cleaned via LIBS (Majewski, 2011), the irregular dopant within the coating could not be physically separated without damaging the coating itself. Regarding the sample in Fig. 36, the standard YSZ may have been modified for coating improvement such that the interference was an intentional addition to the coating. With continual investigation and concoction of new coating compositions for improved performance, similarly unexpected PLPS interferences may occur depending on the application. In this chapter, the difficulties of filtering the unwanted fluorescence is demonstrated and to cope with such complication, the combined chromium and coating fluorescence is temporally filtered prior to spectrally resolving the R1-R2 doublets. This combination of temporal and spectral filtering is demonstrated to permit valid PLPS stress measurements

The described temporal filtering as an add-on to the routine PLPS is referred to herein as time gated PLPS and uses a pulsed laser for reasons that time-dependent measurements cannot be taken with a continuous laser. Time gated PLPS requires a pre-experimental verification—a confirmation test regarding the viability of temporal filtration of the interference. In the confirmation test, a pulsed laser is employed to induce a short-lived fluorescence decay of suspected constituent samples in question, and the signal intensities are examined as a function of time. Based on the results, the time scale of the interference can be compared to the time scale of fluorescence from chromium so that the applicability of temporal resolution can be verified, and furthermore, appropriate time parameters for the time-based filtration can be established. After successful confirmation, time resolved PLPS measurements were taken on the vane sample from Fig. 36; the observed fluorescence was gated such that measurements were recorded within the time window specified by the time parameters previously obtained in the

confirmation test. Lastly, a bandpass filter with a cutoff at <685 nm (>14800 $cm^{-1}$) was installed within the wavelength division multiplexor (WDM) for additional filtration of the problematic interference.

The results of time gated PLPS are first shown using a lower spectral resolution diffraction grating with high diffraction efficiency to demonstrate effectiveness. In these results, the R1-R2 doublet is merged into a single peak at the benefit of good signal intensity. A higher spectral resolution grating with lower diffraction efficiency was later installed to realize the distinctive R1 and R2 peaks at the cost of having noisier signals due to lower grating efficiency. Although the quality of R1-R2 resolution (expressed as merit value in the deconvolution) is dependent on signal-to-noise ratio as investigated in a previous study (Hawron, 2014), the R1-R2 deconvolutions are graphically confirmed for questionable merit values for validation. The merit value is a measure of credibility for the corresponding stress measurement, and ranges from 0 (no fit) to 1 (perfect fit). In Hawron's (2014) experiments, the acceptable merit values were set at 0.975 or higher; in the results to be discussed in this chapter, merit values of 0.8 or higher were accepted. Although these low merit values were previously considered invalid, it was found that the lower signal levels result in lower merit values for fits that are still good representations of the R1-R2 measurements. The limitations in grating efficiency caused lower signal-to-noise ratio in the collected data which was partially compensated for through longer integration times. The merit values in this work ranged from 0.8 to 0.95; stress values with merit values near the low 0.8 were visually checked for credibility in the determined fit. Results showed that despite the low merit values, the deconvolution of the R1-R2 doublets were sound, and provided acceptable estimations in measured local stresses.

## 5.1 Fluorescence Interference

Figure 37 shows the results of deconvolution on alumina packed powder fluorescence without the presence of interference. With a merit value of near maximum at 0.997 indicative of an exceptional curve fit, the location of the following R2 line is recorded as the zero stress reference. The merit value is similar in meaning to that of a cross-correlation coefficient—it is a measure of the curve fit quality which ranges from 0 (no fit) to 1 (perfect fit) and is given by

$$\overline{\qquad\qquad}$$

where is the intensity of the spectrum at pixel, is the intensity of the fitted curve at pixel, and the overbar indicates mean value (Selcuk, 2002). The merit value is often influenced by fluorescence signal quality and monotony of the collected R1-R2 doublet frequency shift. Merit values have been observed to suffer from low signal-to-noise ratios as well as broadened R1-R2 doublet due to extreme readings near local microcracks in the coating as well as uncleaned CMAS islands (Hawron, 2014). The broadened peaks can be decomposed into a set of R1-R2 doublets using a bimodal as opposed to a unimodal deconvolution (Wen, 2006).

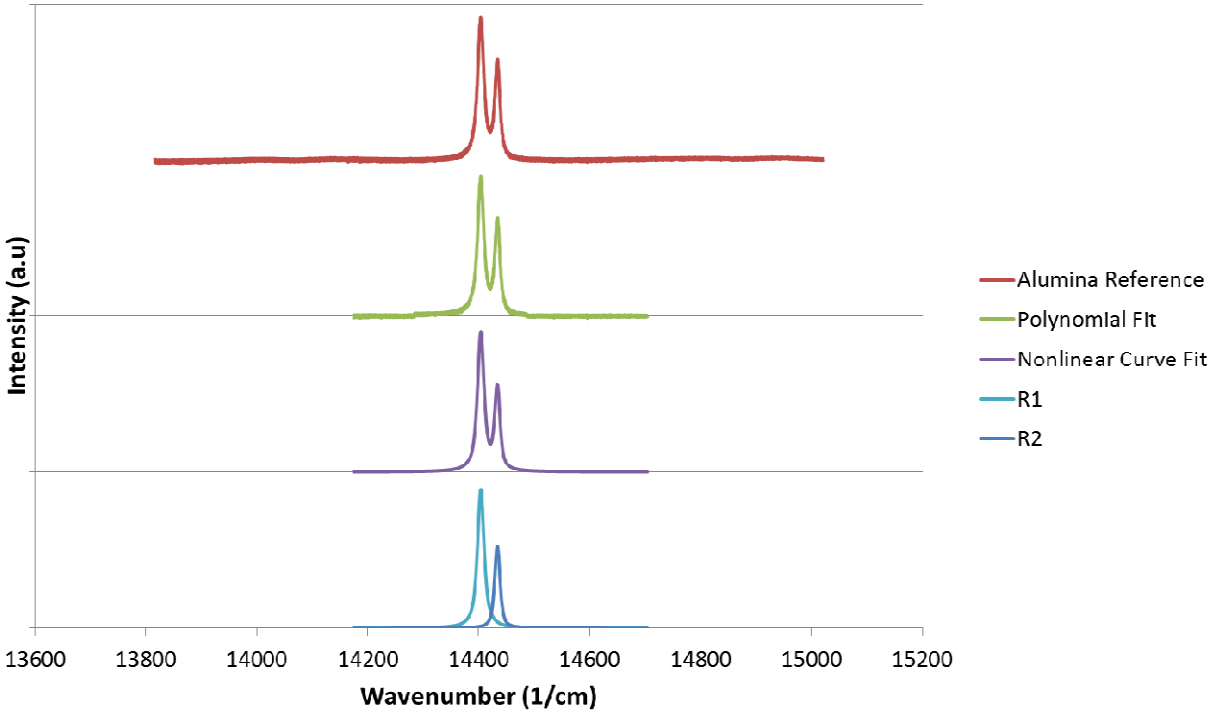


Figure 37: Alumina reference unimodal deconvolution. Merit value = 0.997. Integration time = 0.3 seconds.

Figure 38 shows the erroneous results of a deconvolution attempt on the fluorescence from Fig. 36. Bimodal deconvolution is used to obtain two stress readings of 3.665 GPa (R2A) and 1.589 GPa (R2B); however, due to unacceptably low merit values, these stress values are not credible.

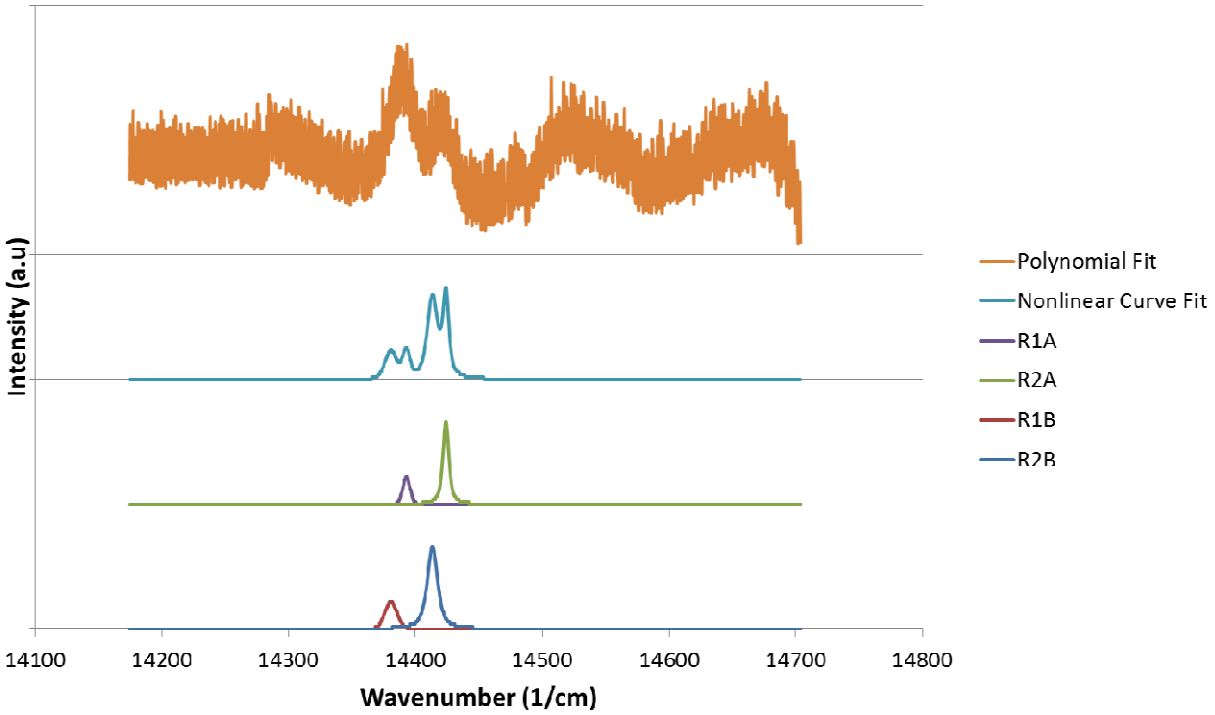


Figure 38: Deconvolution attempt on the PLPS spectrum shown in Fig. 36. Measured stresses = 3.665 GPa (R2A) and 1.589 GPa (R2B) with corresponding merit values = 0.011 (R2A) and 0.026 (R2B).

The insurmountable noise levels seen in the polynomial fit from Fig. 38 are a direct result of the immense volume of the fluorescence interference. The baseline of this fit is harshly uneven as evidence of a poorly fitted data. Furthermore, the severely variant stress measurements of 3.665 and 1.589 GPA is improbable for relatively well-defined chromium peak in Fig. 36; these peaks do not seem as broad as in the deconvolution shown in Fig. 38. It is highly likely that these stress measurements are invalid. The difficulty in evaluation of a spectrally unresolvable fluorescence necessitated temporal filtering to significantly improve stress analysis.

## 5.2 Time Gating

Time gating, or obtaining a time resolved spectrum, is enabled by exploiting dissimilar time dependencies of signals of the individual sources; for this application, the objective was to determine a time window in which the chromium-to-interference fluorescence signal ratio is maximized.

Consider a hypothetical scenario where two simultaneously occurring signals are characterized by a different order of exponential decay as shown in Fig. 39.

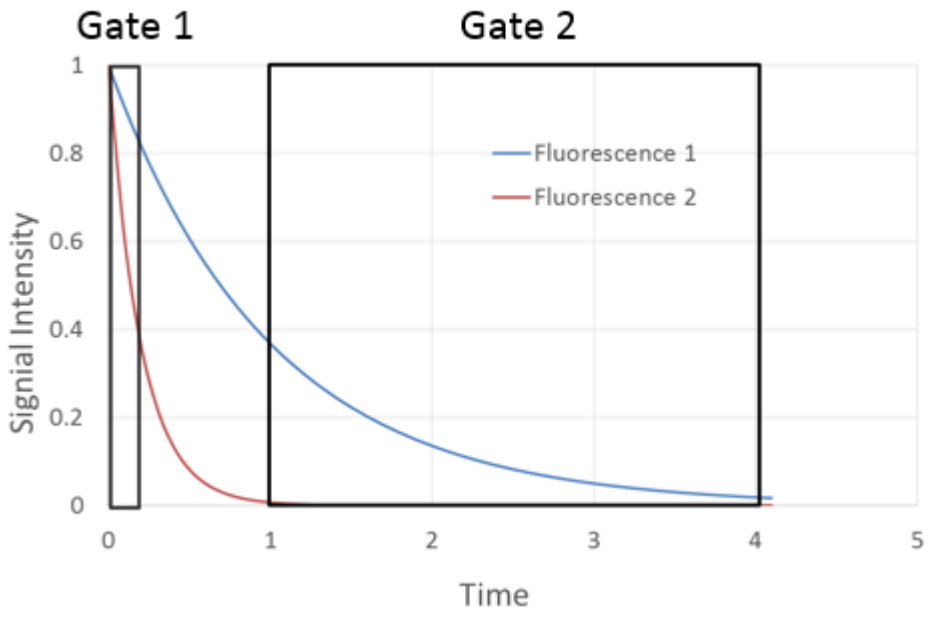


Figure 39: Time gating options for a pair of two hypothetically dissimilar fluorescence decays. Two possible time windows are preferred depending on fluorescence of interest—Gate 1 to maximize fluorescence 1-to-2 ratio, and Gate 2 for vice-versa. After identification of workable gating parameters, measurements can then be taken to temporally resolve the received PLPS spectrum.

To implement the described time gate on the fluorescence shown in Fig. 39, the dissimilar signal decay rates must first be confirmed. In this confirmation experiment, a pulsed laser was employed to realize the observable fluorescence decay; fiber cables were used to guide the fluorescence into a photomultiplier tube (PMT) coupled to an oscilloscope (Fig. 17) to observe signal intensities in terms of voltage as a function of time. The experiment was conducted on two samples: an alumina reference and the source of the coating impurity, which was separately identified. Condoning the voltage oscillations due to instrumental noise, results showed that the chromium fluorescence persisted longer than the interference, as shown in Fig. 40. Therefore, a delayed time window (Gate 2) was desirable in temporally resolving the mixed fluorescence in favor of chromium.

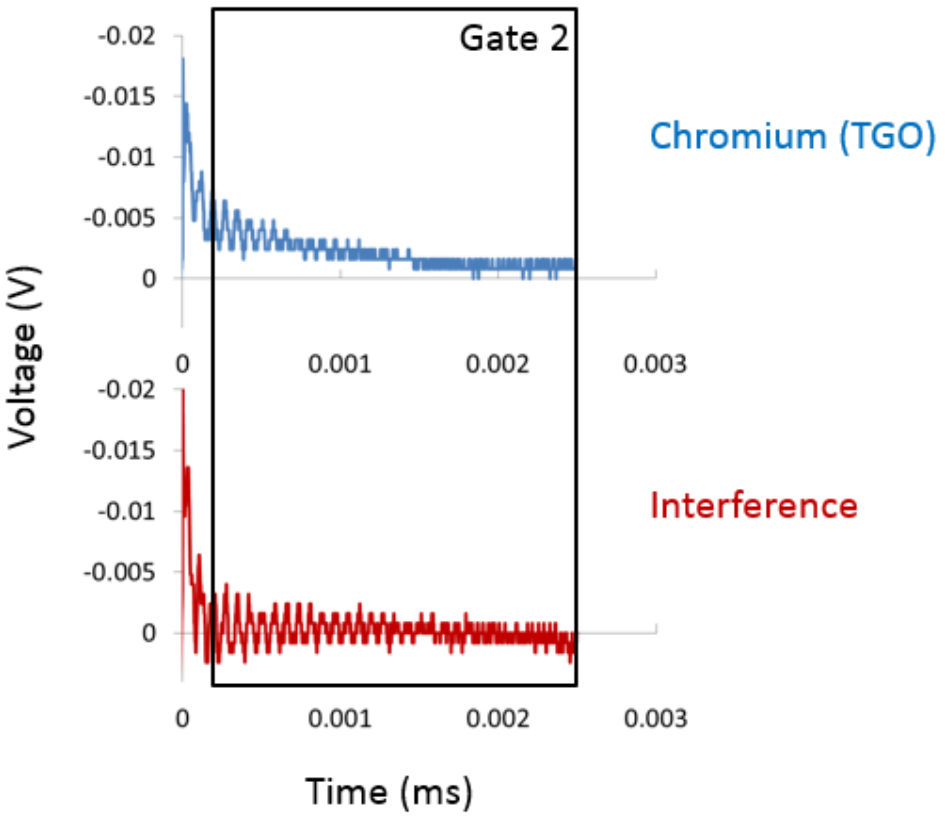


Figure 40: Confirmation of fluorescence decay disparity. Lasing occurs at time = 0 ms. A delayed time gate is desirable for the persistent chromium fluorescence.

During time gated PLPS, fluorescence collection only occurs when the image intensifier is actuated through the delay generator (Fig. 20). The delay generator is the main catalyst of the time gated PLPS setup and has multiple purposes—it dictates the initiation and duration of the time gate to be administered, and accounts for any instrumental delays for synchronized digital communication. The results from Fig. 40 offered approximate time windows to resolve the incoming fluorescence, and then was fine-tuned through trial and error:

$$A_i = T_i + 0.10015\ seconds$$

$$B_i = A_i + 0.09\ seconds$$

where, for the $i^{th}$ pulse:

$$T_i = Nd{:}YAG\ Q - switch\ output$$

$$A_i = gate\ intiation$$

$$B_i = gate\ termination$$

for a pulse repetition rate of 10 Hz. The time resolved spectral collection is graphically illustrated in Fig. 41.

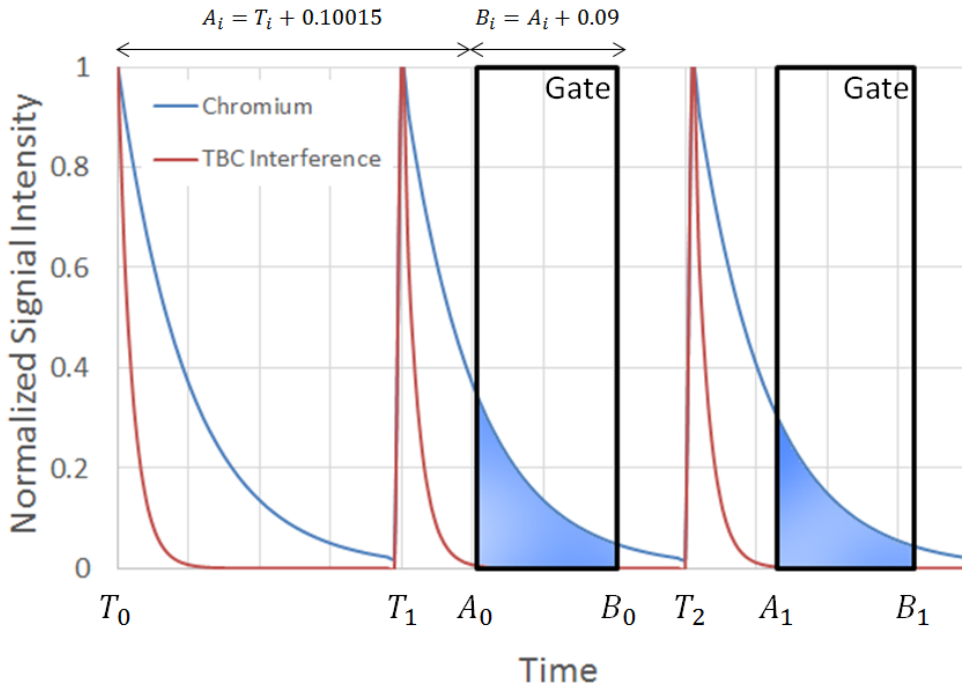


Figure 41: Time gating parameterization. The spectral collection (blue-filled area under curve) is staggered by a full pulse to account for inevitable instrumental delay. Axes are not to scale.

Note that actuation of the time gate is staggered by a full pulse to account for all possible digital communication delay. These parameters were used to collect all of the time resolved data shown in the subsequent sections.

## 5.3 Time Resolved PLPS Spectra

In the first trial of experiments, the PLPS spectra were collected with the Spectra-Physics spectrometer equipped with a custom designed dual grating with a low spectral resolution of 0.5 nm; the R1-R2 doublets were merged into a single peak in both of the alumina reference and vane PLPS spectrum, shown in Fig. 42. The diffraction grating of a spectrometer is responsible for spatial separation of incoming light into discrete wavelengths. The spectral resolution of a grating is a measure of light dispersion and does come without trade-offs—a finer grating, as a result of greater dispersion, typically has a lesser wavelength range and diffraction efficiency (defined as the ratio of the diffracted light to the

illuminating light), and vice-versa for a coarser grating. The diffracted light observed through a camera must be calibrated into corresponding wavenumbers for stress measurements.

However in the first trial of experiments, the pixelated PLPS spectra as observed on the camera could not be indexed to corresponding wavenumbers due to insufficient spectral resolution of the diffraction grating. Nevertheless, a qualitative study was done to determine the effectiveness of time gating using the high efficiency / low resolution grating. A finer grating was later installed after a series of validation experiments followed by calibration (pixels to wavenumbers) in the final experimental setup for stress measurements.

The vane sample PLPS spectrum shown in Fig. 42 is time resolved to provide a resolved spectrum shown in Fig. 43.

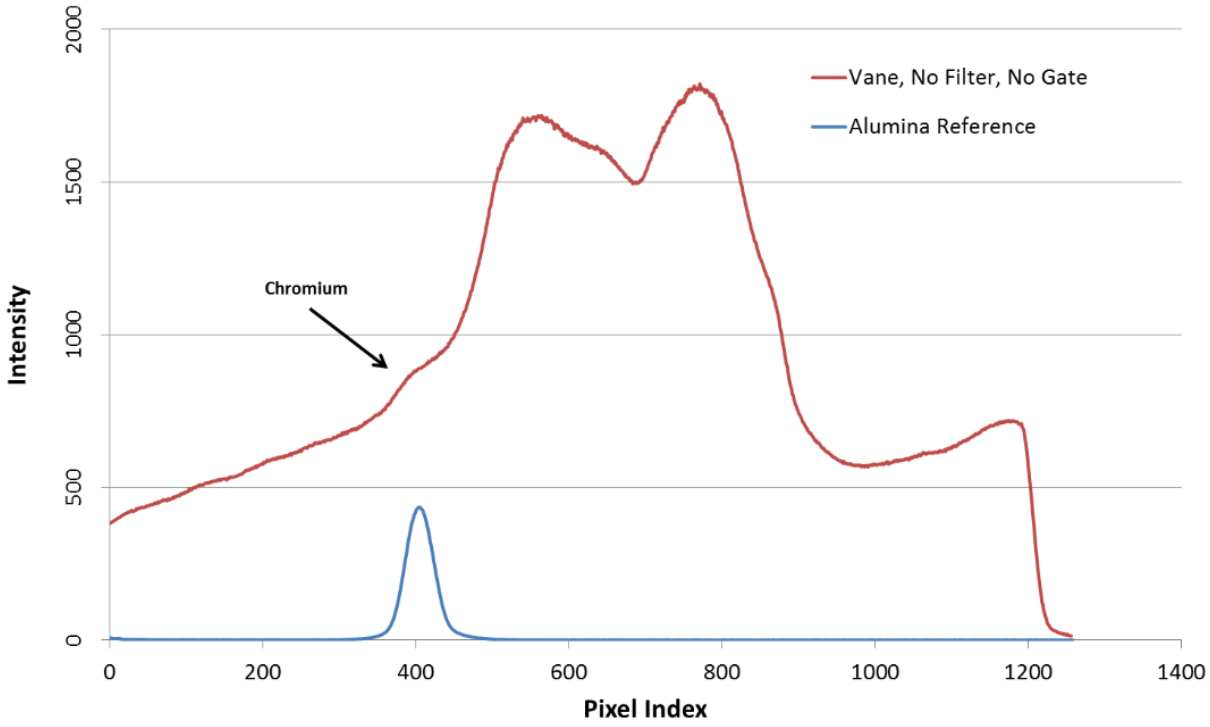


Figure 42: Original fluorescence. Integration time = 8 seconds.

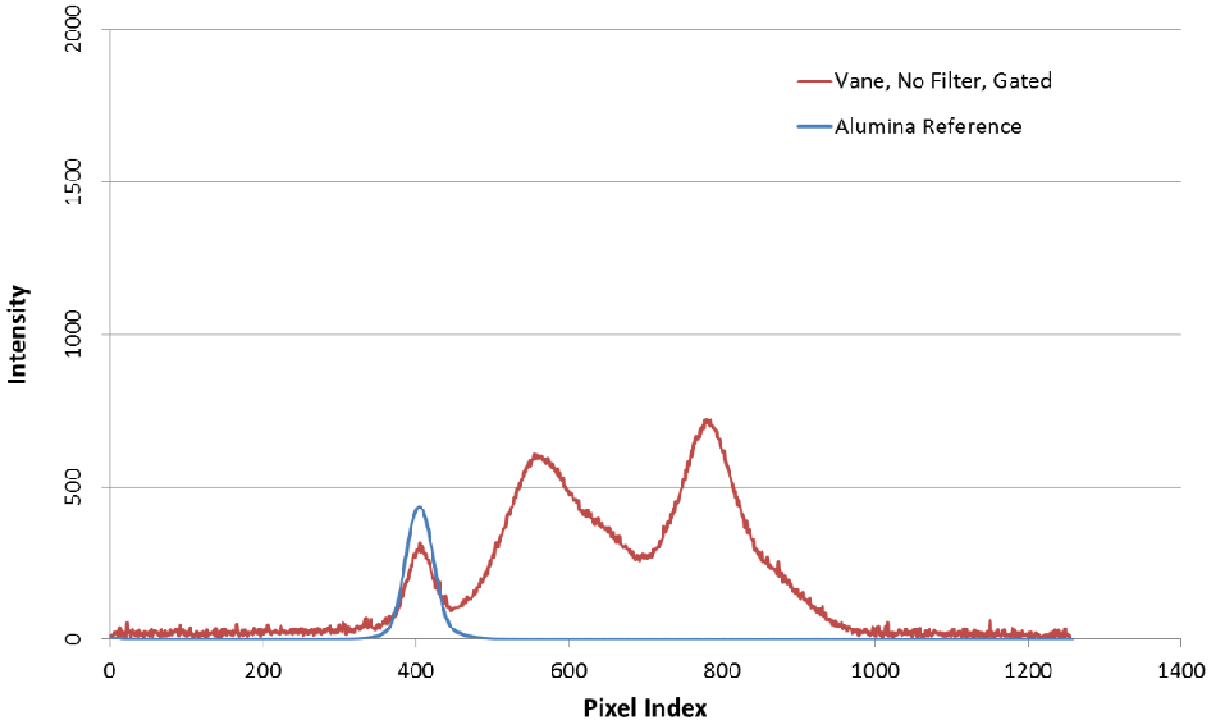


Figure 43: Time gated fluorescence. Integration time = 8 seconds.

The coating interference was significantly diminished in the time resolved spectrum in Fig. 43 but the interference intensities still exceeded the chromium fluorescence of interest.

For further improvement, a bandpass filter with a specified cutoff at <685 nm (>14800 $cm^{-1}$) is installed within the wavelength division multiplexor (WDM), and the direct effects can be seen in Figs. 44-45.

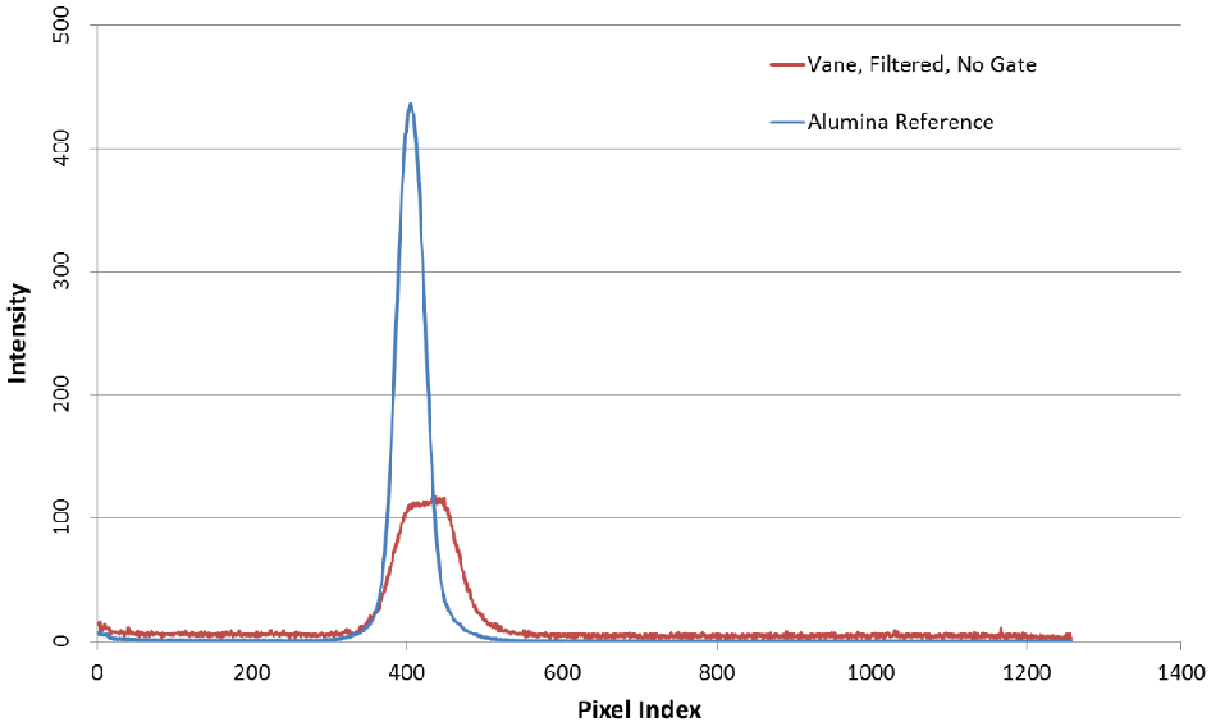


Figure 44: Original fluorescence with the bandpass filter. Integration time = 8 seconds.

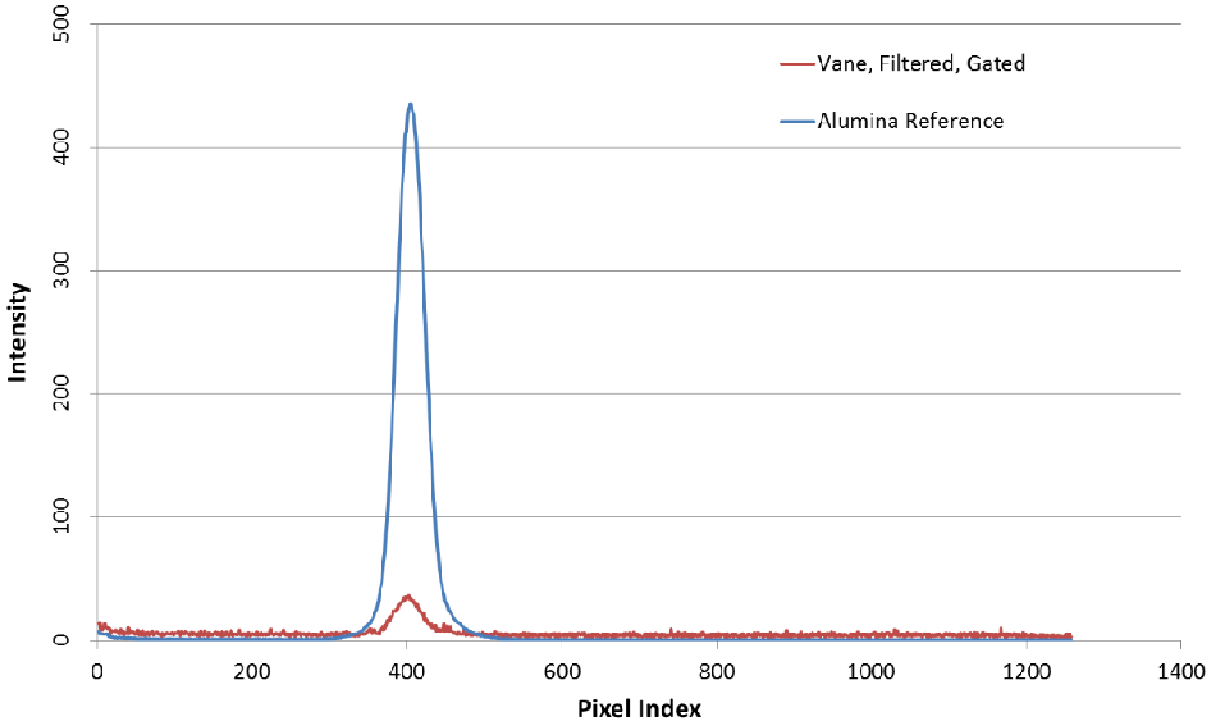


Figure 45: Time gated fluorescence with the bandpass filter. Integration time = 8 seconds.

The finalized time resolved PLPS spectrum supplemented with a bandpass filter showed significant improvements. The time resolved fluorescence near alumina reference verified its chromium identity. The volume of interference eliminated from Fig. 42 to Fig. 45 demonstrated the effectiveness of time gated PLPS to extract the buried chromium fluorescence. The low resolution grating was replaced by a high resolution grating in the next experiment to separate the R1-R2 doublet necessary for stress measurements.

## 5.4 Stress Measurements using Time Gated PLPS Spectra

In the second trial of experiments, a Spectra-Physics 74161 dual grating with a higher spectral resolution of 0.17 nm was installed which allowed visualization of the R1-R2 doublets for stress measurements. An unstressed alumina sample was re-measured using this new grating; the collected spectrum was calibrated to corresponding wavenumbers and was adopted as the zero stress reference, shown in Fig. 46. This calibration was enabled by the finer spectral resolution that allowed visualization of discrete R1 and R2 peaks. These calibration settings were used for all of the results to be shown in subsequent figures.

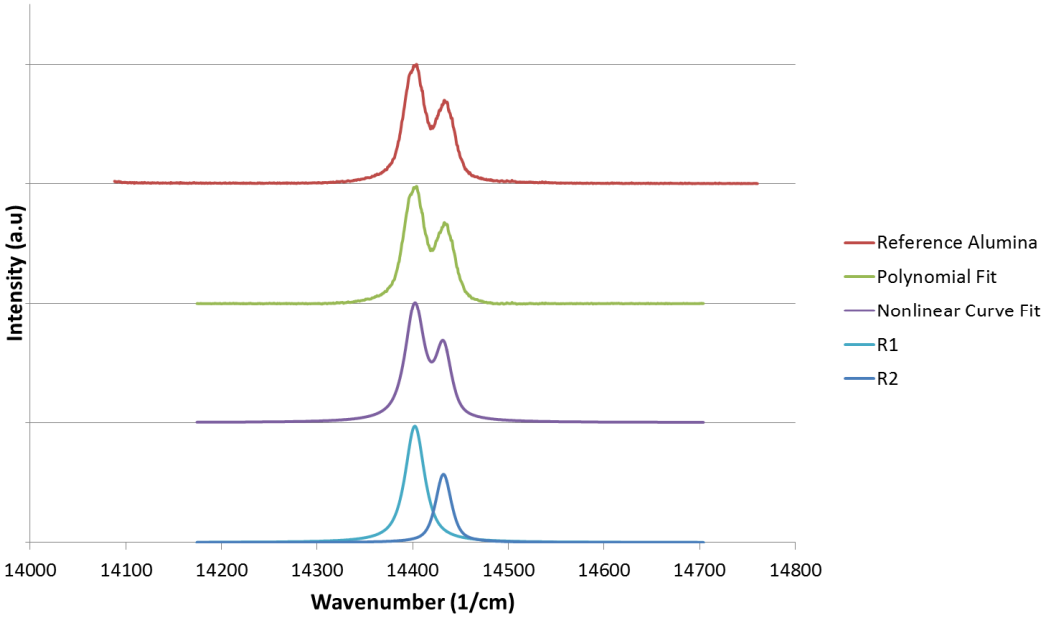


Figure 46: Deconvolution on wavenumber-calibrated reference alumina fluorescence on Spectra-Physics spectrometer equipped with high resolution grating. Merit value = 0.987. Integration time = 3 seconds.

An unfiltered, non-resolved PLPS spectrum was collected on the non-standard TBC vane shown in Fig. 47.

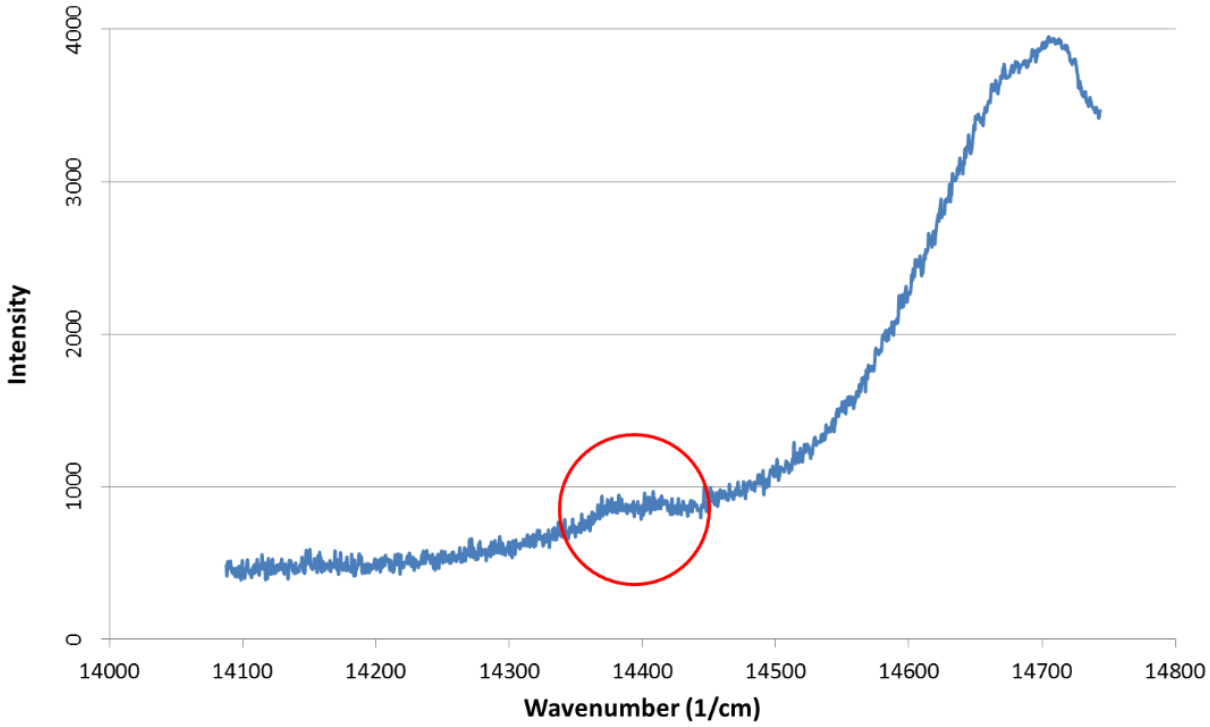


Figure 47: PLPS spectrum using finer grating. Desired chromium fluorescence circled in red. Integration time = 15 seconds.

The previously employed time gating parameters (Fig. 41) were reused with this finer grating with the bandpass filter in place, obtaining a finalized time resolved spectrum which was curve fitted for deconvolution as shown in Fig. 48.

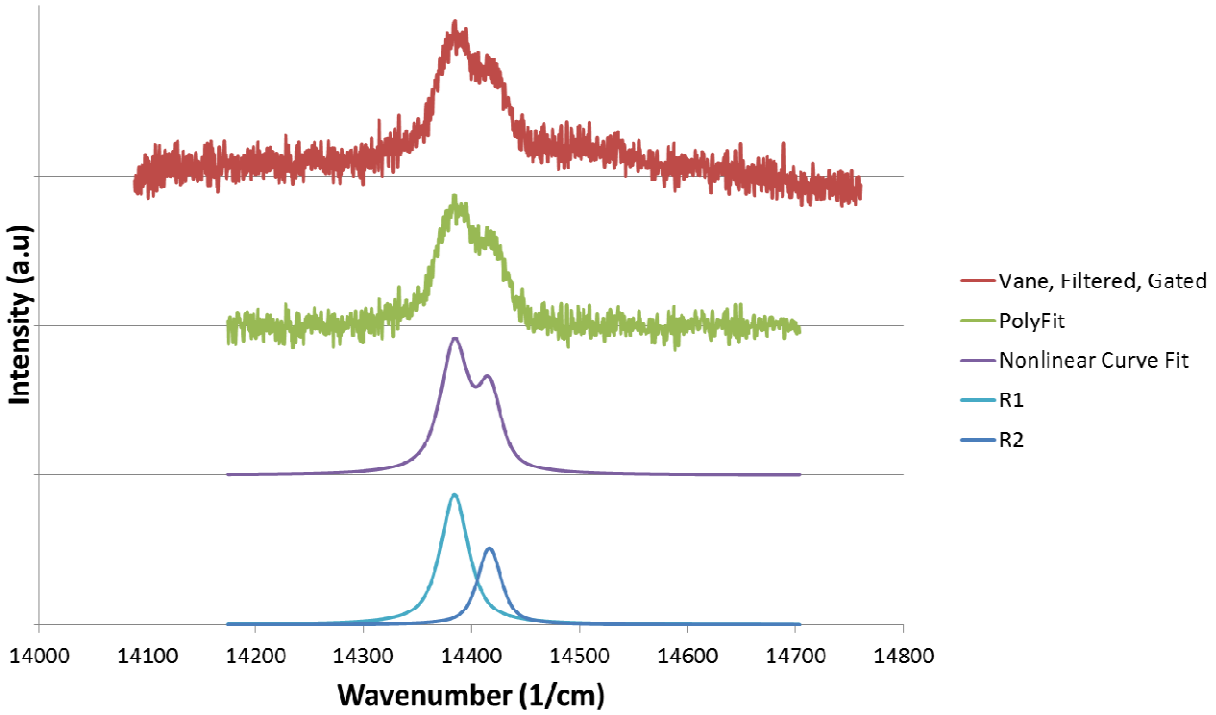


Figure 48: Deconvolution of a time gated PLPS spectrum with bandpass filter. Merit value = 0.929, slightly lower due to noise. Integration time = 200 seconds.

The subtlety of the chromium fluorescence, as well as a degrade in diffraction efficiency necessitated an integration time of over 3 minutes to obtain the spectrum shown in Fig. 48. A stress measurement of 3.06 GPa was obtained for the spectrum shown in Fig. 48 with a merit value of 0.929. Despite a slightly lower merit value, the curve fits appear to be satisfactorily aligned with the time resolved spectrum. The R1-R2 doublets are adequately well-defined such that a unimodal deconvolution suffices with a physically reasonable stress value of 3.06 GPa indicative of mild coating fatigue.

Additional stress measurements were taken within the vicinity of the interrogated location shown in Fig. 48, and results showed average stress values of 3.056 GPa, a maximum and minimum value of 3.2131 and 2.765 respectively, with a standard deviation of 0.113 (Fig. 49). The corresponding merit values were averaged at approximately 0.909, a maximum and minimum value of 0.953 and 0.787 respectively, with a standard deviation of 0.030 (Fig. 49).

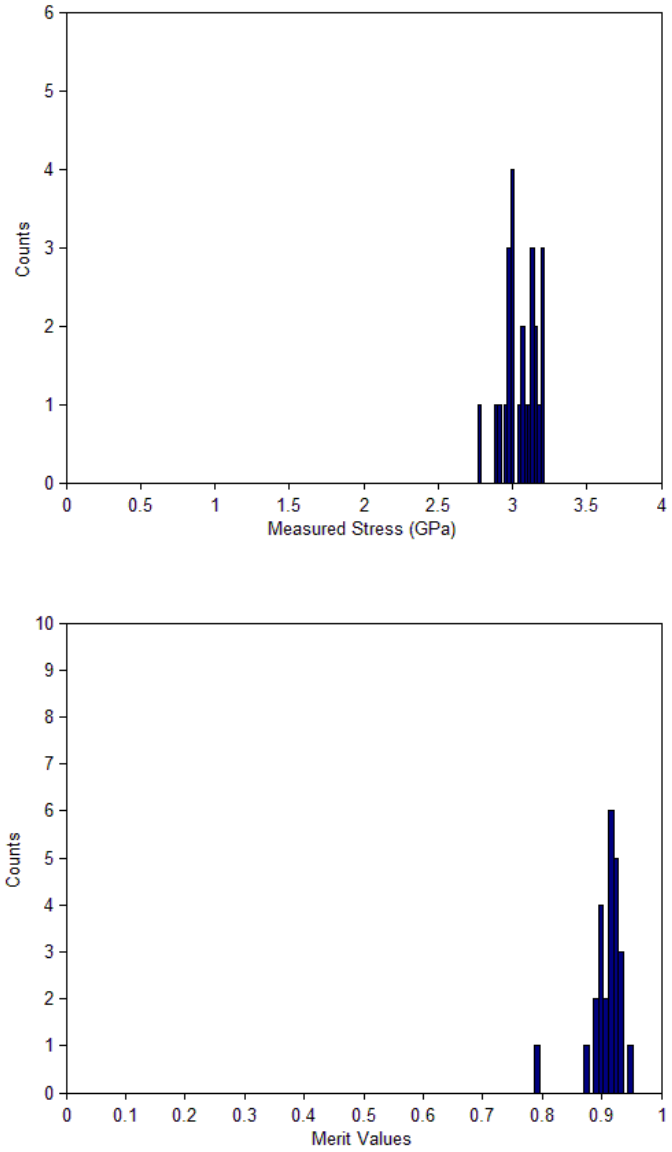


Figure 49: Histograms of stress measurements and merit values for the collected time resolved fluorescence data set near the head of the blade. Average stress of 3.056 GPa with a standard deviation of 0.113, and average merit value of 0.909 with a standard deviation of 0.030 were recorded.

These values were taken near the head of the pressure side; upon wider scope of investigation, results showed that stress values near the extensible tail of the blade were significantly lower than the previously averaged 3.056 GPa. Stress measurements near the extensible tail yielded an average value of 2.481 GPa, a maximum and minimum value of 2.623 GPa and 2.345 GPa respectively, with a standard deviation of 0.074. The corresponding merit values were averaged at 0.885, a maximum and minimum value of approximately 0.937 and 0.801 respectively, with a standard deviation of 0.038 (Fig. 50).

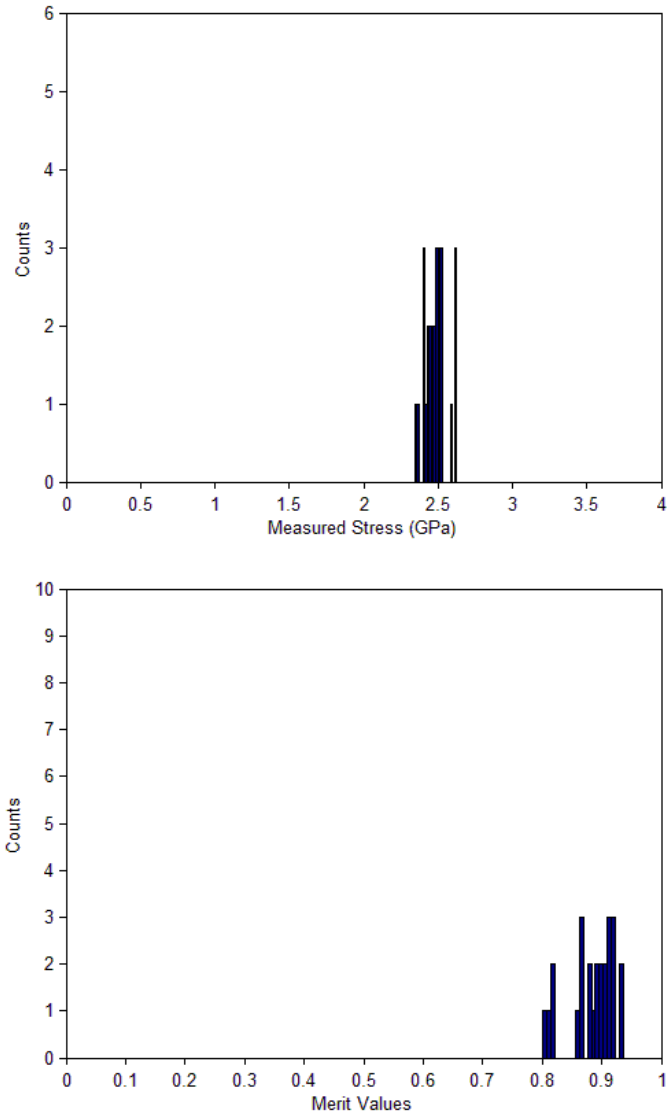


Figure 50: Histograms of stress measurements and merit values for the collected time resolved fluorescence data set near the tail of the blade. Average stress of 2.481 GPa with a standard deviation of 0.074, and average merit value of 0.885 with a standard deviation of 0.038 were recorded.

The lower merit values were a result of weaker fluorescence intensity, thus lower signal-to-noise ratio; deconvolution of PLPS spectra that resulted in the highest and lowest merit values are shown in Fig. 51 for comparison of signal quality. The lower signal-to-noise ratio has influenced the polynomial fit as well.

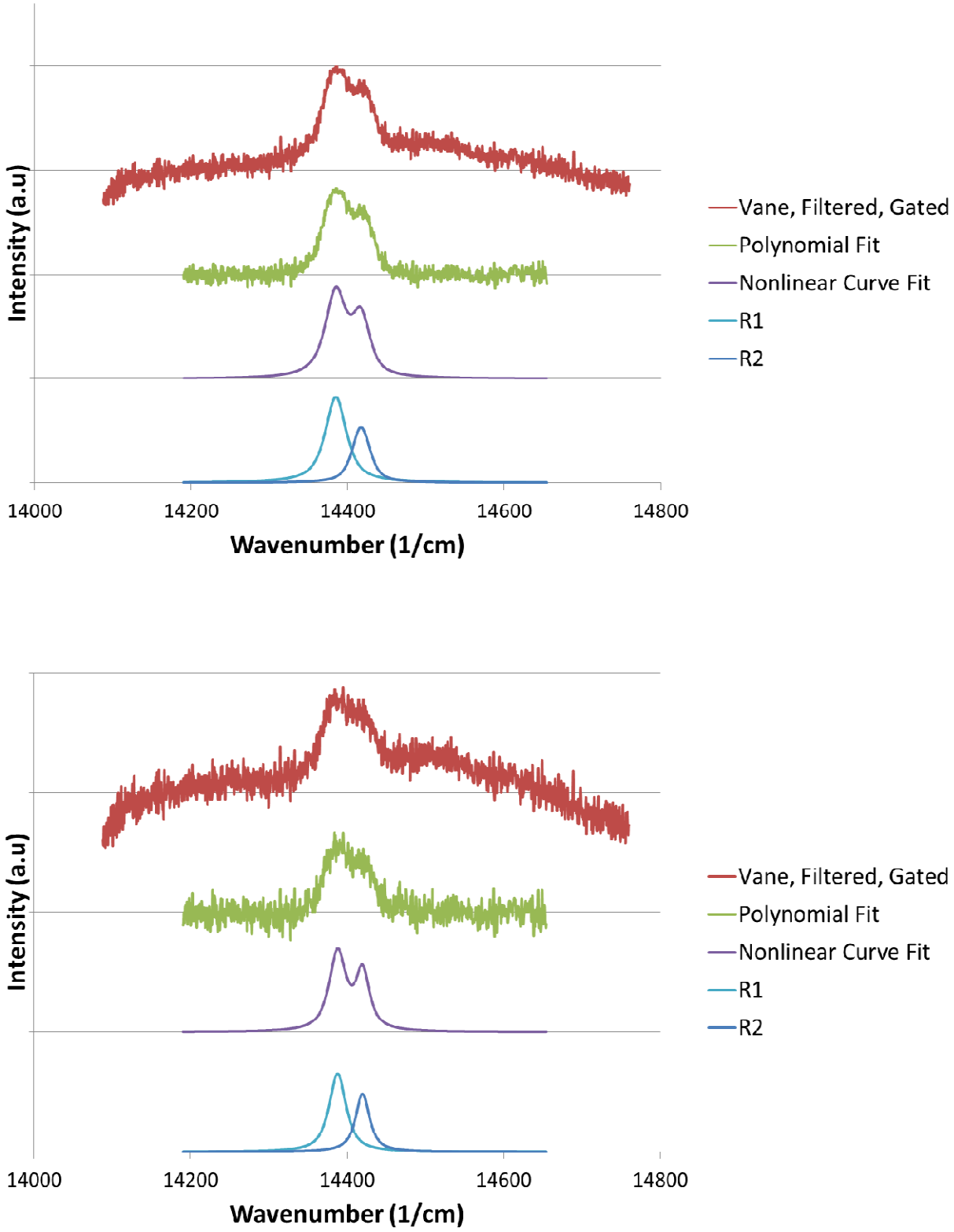


Figure 51: Demonstrating the signal-to-noise ratio and the corresponding polynomial fit for a calculated merit value of 0.953 (top) and 0.787 (bottom). Integration time = 200 seconds.

The lower stress values near the tail end indicate that the vane sample evaluated in this study underwent accelerated thermal fatigue at this location. This may be a result of the specific design of the cooling mechanism for this particular sample; further investigation may enable identification of vulnerable locations in various TBC systems where hastened failure is probable. If the vulnerable areas could be identified based on the cooling anatomy of TBC systems, remaining lifetime analysis should be emphasized at these locations and counter measures may be plausible for strengthening the local thermal resistance of these regions for prolonged coating lifetime.

Due to the large interrogation spot size diameter of 2 mm as opposed to a few hundred microns from Hawron's (2014) standard PLPS study, mild broadening of the R1 and R2 peaks can be observed in Fig. 49 which may also attribute to lower merit values. The broadened R1-R2 doublets indicate the possibility of multiple stress information contained within the collected fluorescence, and thus, further improvements are preferred prior to industrial practice of the time gated PLPS on irregular dopant TBC systems similar to the vane investigated in this chapter.

## 5.5 Possible Improvements for Enhanced Signal Quality in Time Gated PLPS

The elevated noise levels presented in the results can be attributed to the fundamental differences between the pulsed and continuous laser. The PLPS signal quality, in a sense, is volumetric and can be interpreted as a function of interrogation spot size and fluorescence intensity.

In previous applications where a continuous laser was employed, a substantially higher average laser power allowed larger fluorescence volumes to be collected. In the time gated PLPS setup, the Lotis Tii pulsed laser equipped with a 14 ns pulse duration and a repetition rate of 10 Hz introduced additional constraints on laser specifications. For every recurring pulse (10 pulses per second) the induced fluorescence during lasing (14 ns) comprises a miniscule portion of the total integration time (results from the PMT experiment showed that chromium fluorescence persisted for only a few microseconds). Furthermore, only a fraction of this portion is collected within the time dependent measurements. For this reason, the signal-to-noise ratios seen in Fig. 48 and Fig. 51 are substantially lower than measurements

taken on the continuous laser shown in Fig. 37. The elevated noise levels are reflected in the decreased merit values for the time gated PLPS measurements. Therefore, acceptable merit values for the time gated measurements were set at 0.8 (as opposed to the previously standard 0.975).

To achieve a favorable signal-to-noise ratio by upturning the energy per pulse of the laser is not without detrimental effects; for a given material, there is a peak power threshold which, if exceeded, ablation may occur. Such was the case for the investigated vane sample in this chapter; pulse energies exceeding the specified 70 mJ/pulse showed signs of ablation (section 3.3). Although the corresponding average power of this pulse energy was calculated to be 70 mW (compared to 500 mW from the previously employed Laserglow continuous diode), the peak power based on the laser pulse duration was calculated to be over a million-fold at 3.6 MW. Therefore, the workable pulse energies are bounded by the peak power as opposed to the average power. To improve signal quality, the average laser power should be maximized while maintaining peak laser power within the acceptable bounds; this is achievable by increasing the pulse repetition rate (Fig. 52).

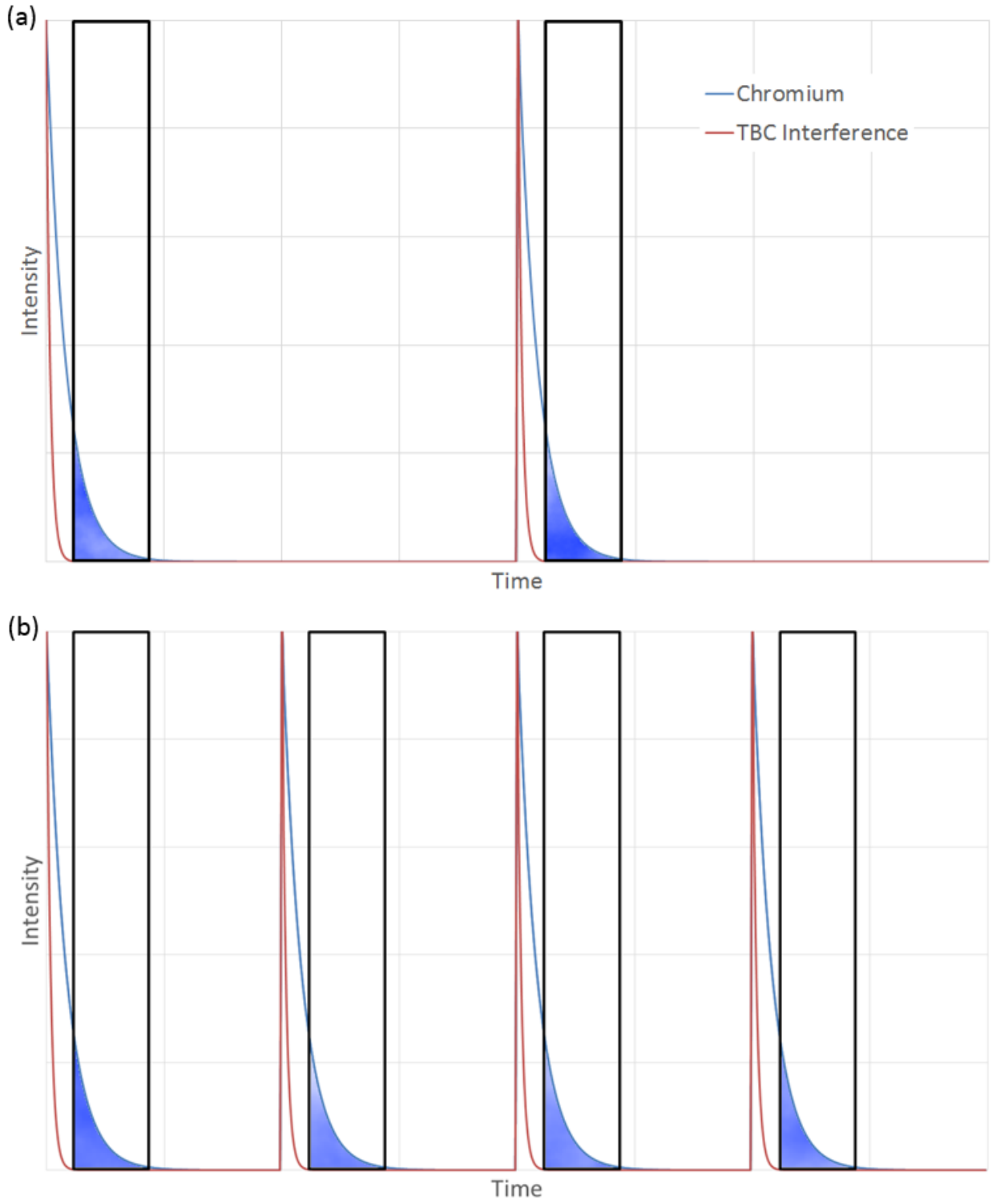


Figure 52: Simple schematic for improving PLPS signal quality over a given integration time. The blue-filled area indicates the measurements taken with a laser equipped with (a) low pulse repetition rate, and (b) high pulse repetition rate. In this illustration, the average power and the signal intensity is doubled meanwhile peak power remains constant. Axes are not to scale.

With substantial upgrades to the laser specifications discussed in this section, signal-to-noise ratios could be improved; not only would this increase merit values for stress measurements but also allow sufficient fluorescence signal for smaller interrogation spot diameters to account for possible variances in TGO stress.

## 5.6 Summary

Time gated PLPS was performed on a sample vane with coating impurity that exhibited unforgiving fluorescence interference near chromium at 694 nm. The overwhelming magnitude of the interference necessitated temporal filtering prior to spectral resolution. A test was performed to confirm the conditions necessary for a temporal resolution to be applicable; in this confirmation test, a photomultiplier tube was installed to observe the decay behaviors of each fluorescence per laser pulse. In the final setup, another vacuum phototube image intensifier could be installed to temporally resolve the mixed fluorescence using appropriate time parameters. Using a bandpass filter, the fluorescence interference was suppressed significantly which allowed stress measurements to be taken on the sample. Although the interference was no longer an issue after temporal resolution, measurement noises still persisted due to very weak chromium fluorescence intensities using the pulsed laser with inefficient average power output. To improve the time resolved fluorescence collection in this application, a pulsed laser with a higher pulse repetition rate with similar pulse energies is recommended. Once the laser equipment is adequately optimized to obtain merit values closer to 1, similar samples could be thermally cycled with weaved PLPS measurements to investigate notable differences in terms of coating lifetime.

Preliminary results showed significantly lower stress values near the tail end of the vane during PLPS diagnosis. Although the merit values were lower than in previous work, the consistency of the stress measurements of approximately 2.5 GPa within this neighborhood of interrogation are considered credible. These results indicate that thermal fatigue is accelerated at this region and it is likely for failure to occur within this proximity before the head of the blade. However, further investigation is required with a larger sample size of data to convincingly characterize this trend.

## Conclusion

Proper Orthogonal Decomposition (POD) was performed on CMAS spectra using forced modes obtained through relevant constituent references. CMAS speciation, previously performed by Lake (2012) using the Least Squares Fit (LSF) method showed comparable results but the computational cost limited its practical use during Laser-induced Breakdown Spectroscopy (LIBS) cleaning of contaminants on engine-run blades (Majewski, 2011). A different approach was taken using POD; the orthogonal properties of the modes enabled renormalization where these modes could be reshaped to minimize cross-talk between reference constituents while remaining orthogonal. Using cross-correlation values as a measure of cross-talk, the set of raw POD modes were renormalized two modes at a time subsequently. At the conclusion of this operation, a set of new modes were obtained that exhibited a maximum of 5.6% cross-correlation to any given reference spectra. These modes were calibrated to various mixtures of 99.99% pure pressed powdered samples of corresponding CMAS constituents prior to CMAS evaluation on engine-run coatings. The finalized modes, with appropriate calibrations, were used to decompose the CMAS constituent compositions based on spectral information during CMAS cleaning of the coating surface as a continuation of Majewski's (2011) previous work. However, a couple limitations to POD were discovered in this process; $Al_2O_3$ could not be calibrated within reasonable accuracy due to a lack of well-defined peaks that are unique from other CMAS constituents and due to the much lower signal intensities. For the same reason, $SiO_2$ was omitted from this analysis. The effectiveness of using POD scales with the amount of information involved in the construction of modes of interest; a complete library of CMAS constituent LIBS spectra on a broader range of investigated wavelengths may demonstrate significant potential in CMAS speciation via POD. As a hypothetical example, although the LIBS wavelengths investigated in this thesis (400-600 nm) showed success exclusively in CaO and MgO calibration, another set of wavelength ranges may be optimal for detection of the remaining constituents ($SiO_2$, $Al_2O_3$, and other missing oxides). Nevertheless, the orthonormal properties of the three identified constituent modes allowed a calculation of spectrally unaccounted species in a residual analysis. Due to orthogonality of the modes, the respectively computed contributions from the already identified

constituents could be subtracted from a CMAS spectrum without the side-effects of overestimations and underestimations as is the case for LSF. However, the validity of using pressed powdered samples for calibration has yet to be thoroughly investigated.

In addition to CMAS-based obstruction in PLPS measurements, chromium fluorescence interference may occur within the coating. With continual experimentation and implementation of modified YSZ coatings through addition of irregular dopants, coating-based fluorescence interference are a possibility. However, the source of interference within the coating is not exclusive to alumina; any dopant that coincides with the chromium fluorescence at 694 nm has a potential to invalidate stress measurements. A possible solution was proposed and demonstrated by introducing time as a variable in the measurement technique. The temporal resolution of PLPS measurements was viable under the condition that the mixed signals decay at sufficiently different rates. A photomultiplier tube was first used to observe the fluorescence decay as a function of time. After confirmation of workable time gating parameters, an image intensifier was used to collect time resolved measurements. Results showed that although the fluorescence interference was significantly resolved, the pulse repetition rate of the employed laser was suboptimal for achieving desirable signal-to-noise ratios. Regardless, the deconvolution of the R1-R2 doublets of the time resolved spectrum was satisfactory—a significant improvement to the results without time gating. Moderately lowering the acceptable merit values for the fit, results on the sampled vane showed variances in stress across opposite locations of the blade at the head and tail end, although measurements were locally consistent. Stress measurements yielded average values of 3.04 GPa near the head side, and 2.48 GPa near the tail end. These results indicate that this particular vane experienced accelerated thermal fatigue during service near the tail end. However, a larger sample size of data on similar blades should be performed with upgrades to the experimental setup for improved merit values.

**References**


Berkooz, G., Holmes, P., & Lumley, J. L. (1993). The proper orthogonal decomposition in the analysis of turbulent flows. *Annual review of fluid mechanics*, *25*(1), 539-575.

Braue, W. (2009). Environmental stability of the YSZ layer and the YSZ/TGO interface of an in-service EB-PVD coated high-pressure turbine blade. *Journal of materials science*, *44*(7), 1664-1675.

Cernuschi, F., Lorenzoni, L., Ahmaniemi, S., Vuoristo, P., & Mäntylä, T. (2005). Studies of the sintering kinetics of thick thermal barrier coatings by thermal diffusivity measurements. *Journal of the European Ceramic Society*, *25*(4), 393-400.

Chatterjee, A. (2000). An introduction to the proper orthogonal decomposition. *Current Science*, *78*(7), 808-817.

Chen, X. (2006). Calcium–magnesium–alumina–silicate (CMAS) delamination mechanisms in EB-PVD thermal barrier coatings. *Surface and Coatings Technology*, *200*(11), 3418-3427.

Christensen, R. J., Lipkin, D. M., Clarke, D. R., & Murphy, K. (1996). Nondestructive evaluation of the oxidation stresses through thermal barrier coatings using Cr3+ piezospectroscopy. *Applied Physics Letters*, *69*(24), 3754-3756.

Clegg, S. M., Sklute, E., Dyar, M. D., Barefield, J. E., & Wiens, R. C. (2009). Multivariate analysis of remote laser-induced breakdown spectroscopy spectra using partial least squares, principal component analysis, and related techniques. *Spectrochimica Acta Part B: Atomic Spectroscopy*, *64*(1), 79-88.

De Grauw, C. J., & Gerritsen, H. C. (2001). Multiple time-gate module for fluorescence lifetime imaging. *Applied Spectroscopy*, *55*(6), 670-678.

Feuerstein, A., Knapp, J., Taylor, T., Ashary, A., Bolcavage, A., & Hitchman, N. (2008). Technical and economical aspects of current thermal barrier coating systems for gas turbine engines by thermal spray and EBPVD: a review. *Journal of Thermal Spray Technology*, *17*(2), 199-213.

Grabner, L. (1978). Spectroscopic technique for the measurement of residual stress in sintered Al2O3. *Journal of Applied Physics*, *49*(2), 580-583.

Gell, M., Sridharan, S., Wen, M., & Jordan, E. H. (2004). Photoluminescence Piezospectroscopy: A Multi-Purpose Quality Control and NDI Technique for Thermal Barrier Coatings. *International Journal of Applied Ceramic Technology*, *1*(4), 316-329.

Han, J. C. (2004). Recent studies in turbine blade cooling. *International Journal of Rotating Machinery*, *10*(6), 443-457.

Hansen, G. E. (2007). Piezo Luminescence Photo Spectroscopy of Engine Run Turbine Blades (Ph.D. Thesis). University of Connecticut.

Hawron, M. P. (2014). Non-Destructive Evaluation and Maintenance of Thermal Barrier Coatings (M.S. Thesis). University of Connecticut.

Kim, H. N., Hawron, M. P., Hassan, W., Jordan, E. H., & Renfro, M. W. (2015). Contaminant identification during laser cleaning of thermal barrier coatings. *Surface and Coatings Technology*, *270*, 86-94.

Kim, T., Lin, C.-T. (2012). Laser-induced breakdown spectroscopy, in: M.A. Farrukh (Ed.), Advanced Aspects of Spectroscopy. *InTech*, 131-164.

Krämer, S., Yang, J., Levi, C. G., & Johnson, C. A. (2006). Thermochemical interaction of thermal barrier coatings with molten CaO–MgO–Al2O3–SiO2 (CMAS) deposits. *Journal of the American Ceramic Society*, *89*(10), 3167-3175.

Lake, J. L. (2012). Thermal Barrier Coating Analysis of Remaining Life and Contaminant Composition (M.S. Thesis). University of Connecticut.

Li, L., Hitchman, N., & Knapp, J. (2010). Failure of thermal barrier coatings subjected to CMAS attack. *Journal of thermal spray technology*, *19*(1-2), 148-155.

Liang, Y. C., Lee, H. P., Lim, S. P., Lin, W. Z., Lee, K. H., & Wu, C. G. (2002). Proper orthogonal decomposition and its applications—Part I: Theory. *Journal of Sound and vibration*, *252*(3), 527-544.

Loganathan, A., & Gandhi, A. S. (2012). Effect of phase transformations on the fracture toughness of t′ yttria stabilized zirconia. *Materials Science and Engineering: A*, *556*, 927-935.

Majewski, M. S., Kelley, C., Hassan, W., Brindley, W., Jordan, E. H., & Renfro, M. W. (2011). Laser induced breakdown spectroscopy for contamination removal on engine-run thermal barrier coatings. *Surface and Coatings Technology*, *205*(19), 4614-4619.

Majewski, M. S., Kelley, C., Lake, J., Renfro, M. W., Hassan, W., Brindley, W., & Jordan, E. H. (2012). Stress measurements via photoluminescence piezospectroscopy on engine run thermal barrier coatings. *Surface and Coatings Technology*, *206*(11), 2751-2758.

Mercer, C., Faulhaber, S., Evans, A. G., & Darolia, R. (2005). A delamination mechanism for thermal barrier coatings subject to calcium–magnesium–alumino-silicate (CMAS) infiltration. *Acta materialia*, *53*(4), 1029-1039.

Michel, A. P. (2010). Review: Applications of single-shot laser-induced breakdown spectroscopy. *Spectrochimica Acta Part B: Atomic Spectroscopy*,*65*(3), 185-191.

Multari, R. A., Cremers, D. A., Dupre, J. M., & Gustafson, J. E. (2010). The use of laser-induced breakdown spectroscopy for distinguishing between bacterial pathogen species and strains. *Applied spectroscopy*, *64*(7), 750-759.

Moran, M. J., Shapiro, H. N., Boettner, D. D., & Bailey, M. B. (2010). *Fundamentals of engineering thermodynamics*. John Wiley & Sons.

Padture, N. P., Gell, M., & Jordan, E. H. (2002). Thermal barrier coatings for gas-turbine engine applications. *Science*, *296*(5566), 280-284.

Rai, A. K., Bhattacharya, R. S., Wolfe, D. E., & Eden, T. J. (2010). CMAS-Resistant Thermal Barrier Coatings (TBC). *International Journal of Applied Ceramic Technology*, *7*(5), 662-674.

Rathinam, M., & Petzold, L. R. (2003). A new look at proper orthogonal decomposition. *SIAM Journal on Numerical Analysis*, *41*(5), 1893-1925.

Schlichting, K. W., Padture, N. P., Jordan, E. H., & Gell, M. (2003). Failure modes in plasma-sprayed thermal barrier coatings. *Materials Science and Engineering: A*, *342*(1), 120-130.

Selcuk, A., & Atkinson, A. (2002). Analysis of the Cr 3+ luminescence spectra from thermally grown oxide in thermal barrier coatings. *Materials Science and Engineering: A*, *335*(1), 147-156.

Sharp, G. C., Jiang, S. B., Shimizu, S., & Shirato, H. (2004). Prediction of respiratory tumour motion for real-time image-guided radiotherapy. *Physics in Medicine and Biology*, *49*(3), 425.

Spiglanin, T. A., McIlroy, A., Fournier, E. W., Cohen, R. B., & Syage, J. A. (1995). Time-resolved imaging of flame kernels: laser spark ignition of H 2/O 2/Ar mixtures. *Combustion and Flame*, *102*(3), 310-328.

Sridharan, S., Xie, L., Jordan, E. H., & Gell, M. (2004). Stress variation with thermal cycling in the thermally grown oxide of an EB-PVD thermal barrier coating. *Surface and Coatings Technology*, *179*(2), 286-296.

Tolpygo, V. K., Clarke, D. R., & Murphy, K. S. (2001). Oxidation-induced failure of EB-PVD thermal barrier coatings. *Surface and Coatings Technology*, *146*, 124-131.

Vaidyanathan, K. (2001). Failure Mechanisms of Platinum Aluminide Bond Coat/Electron Beam-Physical Vapor Deposited Thermal Barrier Coatings (Ph.D Thesis). University of Connecticut.

Wang, X., & Atkinson, A. (2007). Piezo-spectroscopic mapping of the thermally grown oxide in thermal barrier coatings. *Materials Science and Engineering: A*,*465*(1), 49-58.

Wellman, R. G., & Nicholls, J. R. (2007). A review of the erosion of thermal barrier coatings. *Journal of Physics D: Applied Physics*, *40*(16), R293.

Wen, M. (2005). Failure Mechanism and Mechanism-Base Life Prediction for Electron Beam Physical Vapor Deposition Thermal Barrier Coatings (Ph.D Thesis). University of Connecticut.

Wen, M., Jordan, E. H., & Gell, M. (2006). Analysis of localized damage in EB-PVD/(Ni, Pt) Al thermal barrier coatings. *Surface and Coatings Technology*, *200*(18), 5193-5202.

Wen, M., Jordan, E. H., & Gell, M. (2006). Effect of temperature on rumpling and thermally grown oxide stress in an EB-PVD thermal barrier coating. *Surface and Coatings Technology*, *201*(6), 3289-3298.

Zhu, D., Nesbitt, J. A., Barrett, C. A., McCue, T. R., & Miller, R. A. (2004). Furnace cyclic oxidation behavior of multicomponent low conductivity thermal barrier coatings. *Journal of Thermal Spray Technology*, *13*(1), 84-92.

**Appendix**

The two-mode renormalization described in Chapter 4 can be extended to a three-mode renormalization.

$$M_a = A_1 M_1 + A_2 M_2 + A_3 M_3$$

$$M_b = B_1 M_1 + B_2 M_2 + B_3 M_3$$

$$M_c = C_1 M_1 + C_2 M_2 + C_3 M_3$$

where, by the same orthonormal constraints held by the POMs, $M_1$, $M_2$, and $M_3$,

$$A_1^2 + A_2^2 + A_3^2 = 1$$

$$B_1^2 + B_2^2 + B_3^2 = 1$$

$$C_1^2 + C_2^2 + C_3^2 = 1$$

$$A_1 B_1 + A_2 B_2 + A_3 B_3 = 0$$

$$B_1 C_1 + B_2 C_2 + B_3 C_3 = 0$$

$$A_1 C_1 + A_2 C_2 + A_3 C_3 = 0$$

In three-mode renormalization, there are a total of 9 unknowns to be parameterized, $A_i$, $B_i$, and $C_i$, with 6 equations. Thus, 6 of the parameters are constrained by orthogonality, and the remaining 3 parameters can be freely chosen. Three-mode renormalization can be difficult to solve analytically, and often requires a numerical solution (often high computational cost). Furthermore, a three-mode renormalization does not necessary yield better results; similar results can be achieved using consecutive two-mode renormalization as demonstrated in this Thesis.

By the same token, larger numbers of modes (four-mode, five-mode, etc.) can be simultaneously renormalized.